INVERSE POLARITY PROMINENCE EQUILIBRIA

Apollonia Maria Oktavia Schönfelder

A Thesis Submitted for the Degree of PhD
at the
University of St Andrews

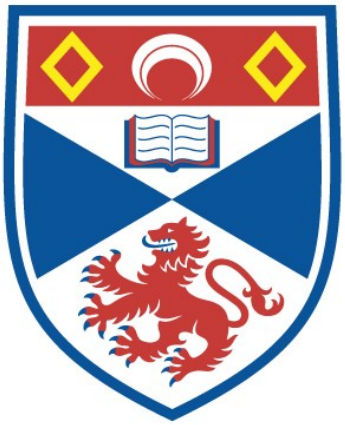

1995

Full metadata for this item is available in
St Andrews Research Repository
at:
http://research-repository.st-andrews.ac.uk/

Please use this identifier to cite or link to this item:
http://hdl.handle.net/10023/14243

This item is protected by original copyright

Inverse Polarity Prominence Equilibria

Apollonia Maria Oktavia Schönfelder

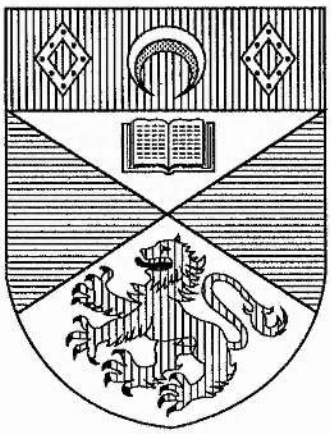

Thesis submitted for the degree of Doctor of Philosophy
of the University of St. Andrews.

ProQuest Number: 10167101

All rights reserved

INFORMATION TO ALL USERS
The quality of this reproduction is dependent upon the quality of the copy submitted.

In the unlikely event that the author did not send a complete manuscript
and there are missing pages, these will be noted. Also, if material had to be removed,
a note will indicate the deletion.

ProQuest 10167101

Published by ProQuest LLC (2017). Copyright of the Dissertation is held by the Author.

All rights reserved.
This work is protected against unauthorized copying under Title 17, United States Code
Microform Edition © ProQuest LLC.

ProQuest LLC.
789 East Eisenhower Parkway
P.O. Box 1346
Ann Arbor, MI 48106 – 1346

TL
B802

Declaration

1. I, Apollonia Maria Oktavia Schönfelder, hereby certify that this thesis has been composed by myself, that it is a record of my own work, and that it has not been accepted in partial or complete fulfilment of any other degree or professional qualification.

   Signed ....Date ..6. Je. June..1995

2. I was admitted to the Faculty of Science of the University of St. Andrews under Ordinance General No. 12 in October 1991 and as a candidate for the degree of Ph.D. in Octo[illegible] 1992

   Signed ....Date ..6. Je. June..1995

3. I hereby certify that the candidate has fulfilled the conditions of the Resolution and Regulations appropriate to the Degree of Ph.D.

   Signature of Supervisor ... .Date ..6. Je. June..1995

4. In submitting this thesis to the University of St. Andrews I understand that I am giving permission for it to be made available for use in accordance with the regulations of the University Library for the time being in force, subject to any copyright vested in the work not being affected thereby. I also understand that the title and abstract will be published, and that a copy of the work may be made and supplied to any bona fide library or research worker.

Acknowledgement

I am grateful to the Commission of European Communities, the ORS Award Sheme, the Austrian Federal Economic Chamber, the Department of Mathematics of St Andrews University, and the Dr. Maria Schaumayer Foundation in Austria for providing funding for this thesis.

I would like to thank my supervisor Dr. Alan W. Hood for his help and inspiration. I am also very grateful to my family and friends for their moral support.

For Craig

Contents

Chapter 1

Introduction

"Far have I fared, much afield have I been,
have often striven in strength with gods:
how soars the sun on the smooth heavens,
when snatched by Fenrir's fangs?"

"A daughter orb was to Alfrothul born,
ere that snatched her Fenrir's fangs;
on her mother's path will the maiden fare,
the time the fair gods fall."

(from *Vafthrudnismal, The Poetic Edda*)

The Sun, the central celestial body of our planetary system, has always been and is of vital importance to us. Without the Sun there would be no life on Earth. This crucial significance was recognised by all early civilisations and hence the Sun repeatedly appears in the myths of all people.

Modern scientists have stripped the Sun of his (or her) godly descent. He has become one of the objects that make up the physical world. As such, the Sun, and all his parts, are subject to the laws of physics.

As our nearest star, the Sun is the primary source of light, heat and energy for our planet. The Sun's gravity holds the Earth, the other planets, and innumerable smaller bodies in its grasp. Although the Sun may appear perfectly peaceful when watched for instance on a lazy afternoon, seen through a telescope his surface layers are constantly bubbling and seething.

The Sun is just one of approximately one billion stars in our galaxy. He is

an ordinary, middle-aged star of G2 spectral class. There is nothing that sets him apart from any of the other stars, except that the Sun is very much nearer; hence provides us with life, and also allows us to observe and investigate and study solar, i.e. stellar, features.

The solar phenomena are manifold; through the following chapters we will concern ourselves only with one of the many types, namely quiescent prominences.

It has been supposed since the middle of this century that it is the global magnetic field surrounding a quiescent prominence that provides the force to prevent its collapse due to the sun's gravitational field. Many theoretical models, assuming that the prominence plasma is supported in a dip in the magnetic field lines associated by the magnetic tension force, have since been put forward. The aim of this thesis is to propose further models of quiescent prominences to widen our understanding and knowledge of these remarkable features.

A short overview over the magnetohydrodynamic equations used to describe solar prominences, or most of the solar phenomena for that matter, are discussed in chapter 2, and a short summary of prominence observations and attempts to model them is given in chapter 3.

A brief description of the numerical code used in chapters 5 and 7 is given in chapter 4.

Observations of Kim (1990) and Leroy (1985) have found that most large quiescent prominences are of inverse polarity type for which the magnetic field passes through the prominence in the opposite direction to that expected from the photospheric magnetic field. Many theoretical models have been proposed, but failed. Hence, in chapter 5 we investigate first - without the inclusion of a prominence sheet - when an inverse polarity magnetic field structure can form due to imposed current distributions; since a pre-prominence magnetic field must have the correct topology for an inverse polarity configuration *before* the formation of the prominence itself.

Only very recently, the first basic successful model of an I-type polarity prominence was proposed by Low (1993). In chapter 6 we examine this model and investigate currents sheets more complicated and realistic than the one used by Low. These analytical models deal with the force-free solution, which is matched onto an

external, unsheared, potential coronal magnetic field. These solutions are mathematically interesting and allow an investigation of different profiles of the current intensity of the magnetic field vector and of the mass density in the sheet. The prominence properties predicted by these models have been examined and have been found to match the observational values. The mathematics of current sheets in general is also briefly discussed.

Chapter 7 deals with numerical solutions of inverse polarity prominences embedded in a force-free magnetic flux tube, matched onto an unsheared potential coronal field. Unfortunately the solutions gained are quite sensitive to the boundary conditions imposed on them through the numerical box, showing a loss of convergence and a tendency for the solution to blow up.

Finally, a short summary as well as possible future work is given in chapter 8.

Chapter 2

The Magnetohydrodynamic Equations

Magnetohydrodynamic (usually abbreviated as MHD) is the study of the interaction between a magnetic field and a plasma, treated as a continuous medium and a conducting gas. The length scales of all the physical processes with which we will be concerned are much larger than those on which individual particles interact, allowing us indeed to treat the plasma on the sun as a continuous fluid. Hence, the equations which govern these processes are the MHD-equations, outlined below. We start with Maxwell's equations of electrodynamics.

2.1 Maxwell's Equations

$$\nabla \cdot \mathbf{E} = \rho_c/\varepsilon, \tag{2.1}$$

$$\nabla \times \mathbf{B} = \mu \mathbf{j} + \frac{1}{c^2}\frac{\partial \mathbf{E}}{\partial t}, \tag{2.2}$$

$$\nabla \cdot \mathbf{B} = 0, \tag{2.3}$$

$$\nabla \times \mathbf{E} = -\frac{\partial \mathbf{B}}{\partial t}. \tag{2.4}$$

$\mathbf{B}$ is the magnetic induction (more usually referred to as the magnetic field), $\mathbf{E}$ the electric field, $\mathbf{j}$ the current density, and ρ_c the charge density. μ is the magnetic

permeability and ε the permittivity. They are usually approximated by μ_0 and ε_0, their values in the vacuum. The speed of light c can then be written as $c = (\mu_0 \varepsilon_0)^{-1/2}$.

Now we list assumptions used for the features we want to study. Consider the fact that most flows observed on the sun are non-relativistic; hence $v_0/c << 1$, where v_0 is a characteristic bulk flow speed. With this and the essentially neutrality of the plasma, $\rho_c << n\,e$ (n being the number density, e the electron charge), a comparison of the magnitudes of the terms in equation (2.2) shows that the displacement current $\partial \mathbf{E}/\partial t$ can be neglected. Equation (2.2) reduces to *Ampere's law*

$$\nabla \times \mathbf{B} = \mu \mathbf{j}. \tag{2.5}$$

A plasma, which is moving with a velocity $\mathbf{v}$ in a magnetic field, is subject to a total electric field of $(\mathbf{E} + \mathbf{v} \times \mathbf{B})$. The current density $\mathbf{j}$ is proportional to this electric field; so we can write *Ohm's law*, with σ being the electrical conductivity, as

$$\mathbf{j} = \sigma(\mathbf{E} + \mathbf{v} \times \mathbf{B}). \tag{2.6}$$

2.2 The Equations of Magnetohydrodynamics

induction equation

$$\frac{\partial \mathbf{B}}{\partial t} = \nabla \times (\mathbf{v} \times \mathbf{B}) - \nabla \times (\eta \nabla \times \mathbf{B}), \tag{2.7}$$

or if η is uniform throughout the plasma

$$\frac{\partial \mathbf{B}}{\partial t} = \nabla \times (\mathbf{v} \times \mathbf{B}) + \eta \nabla^2 \mathbf{B}. \tag{2.8}$$

continuity equation

$$\frac{\partial \rho}{\partial t} + \nabla \cdot (\rho \mathbf{v}) = 0, \qquad \text{or} \qquad \frac{D\rho}{Dt} + \rho\,(\nabla \cdot \mathbf{v}) = 0. \tag{2.9}$$

equation of motion

$$\rho \frac{D\mathbf{v}}{Dt} = -\nabla p + \mathbf{j} \times \mathbf{B} + \rho \mathbf{g} + \rho \nu \left(\nabla^2 \mathbf{v} + \frac{1}{3} \nabla (\nabla \cdot \mathbf{v}) \right), \tag{2.10}$$

perfect gas law

$$p = \frac{\rho \mathcal{R} T}{\mu_a}, \tag{2.11}$$

energy equation

$$\rho T \frac{Ds}{Dt} = -\mathcal{L}, \qquad \text{or} \qquad \frac{\rho^\gamma}{\gamma - 1} \frac{D}{Dt}\left(\frac{p}{\rho^\gamma}\right) = -\mathcal{L}. \tag{2.12}$$

solenoidal constraint from Maxwell's equations

$$\nabla \cdot \mathbf{B} = 0, \tag{2.13}$$

Ampere's law

$$\mathrm{j} = \frac{\nabla \times \mathbf{B}}{\mu}, \tag{2.14}$$

Ohm's law

$$\mathbf{E} = \frac{\mathrm{j}}{\sigma} - \mathbf{v} \times \mathbf{B}. \tag{2.15}$$

In equations (2.7) to (2.15) we have the following definitions:

$\mathbf{B}$	magnetic field
$\mathbf{v}$	plasma velocity
$\eta = 1/(\mu\sigma)$	magnetic diffusivity
μ	magnetic permeability
σ	electric conductivity
ρ	plasma density
$\frac{D}{Dt} = \frac{\partial}{\partial t} + \mathbf{v} \cdot \nabla$	convective time derivative
p	plasma gas pressure
j	current density
g	gravitational acceleration
ν	coefficient of kinematic viscosity, assumed to be uniform throughout the plasma
$\mathcal{R}$	gas constant
μ_a	mean atomic weight, 0.6 in the solar corona
T	temperature
s	entropy per unit mass of the plasma
$\mathcal{L}$	energy loss function due to all sources and sinks present
$\gamma = c_p/c_v$	ratio of specific heat of the gas at constant pressure to that at constant volume

The induction equation (2.7) determines **B** once **v** is known. It was obtained by using equations (2.3), (2.4), (2.5) and (2.6) and eliminating the electric field and the current density.

The ratio of the convective term and the diffusive term in the induction equation (2.7), written in terms of a typical plasma velocity v_0 and length scale l_0 is known as the *magnetic Reynolds number*

$$R_m = \frac{l_0 v_0}{\eta}. \tag{2.16}$$

For many solar applications R_m is very much bigger than unity, allowing us to neglect the diffusion term in equation (2.7). This limit of MHD is called *ideal MHD*. From the ideal approximation follows *Alfvén's frozen-flux theorem* which states that in a perfectly conducting plasma, magnetic field lines move with the plasma as if frozen to it.

The continuity equation (2.9) comes from the conservation of mass, whereas the equation of motion (2.10) from the conservation of momentum. The four terms on the right hand side of equation (2.10) describe the plasma pressure gradient force, the Lorentz force, and the effects of gravity and viscosity, respectively.

The Lorentz force can be decomposed into two parts, written as

$$\mathbf{j} \times \mathbf{B} = \frac{1}{\mu} (\mathbf{B} \cdot \nabla) \mathbf{B} - \nabla \left(\frac{B^2}{2\mu} \right). \tag{2.17}$$

The first part represents the effect of magnetic tension, of magnitude B^2/μ per unit area, resulting in a magnetic tension force if the field lines are curved, and the second part represents the effect of a magnetic pressure, $B^2/2\mu$, giving a resultant magnetic pressure force when B varies with position.

For simplicity the perfect gas law has been taken to determine the plasma pressure. A useful quantity is the *plasma beta*,

$$\beta = \frac{2\mu p}{B^2}, \tag{2.18}$$

which is the ratio of plasma pressure to magnetic pressure. If $\beta << 1$, the magnetic force dominates the gas pressure force and vice versa if $\beta >> 1$.

There are also velocities associated with the plasma, namely the sound speed

$$c_s = \sqrt{\frac{\gamma p}{\rho}} \tag{2.19}$$

and the Alfvén speed

$$v_A = \frac{B}{\sqrt{\mu\rho}} \tag{2.20}$$

which is the velocity at which transverse waves propagate along the magnetic field due to its magnetic tension.

2.3 The Equations of Magnetohydrostatics

magnetohydrostatic equilibrium

$$0 = -\nabla p + \mathbf{j} \times \mathbf{B} + \rho \mathbf{g}, \tag{2.21}$$

force-free fields

$$\mathbf{j} \times \mathbf{B} = 0. \tag{2.22}$$

The equation of magnetohydrostatic equilibrium (2.21) considers the special case of static equilibrium structures which do not evolve in time. Then time derivatives and velocities are set identically to zero and both the induction and the continuity equations become redundant, while equation of motion reduces to equation (2.21).

If gravity acts in the negative z-direction, then resolving the forces along a field line yields to

$$p = p_0 \, e^{-\int_0^z \frac{dz}{H(z)}}, \tag{2.23}$$

where p_0 is the pressure at $z = 0$ and $H(z)$ is the pressure scale height given by the perfect gas law as

$$H(z) = \frac{\mathcal{R} T(z)}{\mu_a \, g(z)}. \tag{2.24}$$

When the vertical extent of the structure under consideration is much less than the scale height H, gravitational forces are negligible compared to pressure

gradient forces. In addition, when the plasma beta (2.18) is very much less than unity, pressure forces are negligible compared with the Lorentz force. Thus, we end up with the concept of a plasma in a magnetic field called *force-free* (2.22), i.e. a field which does not require external forces. The magnetic forces dominate all others and hence $\mathbf{B} \times (\nabla \times \mathbf{B}) = 0$.

2.3.1 The Grad-Shafranov-Equation

The problem of the MHD equilibrium of the solar corona amounts to finding solutions to the MHS equilibrium equation (2.21) together with Ampere's law (2.14) and Maxwell's solenoidal constraint (2.13).

When gravity is neglected and all quantities are functions of a horizontal variable, y, and a vertical one, z, only, but independent of the second horizontal coordinate, x, we can introduce a flux function $A(y,z)$ and a third component $B_x(y,z)$ such that the magnetic field becomes

$$\mathbf{B} = \nabla \times \big(A(y,z)\,\hat{\mathbf{e}}_x\big) + B_x(y,z)\,\hat{\mathbf{e}}_x\,, \tag{2.25}$$

or written in component form

$$\mathbf{B} = \big[B_x(y,z),\, \partial_z A(y,z),\, -\partial_y A(y,z)\big]\,. \tag{2.26}$$

For simplicity we have used the notations

$$\partial_k = \frac{\partial}{\partial k} \qquad \text{and} \qquad \partial_k^2 = \frac{\partial^2}{\partial k^2}\,, \qquad k = x, y, z.$$

The electric current density $\mathbf{j}$ is then given by equation (2.14) and becomes

$$\mu\mathbf{j} = -(\partial_y^2 A + \partial_z^2 A)\,\hat{\mathbf{e}}_x + \partial_z B_x\,\hat{\mathbf{e}}_y - \partial_y B_x\,\hat{\mathbf{e}}_z. \tag{2.27}$$

The equilibrium equation (2.21) then separates into

$$0 = -\partial_z B_x \partial_y A + \partial_y B_x \partial_z A, \tag{2.28}$$

$$-\mu\,\partial_y p = \big(\partial_y^2 A + \partial_z^2 A\big)\,\partial_y A + B_x \partial_y B_x, \tag{2.29}$$

$$-\mu\,\partial_z p = \big(\partial_y^2 A + \partial_z^2 A\big)\,\partial_z A + B_x \partial_z B_x. \tag{2.30}$$

Equation (2.28) expresses that B_x is a function of A only,

$$B_x(y,z) = B_x\Big(A(y,z)\Big). \tag{2.31}$$

Multiplying equation (2.29) by $\partial_z A$ and (2.30) by $\partial_y A$ and subtracting them, taking (2.28) into account, we obtain similarly

$$\partial_y A\, \partial_z p = \partial_z A\, \partial_y p, \tag{2.32}$$

showing that p too is a function of the flux function only,

$$p(y,z) = p\Big(A(y,z)\Big). \tag{2.33}$$

Hence B_x and p are constant along the field lines.

A given equilibrium structure is characterised by the functions $B_x(A)$ and $p(A)$ and the calculation of the magnetic configuration boils down to solving equations (2.29) and (2.30), which, due to equations (2.31) and (2.33), collapse into the so-called *Grad-Shafranov equation* (originally derived independently by Lüst and Schlüter, 1957; Shafranov, 1958; Grad and Rubin, 1958)

$$\nabla^2 A + \frac{d}{dA}\left(\frac{1}{2}B_x^2(A) + \mu\, p\,(A)\right) = 0. \tag{2.34}$$

If the plasma beta is very much less than unity, as is the case in the solar corona, the plasma pressure gradient force is negligible when compared to the Lorentz force and the Grad-Shafranov equation takes the form

$$\nabla^2 A + \frac{1}{2}\,\frac{dB_x^2(A)}{dA} = 0 \tag{2.35}$$

In general, B_x(A) is a nonlinear function of A and the Grad-Shafranov equation becomes a non-linear, partial differential equation.

Many authors have looked for solutions to the Grad-Shafranov equation, once the form of $B_x(A)$ has been imposed.

- The simplest approach is setting $B_x(A) = \alpha$, ($\alpha \in \Re$). Then equation (2.35) reduces to Laplace's equation, corresponding to potential fields.

- Another possibility is setting $B_x(A) = \alpha A$ so that equation (2.35) reduces to the linear Helmholtz equation giving the so-called constant-α or linear force-free fields.

- For $B_x(A) = \alpha\sqrt{A}$ equation (2.35) becomes Poisson's equation, corresponding to constant-current force-free fields (j_x is a constant).

Although solar processes are dynamic on small length scales, many can be described by the magnetohydrostatic equation. The *Reynolds number* is the ratio of the inertial term to the viscous term in the equation of motion (2.10),

$$Re = \frac{l_0 v_0}{\nu}. \tag{2.36}$$

For many aspects of solar theory the Reynolds number is very much larger than unity, thus allowing viscous effects to be neglected. Furthermore, the inertial term itself may be neglected, if the plasma velocity is very much less than the sound speed (2.19), the Alfvén speed (2.20) and the gravitational free fall speed $\sqrt{gh}$. Such a system evolves slowly in time and is assumed to go through a series of essentially static equilibrium states. This can be approximated by the MHS equilibrium equation (2.21) and is known as a quasi-static evolution.

Chapter 3

Solar Prominences

3.1 Introduction

Solar prominences are huge structures of condensed gas located in the lower solar atmosphere. They can be divided into two principal categories, as either quiescent or active region prominences. Quiescent prominences are among the most stable and long-lived of solar phenomena. They are the subject of this thesis.

3.2 Observational Features of Quiescent Prominences

Observations of prominences reach back as far as the 13th century; but it was not until the middle of the last century that good photographic techniques provided observations for scientific studies of their properties.

In Hα photographs of the solar disc prominences appear as long, dark features due to their absorption of the underlying photospheric emissions. When observed at the limb in its own emission, they appear bright and show a variety of shapes, but are generally much more extended in height than in thickness. Observers refer to a prominence as a filament when seen as an absorption feature. (See Figure 3.2, or Figure 3.1 for an example.)

Prominences are huge, vertical sheets of cool, dense plasma embedded in the

hot corona, with a length ranging from 60 - 600 Mm (1 Mm = 10^6 m), a height from 10 - 100 Mm, and a width from 4 - 15 Mm. Average values for the length, height and width are 200 × 50 × 6 Mm (Priest, 1982). (Figure 3.1)

They form in the zone between two large-scale regions of opposite photospheric polarity (Martin, 1973) and may retain their overall shape and structure from a few months to as much as a year. During that time they gradually drift polewards, tilting continuously away from the north-south direction to almost east-west at high latitudes, forming a polar crown. Eventually they break up, either disappearing, or erupting into space and revealing, quite often, a twisted helical structure (Figures 3.3 and 3.4). Generally they reform in the same place.

Their density ($0.5-1.0\times10^{17}$ m^{-3}) is about 500 times more than the ambient coronal value and their temperature ($5-10\times10^3$ K) about 500 times less. They show much fine structure in form of vertical threads (Figure 3.5), typically 5 - 7 Mm long and 0.3 - 1 Mm wide, with a filling factor between 0.01 and 0.1. They reach down to the photosphere in a series of regularly spaced feet spaced about 30 Mm and located at supergranule boundaries. (Figure 3.6) Internal mass motions are observed within a prominence with downflows of 0.5 km/s when observed on the limb and upflows of 0.5 - 3 km/s when viewed on the disc. However, these observed flows in prominences are much smaller than the free-fall speed $\sqrt{gh}$ of about 100 km/s, and so the plasma is essentially in equilibrium with a rough balance between the magnetic, pressure and gravitational forces as it very slowly dribbles through the magnetic field. (Engvold, 1976; Mein, 1977; Martres et al., 1981)

Surrounding a prominence a region of reduced density can be seen, known as the coronal cavity. Above it an arcade of hot loops (typically 400 Mm in width) and a helmet streamer, stretching radially outwards, is frequently observed (Tandberg-Hanssen, 1974).

The magnetic field through prominences lies between 3 - 30 Gauss, and increases with height (Rust, 1967; Leroy, 1977). It is inclined approximately 3° to the horizontal (Athay, et al., 1983) and about 20° to the longitudinal prominence axis (Tandberg-Hanssen and Anzer, 1970; Leroy et al., 1983; Kim, 1990). The highly important observation of Babcock and Babcock (1955) was that prominences are

always found to lie above the magnetic polarity inversion line between two large-scale areas of opposing photospheric magnetic field polarities.

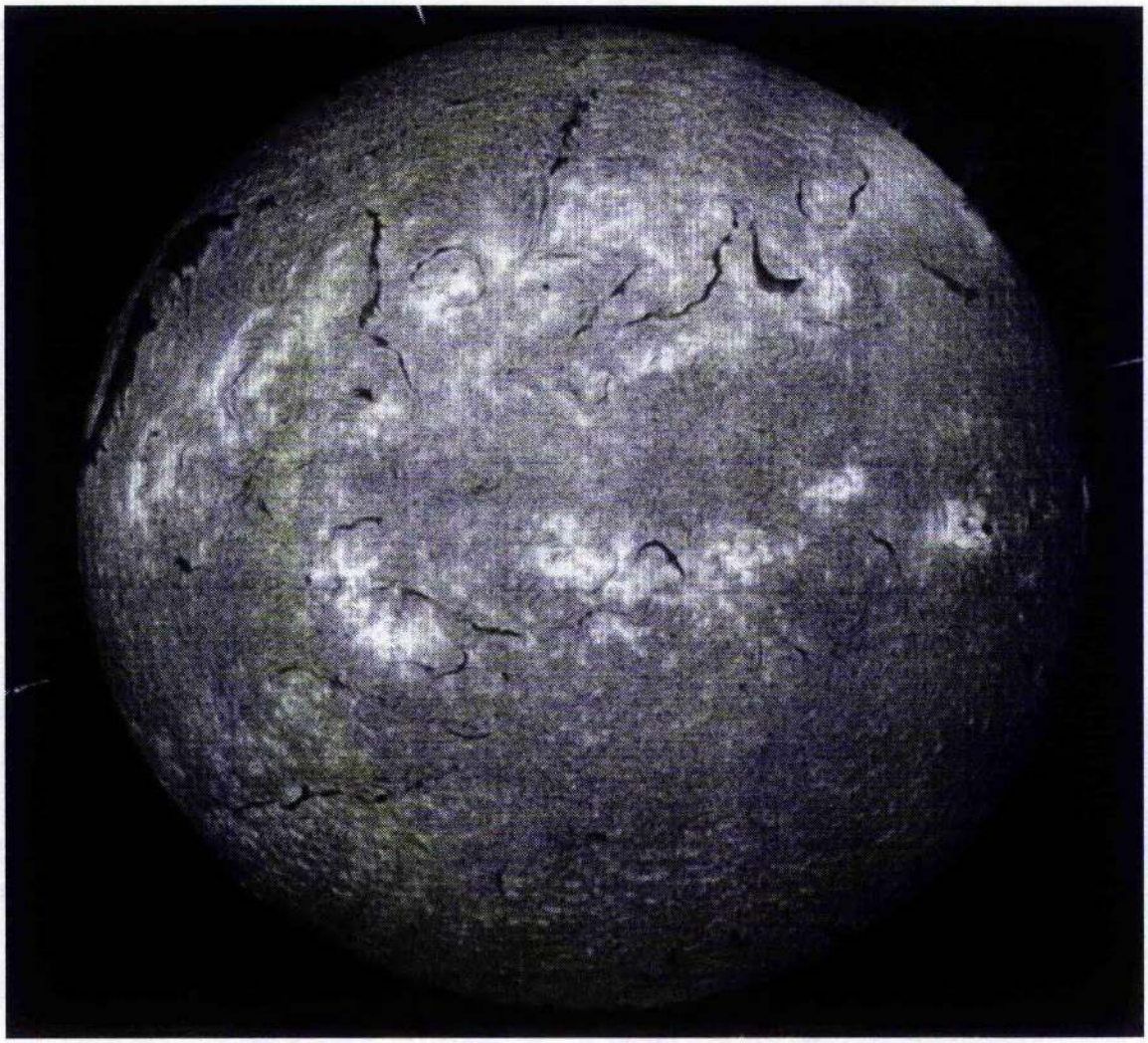

Figure 3.1: Full disc Hα observation of the sun. (Courtesy of Meudon Observatory)

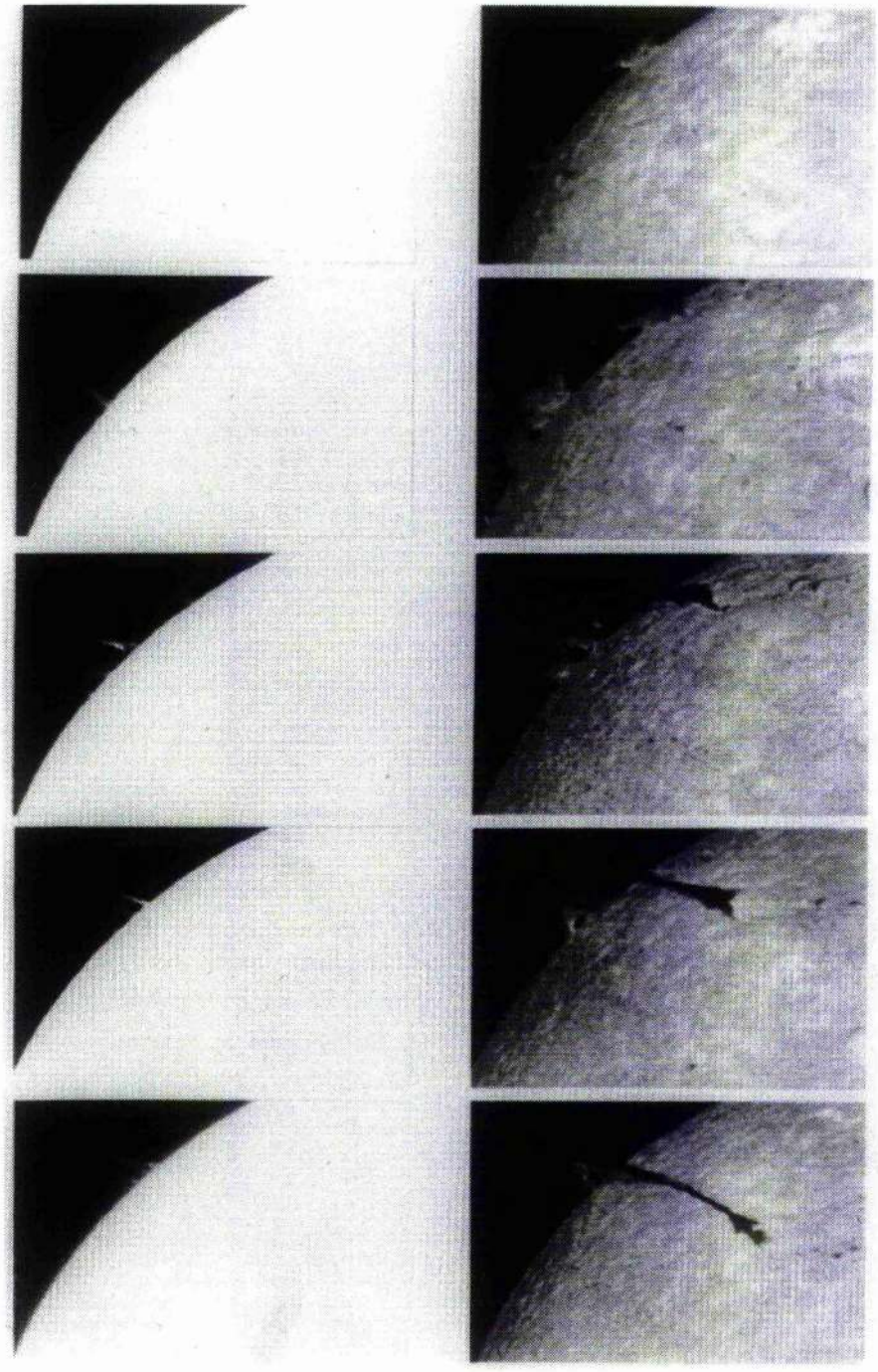

Figure 3.2: Disc observation of a filament. When reaching the limb due to the sun's rotation, the filament is seen bright as an emission feature, "becoming" a prominence. (Courtesy of Sacramento Peak Observatories)

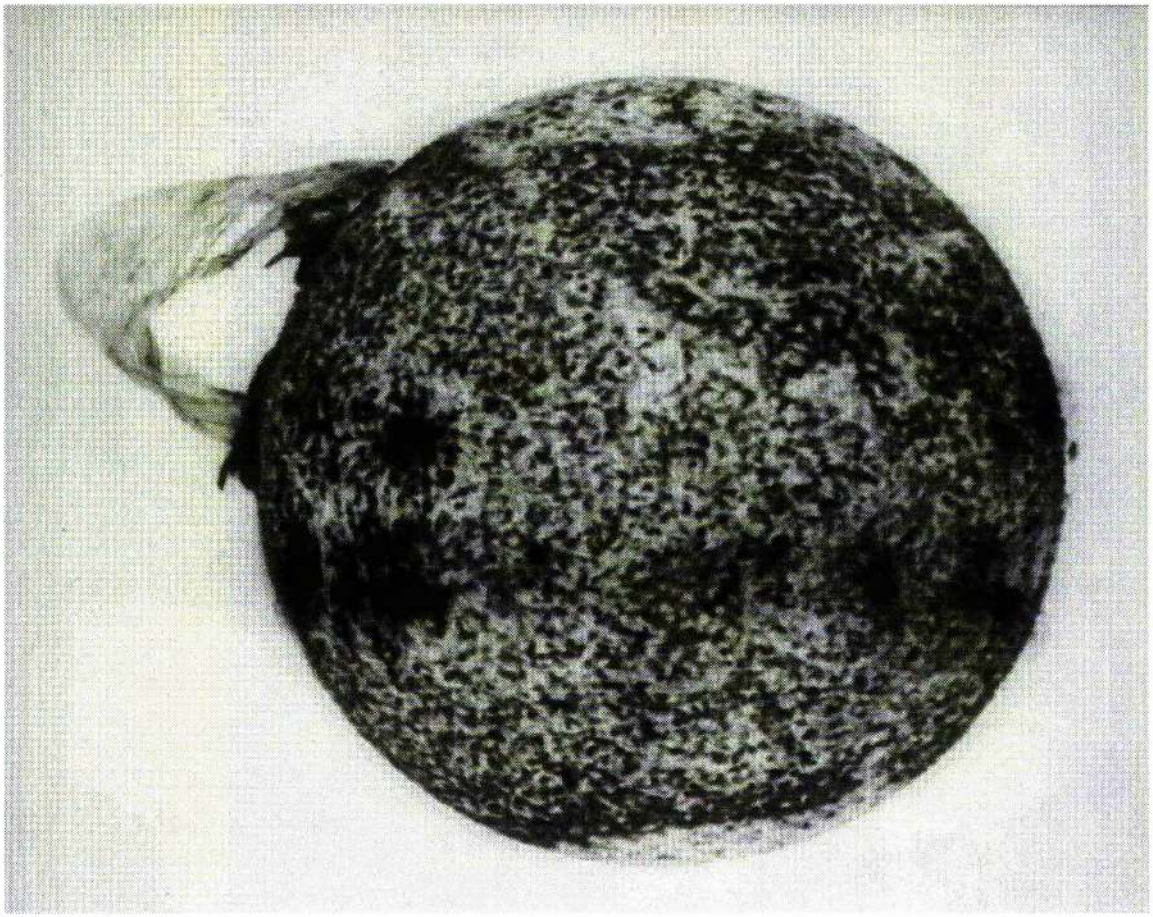

Figure 3.3: Erupting prominence, revealing its helical structure (inverted colour). (Courtesy of Naval Research Laboratories)

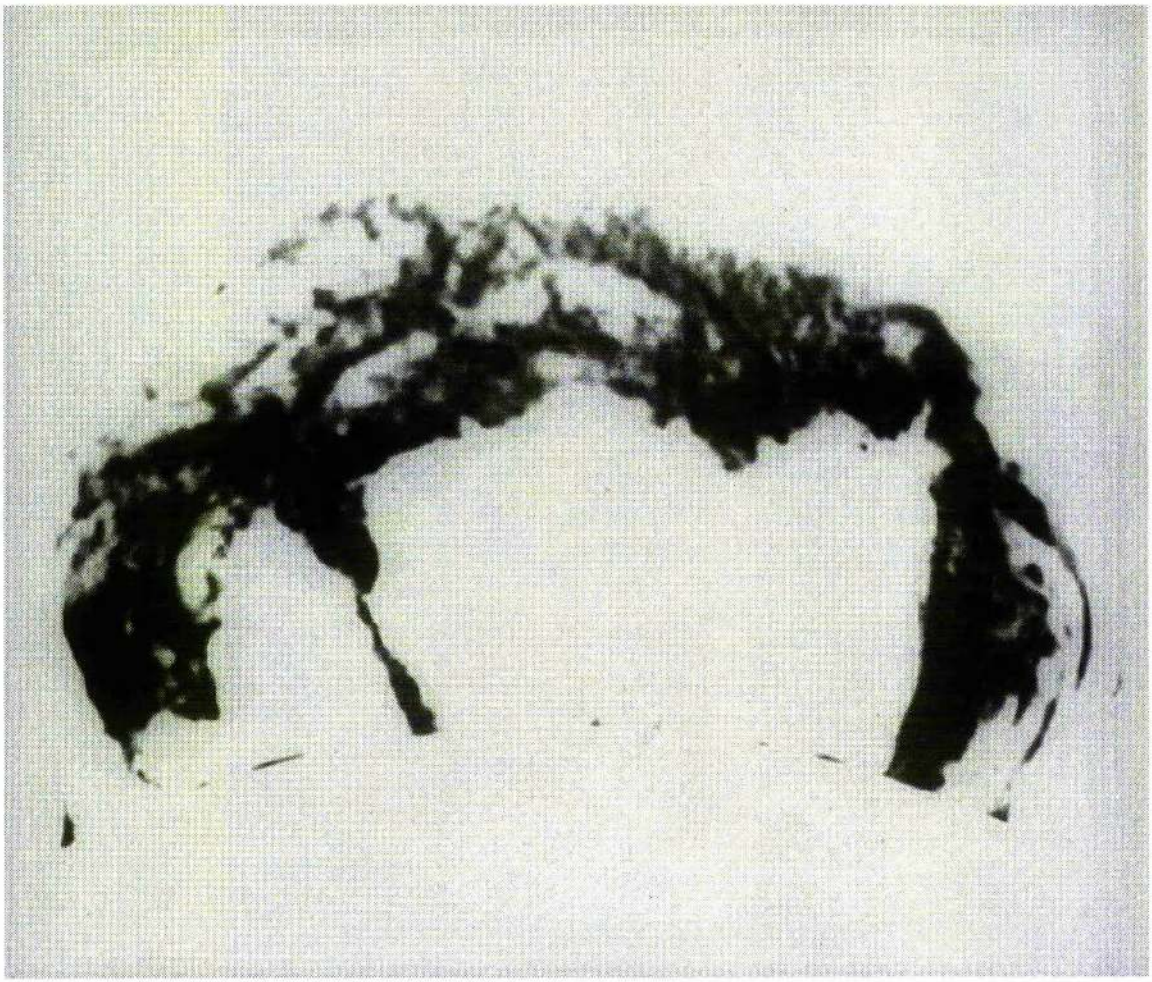

Figure 3.4: Erupting prominence (inverted colour). (Courtesy of Sacramento Peak Observatories)

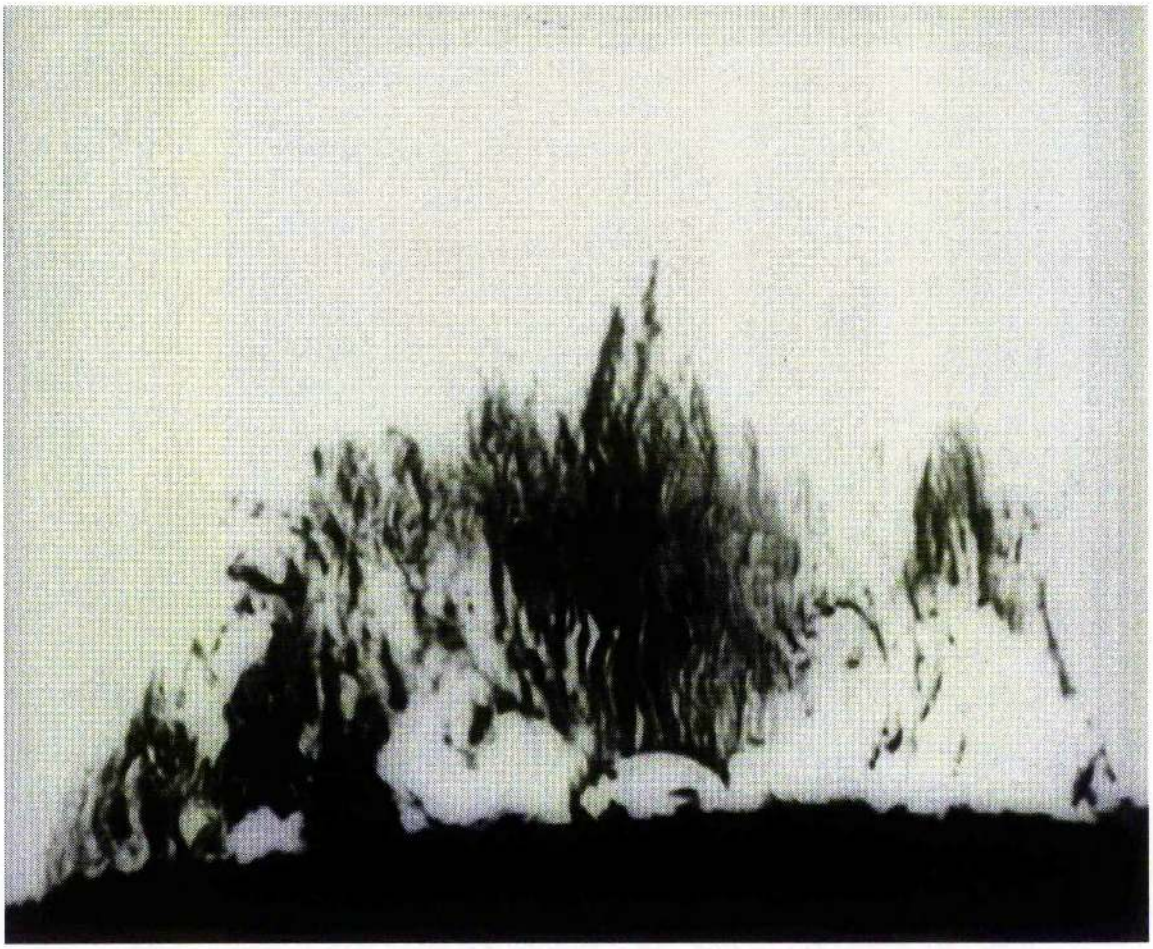

Figure 3.5: "Hedgerow" prominence, showing clearly a fine structure in form of vertical threads (inverted colour). (Courtesy of Sacramento Peak Observatories)

Figure 3.6: Prominences reach down towards the photosphere in a series of regularly spaced feet, resembling great tree trunks (inverted colour). (Courtesy of Meudon Observatory)

3.3 Models of Inverse Polarity Prominences

The magnetic field is a good candidate for the support of prominences, particularly because they always overlie a photospheric neutral line. Prominences fall into two categories depending on whether the magnetic field configuration is topologically similar to either the model described by Kippenhahn and Schlüter (1954) (Figure 3.7), in which the field passes through the prominence in the same direction as the underlying photospheric field (*normal* or *N-type polarity*), or that of Kuperus and Raadu (1974) (Figure 3.10), in which the field through the prominence is in the opposite (or inverse) direction to that of the underlying field (*inverse* or *I-type polarity*).

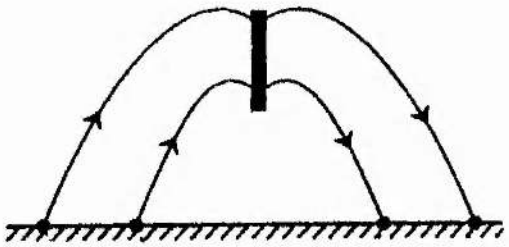

Figure 3.7: The magnetic field configuration for a Kippenhahn-Schlüter model.

Observations (Leroy, 1985, Kim, 1990) have shown that most large, high prominences are of the inverse polarity type.

The first model set forth to describe an I-type polarity magnetic structure (Kuperus and Raadu, 1974) represents the prominence by a current filament embedded in a purely vertical background field (Figure 3.8 a) which reverses its direction at one point ($x = 0$). No Lorentz force is provided by such a field. In order to find equilibrium Kuperus and Raadu postulated induced photospheric currents. These can be represented mathematically by image currents situated below the photosphere at equal depth, with equal strength but opposite direction to the original current (Figure 3.8 b). These two currents will repel each other and thus give rise to the

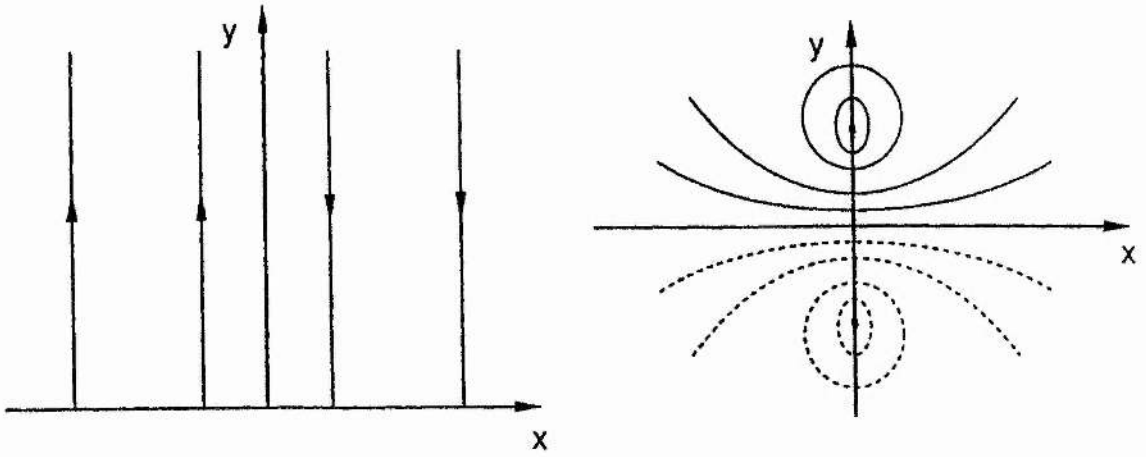

(a) (b)

Figure 3.8: The magnetic fields combined in the Kuperus-Raadu model. (a) The background vertical field. (b) The magnetic field due to a prominence filament located at (0,y) and its image filament located at (0,-y).

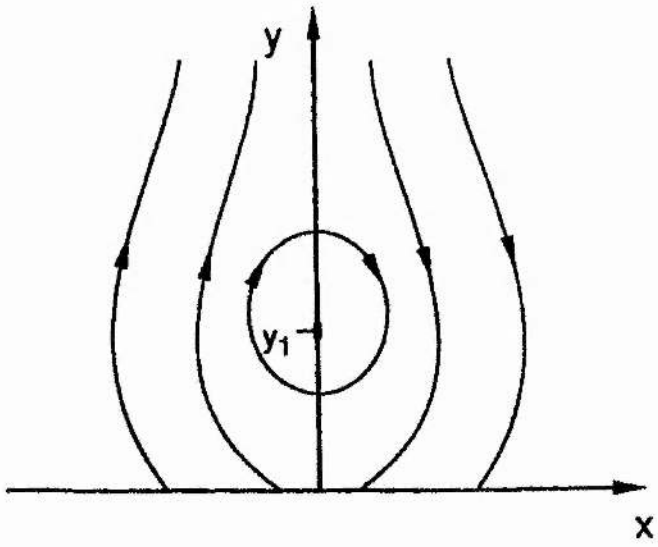

Figure 3.9: The resultant magnetic field of the Kuperus-Raadu model.

required Lorentz force. The resulting magnetic field configuration is shown in Figure 3.9. Van Tend and Kuperus (1978) and Kuperus and Van Tend (1981) extended the work of Kuperus and Raadu (1974) including the effect of an additional background magnetic field. By increasing the filament current intensity above a certain threshold value no neighbouring equilibrium could be found anymore, possibly leading to a dynamic evolution such as a prominence eruption.

However, prominences are not well represented by current filaments since their vertical extent is not negligible. Extending the prominence to a current sheet by keeping the above field topology yields to configurations shown in Figure 3.10. Sketch 3.10 a possesses an O-type neutral point only, whereas in 3.10 b an X-type neutral point is also present below the prominence current sheet but above the photosphere.

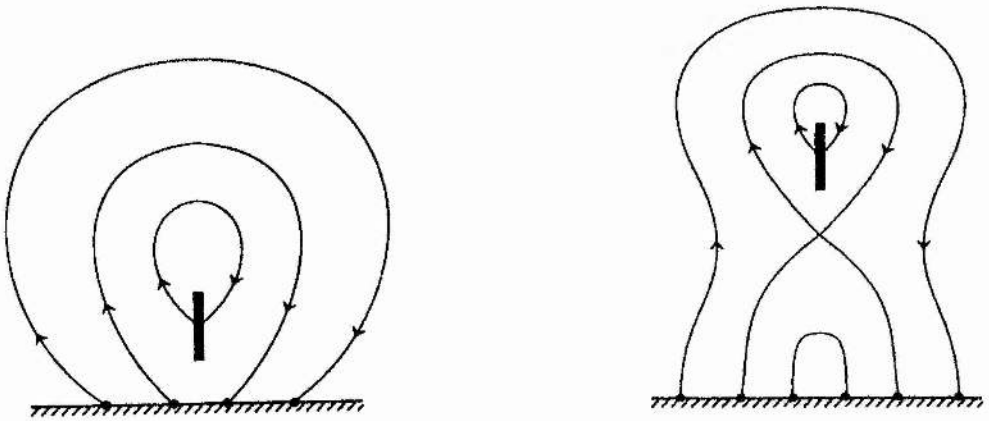

(a) (b)

Figure 3.10: Current sheet configurations of inverse polarity (a) with an O-type neutral point, (b) with an O-type and X-type neutral point.

Malherbe and Priest (1983) used complex variable theory ($\eta = x + iy$) to model prominences as a cut in the upper-half complex plane extending along the imaginary axis from $\eta = ip$ to $\eta = iq$. An analytic function η outside the cut can then describe a potential coronal field written in the form $B_y + iB_x$. Examples

of generated inverse polarity configurations are given in Figure 3.11. However, the helical structure shown in Figure 3.11 b is not in local equilibrium, the Lorentz force being downwards at the upper end of the current sheet. In addition, these fields are singular at the polarity inversion line.

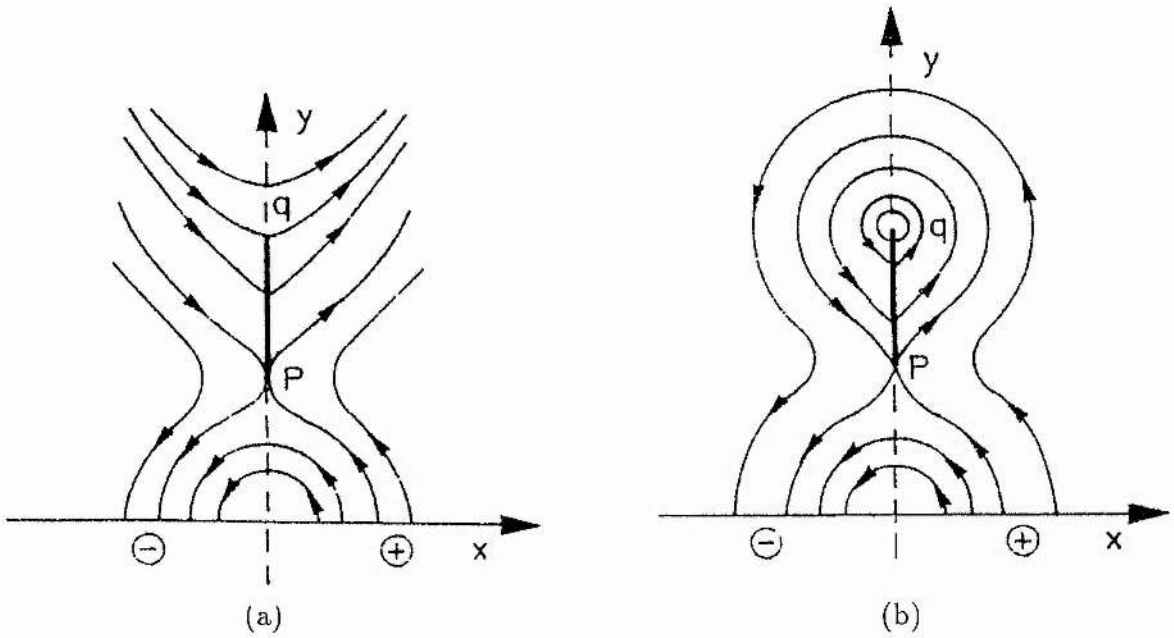

Figure 3.11: Malherbe-priest models of (a) inverse polarity, (b) inverse helical structure

The most realistic models recently presented describe the prominence as a sheet of mass and current (the vertical extent of a prominence is much greater than its width) located in a force-free coronal field, since vector magnetograms observations (Leroy et al., 1983) have shown that there exist (i) currents flowing in the corona and (ii) a strong field component along the prominence axis.

Démoulin et al. (1992), modelling linear force-free fields, found that inverse polarity configurations can be explained by assuming a quadrupolar flux distribution, an idea put forward earlier by Anzer in 1990. However, prominences belonging to the

polar crown class, and probably others too, are associated with bipolar photospheric flux distributions; hence the quadrupolar constant-α models of Démoulin et al. (1992) cannot be used as a general explanation for inverse polarity prominences.

Up to the time of the review of Anzer (1993) attempts at producing physical models for inverse polarity prominences have been unsuccessful. The reason for that is that when modelling a prominence by a current sheet rather than a line current, a problem is introduced by the self-attraction of the currents within the sheet. The current in the sheet is everywhere of the same sign, hence different current elements attract each other. On top of the sheet this attractive force exerted by these like-sign current elements is stronger than the repulsive force exerted by the images of the current elements, which are located further away. Hence, the net force on top of the current sheet is necessarily downwards, irrespective of the current distribution in the sheet. This domination of the self-pinching effect to collapse the sheet over the repulsion force due to the image currents, leading to the inevitability of a downwards Lorentz force on top of a current sheet, is a problem of internal structure. The prominence sheet as a spatially extended object suspended in a bipolar potential magnetic field cannot be threaded by magnetic field lines which are closed in the atmosphere (independently derived by Lepeltier and Aly (1995), and Low and Hundhausen (1995)).

The obvious conclusion, once the above fundamental reason for the general failure of modelling inverse polarity prominences is recognised, is that prominences of I-type polarity require the presence of volumetric currents in the surrounding corona to exert additional forces for the prominence support. The assumption that the magnetic field around a prominence is potential must be relaxed.

Nevertheless, the same problem even persisted in models with certain linear force-free fields (Amari and Aly, 1990). Extending their work Amari and Aly (1992) found that equilibrium for inverse polarity prominences can be obtained, though only for strongly restricted parameters. Hence some calculated prominence properties differ greatly from their observed values.

Ridgway, Amari and Priest(1991) examined a finite, vertical current sheet in a constant current force-free field and found it to be in static equilibrium for both

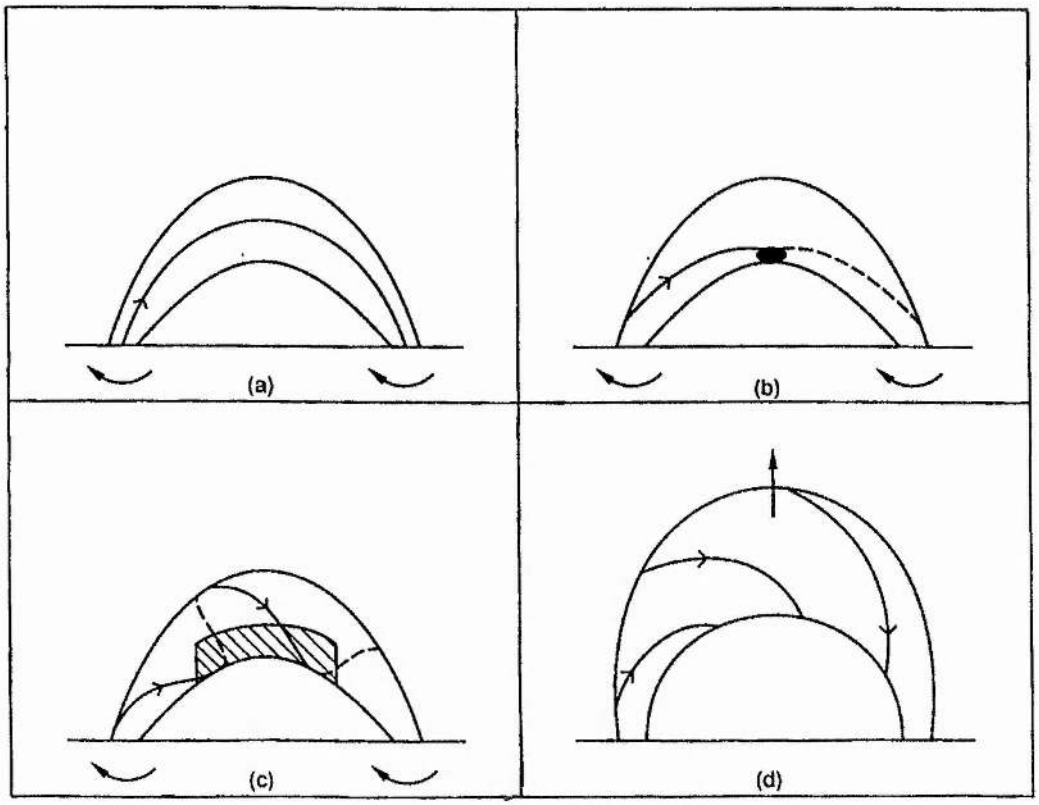

Figure 3.12: The evolution of a large twisted flux tube. (a) The initial arcade without twist. (b) The first field line attains a dip. (c) The prominence grows as more field lines acquire dips. (d) Such a large twist that the prominence erupts, revealing its helical structure. (From Priest, Hood and Anzer, 1989)

N-type and I-type polarity configurations. However, the magnetic fields obtained diverge at large distances. Therefore also these fields cannot be used for modelling inverse polarity prominences.

Démoulin and Forbes (1992) combined photospheric and prominence data to determine the coronal field around a prominence. To remove the problem of self-pinching and lack of support found by Anzer (1989), they added a massless current line in the corona. Then also inverse configurations are possible in a bipolar region as long as this line current, or equivalently, a twisted flux tube is present.

One major model proposed by Priest, Hood and Anzer (1989) is that of a large-scale, curved twisted flux tube (Figure 3.12). By inducing twisting motions at the end of the flux tube in the photosphere due to the Coriolis force they found it was possible to create dips in the field lines near the summit of the tube. For prominence formation the existence of such dips prior to the condensation of plasma is a necessary condition.

Ridgeway, Priest and Amari (1991) developed this theory into a force-free model of a flux tube supporting a current sheet (representing the prominence) at the low points of its windings.

Cartledge and Hood (1993) developed that work further and expanded the current sheet to a finite width, matching the internal prominence solution to the external force-free solution within the twisted flux tube. However, a detailed matching of the flux tube to the untwisted coronal field was not demonstrated in that paper.

Van Ballegooijen and Martens (1989) presented a model where reconnection and flux cancellation at the neutral line of a sheared arcade leads to the formation of helical field lines (Figure 3.13).

The solar corona is both tenuous and highly electrically conducting. It can sustain electric currents, but cannot support any significant Lorentz force needed to prevent the self-pinching of a current sheet. Therefore the presence of force-free magnetic fields around the prominence is a simple way of introducing currents into the corona to produce a significant Lorentz force on the prominence without exerting a comparable force on the corona. This was the basic feature of the first successful prominence model for a prominence of I-type polarity, proposed by Low (1993). In

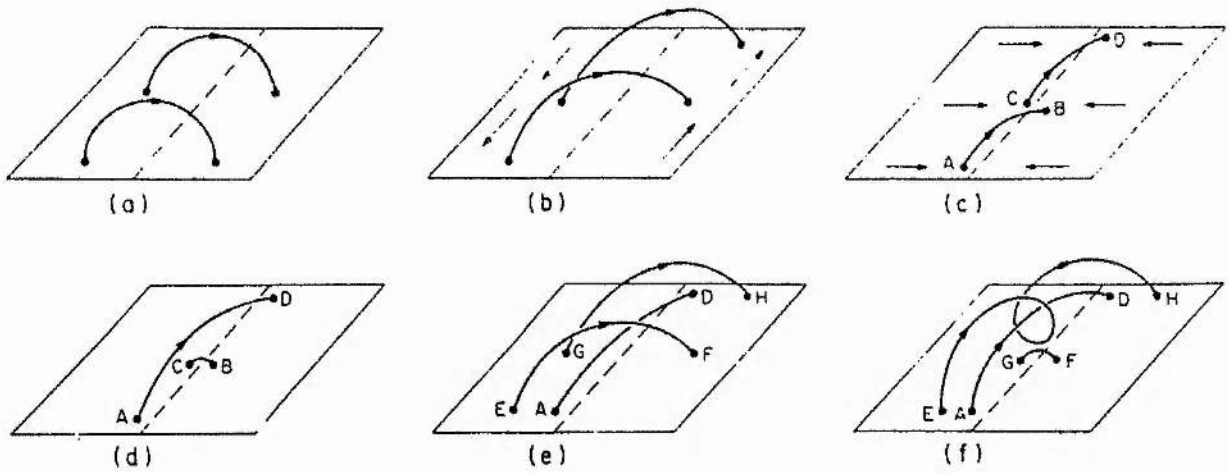

Figure 3.13: The Van Ballegooijen and Martens model to obtain helical field lines. (a) The initial potential field. (b) Photospheric motions parallel, but oppositely directed on either side, produce sheared arcades. (c) Converging flows increase the shear. (d) Reconnection produces a long loop AD and a short one BC, which submerges. (e) Overlying loops converge towards the neutral line. (f) Reconnection leads to a helical field line EH and a small loop FG, which again submerges. (From Van Ballegooijen and Martens, 1989)

that model, the prominence sheet is suspended in a horizontal tube of twisted force-free magnetic field and this flux tube is then matched onto the untwisted coronal field. The prominence sheet is everywhere in local equilibrium; the self-pinching has been avoided by a strong enough background field. However, the description of the magnetic field will give an infinite current density at the ends of the current sheet.

Recently, Low and Hundhausen (1995) looked at the magnetic properties of a quiescent prominence as part of a larger coronal structure, made up of the prominence, the cavity commonly observed around a prominence, and the helmet streamer above them. Extending Low's prominence model (1993) they identify the flux tube as the cavity in the corona and as the filament channel in the chromosphere. They show that the manifestation of the magnetic flux tube is more fundamental than the prominence, since every prominence is in a filament channel, yet not all channels have prominences.

A quite different possibility to achieve inverse polarity configurations was only very recently proposed by Antiochos, Dahlburg and Klimchuk (1994). Significant variations along the prominence length and a strongly sheared magnetic field near the polarity inversion line lead to dip formation for both normal and inverse polarity. Their I-type model is not helical as in the previous models of Priest, Hood and Anzer (1989), and Van Ballegooijen and Martens (1989). Whether this model can reproduce the observed distribution of prominence material has yet to be investigated. The model also predicts both normal (for low lying field lines) and inverse polarity in a single prominence.

Chapter 4

The Numerical Code

The numerical code, initially developed by R. A. S. Fiedler, used throughout this thesis for solving the Grad-Shafranov equation, is a nonlinear multigrid algorithm with finite difference method. Elliptic and hyperbolic partial differential equations are at the heart of most mathematical models used in physics and engineering, but give rise to extensive computations. Multigrid methods are a prime source of important advances in algorithmic efficiency. Essentially, the multigrid principle is to approximate the smooth (long wavelength) part of the error on coarser grids, while the non-smooth part is reduced with a small number of iterations with a basic iterative method on the fine grid. For a general introduction to multigrid methods see, for example, Brandt (1977), Briggs (1987), Stüben and Trottenberg (1982), or Wesseling (1992).

Convergence properties of finite difference and finite element relaxation techniques degrade with the number of algebraic equations required to be solved. Short wavelength error components, which are only coupled over a few neighbouring nodes, reduce very quickly, while the long wavelength error components are hardly effected at all and persist for many iterations. Thus, relaxation tends to smooth the error rather than reducing it.

Nested iteration, a technique to improve convergence, finds a solution on a coarse grid and then interpolates it onto a finer grid, repeating the procedure until the finest grid is reached. However, problems arise because in the interpolation stage

errors are introduced again. Although the short wavelength components of the error are eliminated quickly, the long wavelength components persist again and the initially good convergence stalls.

In multigrid methods we recognise the relationships between the representation of our equations on the various grids. By transferring the errors in fine grids to coarse grids in the correct way, troublesome long wavelength components are eliminated, since on coarse grids they are seen as short wavelength errors.

For MHD equilibria (see also Fiedler, 1992) we have considered the elliptic partial differential equation on the unit square domain $\Omega = (0,1) \times (0,1)$

$$\frac{\partial^2 A}{\partial x^2} + \frac{\partial^2 A}{\partial y^2} + f(A) = 0, \tag{4.1}$$

where $f(A)$ is possibly nonlinear. The standard second order accurate finite difference approximation on a square mesh of size $h = 1/n$, with n being the number of intervals into which the domain is divided, applied at the points $(x_i, y_j) = (ih, jh)$, gives us the following set of simultaneous nonlinear algebraic equations:

$$\begin{aligned} N(A_{ij}) &= -4A_{ij} + A_{i-1j} + A_{i+1j} + A_{ij-1} + A_{ij+1} + h^2 f(A_{ij}) = 0 \\ &\quad \text{for } 1 \leq i,j \leq n-1 \end{aligned} \tag{4.2}$$

A standard approach for solving such systems is to employ a Newton type algorithm. Expanding to first order, we seek corrections ϵ^{n+1} to some approximate solution A^n satisfying

$$\begin{aligned} L(\epsilon_{ij}^{n+1}) &= -4\epsilon_{ij}^{n+1} + \epsilon_{i-1j}^{n+1} + \epsilon_{i+1j}^{n+1} + \epsilon_{ij-1}^{n+1} + \epsilon_{ij+1}^{n+1} + h^2 \frac{\partial f(A_{ij}^n)}{\partial A_{ij}} \epsilon_{ij}^{n+1} = -N(A_{ij}^n) \\ &\quad \text{for } 1 \leq i,j \leq n-1 \end{aligned} \tag{4.3}$$

While it is possible to solve this linear system directly, the time taken for large systems to reach a solution was found unacceptably slow. In practice though it was not necessary to completely solve the above system. Iterative methods may be used to solve the system to some suitable accuracy and still retain the good convergence properties of Newton's method.

Rather than solving the global system (4.3) and then adding the correction terms we may employ an iterative nonlinear Gauss-Seidel (NLGS) procedure whereby

we step through the grid one node at a time and solve the corresponding linearised equation subject to the constraint that $\epsilon_{pq}^{n+1} = 0$ for $p \neq i$ or $q \neq j$. We then add the correction to A_{ij} immediately and then proceed to the next point. Although each sweep through the grid is accomplished very quickly, it is found that the convergence rate behaves like $1 - O(h^2)$ or worse and the process soon stalls if we even have a moderate number of points. It is found, both numerically and analytically, that while the short wavelength Fourier modes of the error, up to $4h$ in size, are reduced quite quickly (about an order of magnitude in three or four sweeps), long wavelength errors are hardly reduced at all resulting in a slow convergence. Thus, NLGS is a good smoother of the error and a suitable candidate for use in a multigrid procedure.

Our multigrid procedure begins with one sweep of NLGS to the system (4.3) on the original grid. We then restrict the solution and the residual of (4.2) to a coarser grid of size $2h$ by straight injection. We then apply a sweep of NLGS to our coarse grid approximation in order to reduce the errors between $4h$ and $8h$. We repeat this procedure of restriction and smoothing until we are unable to continue (or in some cases until NLGS no longer functions as a smoother). On this coarsest grid we apply NLGS until the residual is reduced to some specified tolerance. This is quite cheap since there are only a few nodes in our coarsest grid. We now return to our finest grid by bilinearly interpolating our corrections from one grid and adding them to the solution on the next finest. It is found that this prolongation introduces a small amount of short wavelength error which is easily eliminated by a further application of NLGS before interpolating and adding to the next finest grid. We continue until we return to our original fine grid. Each sweep of this so called *V cycle* requires about as much work as three sweeps of NLGS but is able to reduce all of the error wavelengths in an almost uniform manner. More complex combinations of smoothing, restriction and prolongation are possible but this was found to be unnecessary in the cases which we considered.

Chapter 5

The magnetic field structure of inverse polarity prominences due to imposed axial current distributions

5.1 Introduction

In this chapter numerical calculations of two-dimensional force-free magnetic fields are presented, investigating whether suitable magnetic field arcades for prominences of inverse polarity can be obtained. Since the prominence must form in a low-beta coronal plasma, the pre-prominence magnetic field must have the correct topology for an inverse polarity configuration *before* the formation of the prominence itself. We investigate how various axial current distributions effect coronal arcades and whether neutral points can form.

As recently shown by Anzer (1993), at present no physically realistic models exist for inverse polarity prominences. Therefore we impose current distributions and investigate whether they can form an inverse polarity magnetic field structure. We do not look at the evolution of such fields; this can be a subject for future work once models without unphysical characteristics have been demonstrated. The formation of

I-type polarities requires both shearing and converging photospheric motions as well as reconnection (Van Vallegooijen and Martens, 1989).

5.2 Mathematical Description of the Model

We use a Cartesian coordinate system (x, y, z) in which the corona occupies the half-space $\{-\infty < x < \infty, -\infty < y < \infty, z > 0\}$ above the photosphere $\{z = 0\}$. All physical quantities are assumed to be invariant along the longitudinal axis of the prominence (x-axis), and thus we need only to consider a single plane perpendicular to the prominence axis $\{x = 0, -\infty < y < \infty, 0 < z < \infty\}$. The prominence, in general, is represented by an infinitesimally thin vertical sheet of mass and current. However, since the prominence must form in a low-β coronal plasma, the magnetic field must have the correct topology for an inverse polarity configuration *before the formation of the prominence itself.* In addition, this magnetic configuration must also be in equilibrium. Only after that can a prominence form! The prominence as it begins to form cannot modify the field structure, although local variations may occur when it is fully formed. Therefore we proceed by investigating the conditions for which the coronal magnetic field has a general inverse polarity topology without the prominence sheet.

The coronal field now is considered to vary slowly in time since the global appearance of a prominence changes little over a period of days. The force of gravity may be neglected outside the prominence, since the height of a prominence is much smaller than the coronal scale height. The field can be expressed by the *Grad-Shafranov equation* of magnetohydrostatics (2.35). This is a single, non-linear, elliptic, partial differential equation with the non-linearity appearing in the term involving the axial current density and the real problem in modelling inverse polarity prominences is to know the functional form of this axial current. In principle this should be determined from the photospheric foot point motions (Jockers, 1978). However, in this chapter we investigate the functional forms of $B_x(A)$ that generate inverse polarity configurations without worrying at this stage about the foot point connectivity. We have a topological look at the current profiles, not an evolutionary one.

Let B_x be some function of A and λ, where λ is a positive parameter, so that

$$\frac{d}{dA}\left(\frac{1}{2}B_x^2(A) + \mu\, p(A)\right) = \lambda f(A). \tag{5.1}$$

It is the aim of this research to determine forms of the axial current distribution $f(A)$ that generate inverse polarity configurations.

5.3 The Linear Approximation

At first we set up a simplified model in terms of a small displacement about a background potential magnetic field. In this manner a linear equation can be obtained and solved analytically in a simple manner. The modified field is investigated to see if X-type and O-type neutral points are present. This process allows one to deduce the types of current profiles that might generate inverse magnetic field configurations.

We choose the function $f(A)$ as (Amari, et al., 1991)

$$f(A) = (A + bA^3) := f_b(A) \tag{5.2}$$

in order to examine a possible non-linear force-free field. b is the parameter measuring the non-linearity of the shear profile.

The force-free field is now considered to be a small perturbation from a potential field. Expressing A as

$$A = A_0 + \epsilon A_1,$$

with $\epsilon << 1$, the perturbed field satisfies

$$\nabla^2 A_1 = -f(A_0). \tag{5.3}$$

With the unperturbed potential field chosen to be

$$A_0 = \cos(y)e^{-z} \tag{5.4}$$

and boundary conditions $A_1 = 0$ at $z = 0$, $z = \infty$ and $y = \pm\pi/2$, the solution to equation (5.3) is

$$A_1 = \frac{\cos(y)}{2}\left[ze^{-z} + \frac{3}{16}b\left(e^{-z} - e^{-3z}\right)\right] + \frac{1}{24}b\cos(3y)ze^{-3z}. \tag{5.5}$$

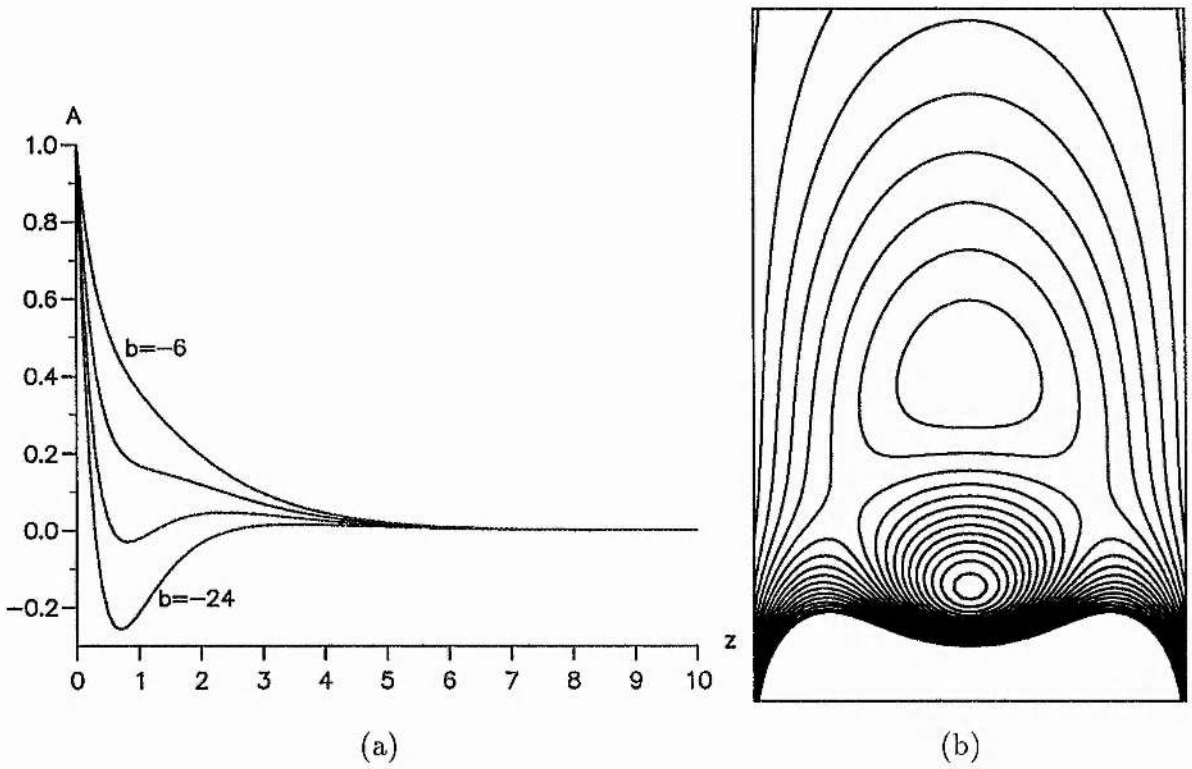

Figure 5.1: (a) The flux function A with height at $y = 0$, for $b = -6, -12, -18, -24$. (b) Magnetic field lines from contours of A between 0 and 0.1 at $b = -18$ for $\epsilon = 1$.

In Figure 5.1a the flux function A as a function of z at $y = 0$ is shown for various values of b. We see that for $b = -18$ the flux function shows the most appropriate form. In Figure 5.1b the overall magnetic field is shown for this case. Two regions of detached field lines are clearly seen with two X-type neutral points situated away from the vertical axis and two O-type neutral points. A prominence forming between the O-type neutral points would be of the inverse polarity type whereas below the lower O-type neutral point it would be a prominence of normal polarity.

Another possibility is to vary the function $f(A)$. With b, c, d, f and g being constants, following functions have also been investigated in the linearisation,

$$f_c(A) = A + bA^3 + cA^5, \tag{5.6}$$

$$f_d(A) = A + dA^5, \tag{5.7}$$

$$f_f(A) = A + fA^7, \tag{5.8}$$

$$f_g(A) = A^3 + gA^5, \tag{5.9}$$

Using the same boundary conditions and the same A_0 as in (5.4), A_1 is then given by

$$\begin{aligned} f_c: \ A_1 &= \frac{\cos(y)}{2}\left[ze^{-z} + \frac{3}{16}b\left(e^{-z} - e^{-3z}\right) + \frac{7}{96}c\left(e^{-z} - e^{-5z}\right)\right] + \\ &+ \frac{\cos(3y)}{8}\left[\frac{1}{3}bze^{-3z} + \frac{1}{4}c\left(e^{-3z} - e^{-5z}\right)\right] + \\ &+ \frac{\cos(5y)}{80}\left[cze^{-5z}\right], \end{aligned} \tag{5.10}$$

$$\begin{aligned} f_d: \ A_1 &= \frac{\cos(y)}{2}\left[ze^{-z} + \frac{5}{192}d\left(e^{-z} - e^{-5z}\right)\right] + \\ &+ \cos(3y)\left[\frac{5}{256}d\left(e^{-3z} - e^{-5z}\right)\right] + \cos(5y)\left[\frac{1}{160}dze^{-5z}\right], \end{aligned} \tag{5.11}$$

$$\begin{aligned} f_f: \ A_1 &= \frac{\cos(y)}{2}\left[ze^{-z} + \frac{35}{3072}f\left(e^{-z} - e^{-7z}\right)\right] + \\ &+ \cos(3y)\left[\frac{21}{2560}f\left(e^{-3z} - e^{-7z}\right)\right] + \\ &+ \cos(5y)\left[\frac{7}{1536}f\left(e^{-5z} - e^{-7z}\right)\right] + \cos(7y)\left[\frac{1}{896}fze^{-7z}\right], \end{aligned} \tag{5.12}$$

$$\begin{aligned} f_g: \ A_1 &= \cos(y)\left[\frac{3}{32}\left(e^{-z} - e^{-3z}\right) + \frac{5}{192}g\left(e^{-z} - e^{-5z}\right)\right] + \\ &+ \cos(3y)\left[\frac{1}{24}ze^{-3z} + \frac{5}{256}g\left(e^{-3z} - e^{-5z}\right)\right] + \end{aligned}$$

$$+ \quad \cos(5y)\left[\frac{1}{160}gze^{-5z}\right]. \tag{5.13}$$

Varying the constant c in (5.10) only gives a slight improvement to (5.5). We get a more profound shape of A with a $c = -1$. However, the overall coronal field does not differ much to the field shown in Figure 5.1b for $f_b(A)$, again displaying two X-type neutral points situated away from the vertical axis and two O-type neutral points along the vertical axis.

For low ϵ-values the effects which may create an inverse polarity configuration are not strong enough. Therefore a large value of ϵ has been used, although it probably invalidates the linearisation procedure used here. However, the main aim of this approach was only to find the form of the flux function that may create an inverse polarity topology.

The behaviour of the functions $f_d(A)$, $f_f(A)$ and $f_g(A)$ is similar. Very high values for the constants are needed to get any change from the potential arcades, then displaying an O-type neutral point very close to the photosphere only.

It was realised that to produce neutral points requires a substantial departure from the potential state and this requires a large displacement. In other words it is not clear whether the linear approximation is valid or not (see also Amari, et al., 1991). Thus, it is necessary to solve the full non-linear Grad-Shafranov equation.

5.4 Boundary Functions of the Numerical Code

A computer program (see chapter 4) based on a nonlinear, multigrid, finite difference method has been used to obtain solutions of the Grad-Shafranov equation (2.34). Three boundary functions $A(y,0) = g(y)$ at the photosphere have been tried, namely

$$\tilde{g}(y) = (1-y)(1+y), \tag{5.14}$$

$$g(y) = 1.04\left(\cos(\frac{\pi y}{2}) + \eta_3\cos(\frac{3\pi y}{2}) + \eta_5\cos(\frac{5\pi y}{2})\right), \tag{5.15}$$

$$\bar{g}(y) = \frac{\ln(1+y^2)}{\ln 2}, \tag{5.16}$$

where (5.15) is described by Amari and Aly (1992) with $\eta_3 = -0.15$, $\eta_5 = 0.115$ for inverse polarity prominences and (5.16) by Low (1977) for an semi infinite plasma. (5.15) and (5.16) have been rescaled, so that the same amount of flux threads the photosphere for all three boundary functions.

The line of sight magnetic field at the photosphere is, $B_z = -dg/dy$. Hence,

$$B_z = \begin{cases} 2y & \text{for (2)}, \\ 0.52\,\pi(\sin\frac{\pi y}{2} + 3\eta_3 \sin\frac{3\pi y}{2} + 5\eta_5 \sin\frac{5\pi}{2}) & \text{for (3)}, \\ -\frac{1}{\ln 2}\,\frac{2y}{1+y^2} & \text{for (4)}. \end{cases} \tag{5.17}$$

These choices cover a wide range of possible profiles.

The other boundaries are taken as field lines so that

$$A(\pm 1, z) = A(\pm 1, 0) \qquad \text{and} \qquad A(y, h) = A(\pm 1, 0).$$

The side boundaries simulate neighbouring active regions which are preventing the coronal arcade from expanding to infinity.

The height of the upper boundary has been varied by altering the aspect ratio of the numerical box to see the effect of constraining the field. However, as the height is increased, there is no topological difference in the resulting field and especially in the lower half part, where the neutral points form. In the upper half of the larger numerical box the field lines stretch more to fill the space, but the overall topological configuration remains the same.

Therefore the height of the numerical box used in this paper has been taken twice as high as it is long, hence the numerical box is scaled to $-1 < y < 1$ and $0 < z < 4$. The same values of A are used so that the influence of the axial current on a particular field line can be seen.

5.5 Axial Current Profiles

A variety of different current profiles that may give rise to inverse polarity structures has been investigated, namely

Polynomials	$f(A) = A^n(1 - c_m A^m)$
Trigonometric Functions	$f(A) = \cos\left(\pi \frac{A - A_0}{2\,\delta A}\right)$
Exponential Function	$f(A) = e^{-2A}$

The behaviour of the magnetic field lines depends on the value of $A = A_{j=0}$ that corresponds to the value of A, and hence the field line, on which the axial current, j_x, is zero and whether $A_{j=0}$ is smaller, equal or larger than the maximum A-value on the photosphere, A^{ph}_{max}, for the chosen boundary function.

5.5.1 Polynomials

$$f(A) = A^n(1 - c_m A^m) \tag{5.18}$$

with c_m a constant. Increasing n and m allows the axial current to become strongly peaked near $A = (\frac{n}{(n+m)c_m})^{1/m}$ and suitable choices of c_m can either keep the current of one sign or allow negative currents as well as positive currents.

Negative values of c_m:

For negative values of the constant c_m the program fails to converge when λ has a certain critical value λ^*. Depending on the form of $f(A)$ the following properties for solutions to the Grad-Shafranov equation (2.34) hold if Dirichlet boundary conditions are imposed. (see e.g. Birn and Schindler (1981))

1. For $\frac{\partial f(A)}{\partial A} \leq 0$ equation (2.34) has a unique solution for every $\lambda \geq 0$;
2. for $f \geq 0$, $\frac{\partial f(A)}{\partial A} \geq 0$, $\frac{\partial^2 f(A)}{\partial A^2} > 0$ (or equivalently $f \leq 0$, $\frac{\partial f(A)}{\partial A} \geq 0$, $\frac{\partial^2 f(A)}{\partial A^2} < 0$) a catastrophe point λ^* occurs and there is no neighbouring solution to equation (2.34) for $\lambda > \lambda^*$.

If c_m is negative, we can rewrite equation (5.18) as

$$f(A) = A^n + kA^l$$

with $l = m + n$ and k is a positive constant. Since A is positive, $f(A)$ is positive and so are its first and second derivatives. Therefore case 2 applies and we have only solutions to equation (2.34) for $\lambda < \lambda^*$.

For boundary function $\tilde{g}$ (5.14) we obtain, for $c_2 = -1$ and $c_2 = -0.1$, normal polarity arcades, which, for larger values of λ, show a tendency to forming closed loops. But before these structures can develop and an O-type neutral point can form, the catastrophe point is reached and no neighbouring solution is found anymore.

Positive values of c_m:

For a positive constant c_m, $f(A)$ and its derivatives can be either positive or negative depending on its respective A-value. So neither set of the Dirichlet boundary conditions is satisfied. We cannot say whether solutions for equation (2.34) are guaranteed. Fortunately, we find that the code converges for small powers of n.

For $n = 1$ five functions with $m = 1, 2, 3, 4$ and 6 were investigated and the same pattern appeared, therefore we concentrate on following one m-value only, namely $m = 2$.

For polynomials the value $A_{j=0}$ depends inversely on the value of c_m.

$A_{j=0}$ is smaller than A^{ph}_{max}

In Figure 5.2 a large value of c_m has been used, namely $c_2 = 18$, for boundary function $\tilde{g}$ (5.14). Thus the axial current becomes zero for $A \cong 0.24$. For larger values of A the current changes sign and becomes negative; a downwards acting Lorentz-force results. Smaller A-values produce a positive axial current and an upwards directed Lorentz-force. So the field lines at the outer edge, from $A = 0$ to $A = A_{j=0}$, rise, while the other ones for $A > A_{j=0}$ are pushed down (see Figure 5.2a). An increased λ, hence a stronger current and a bigger Lorentz-force, pushes the field lines up or down by a larger amount, respectively, as seen in Figure 5.2b. Therefore more of the middle area turns to the value $A = A_{j=0}$. This can be seen clearly in Figure 5.3a for the corresponding A as a function of z at $y = 0$. Since $2\mu j_x = dB_x^2/dA$,

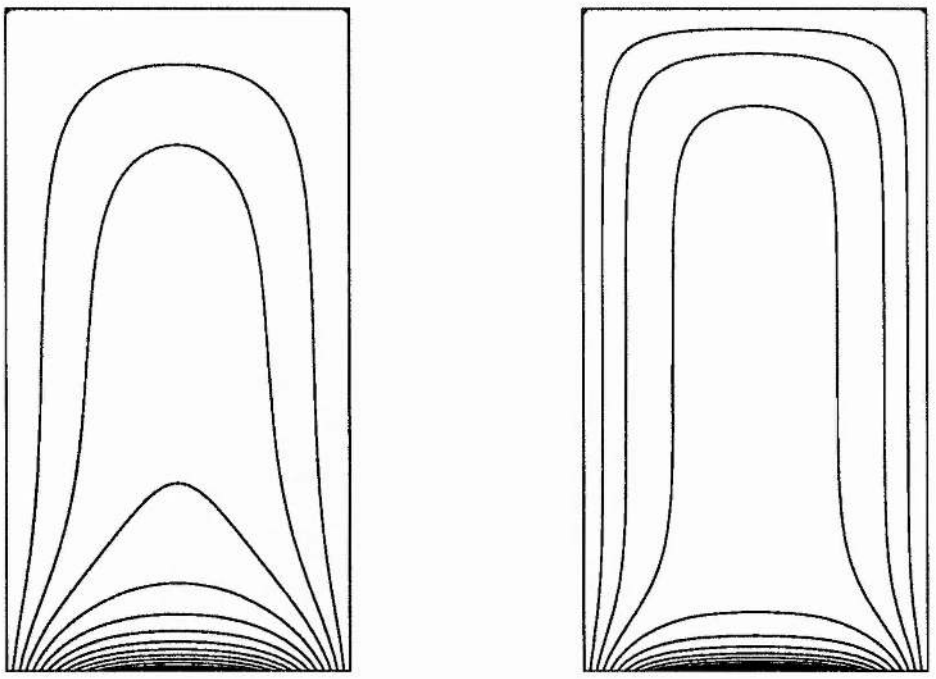

(a) (b)

Figure 5.2: The magnetic field line structure for $\lambda f(A) = \lambda A(1 - c_2 A^2)$, $c_2 = 18$, for boundary function $\tilde{g}$. (a) $\lambda = 5$, (b) $\lambda = 15$.

(a)

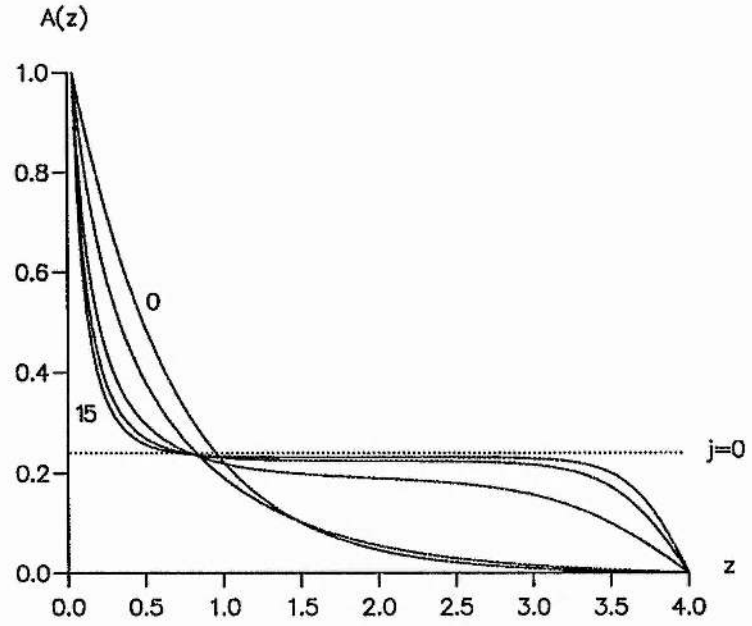

(b)

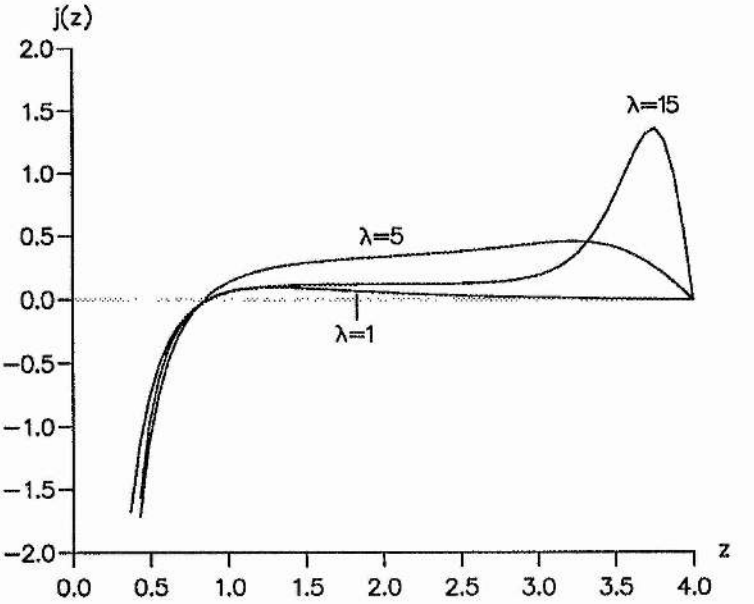

Figure 5.3: $\lambda f(A) = \lambda A(1 - c_2 A^2)$, $c_2 = 18$, for boundary function $\tilde{g}$. (a) Corresponding $A(z)$ at $y = 0$ for $\lambda = 0, 1, 5, 10, 15$. (b) Corresponding current density $j(z)$ at $y = 0$ for $\lambda = 1, 5, 15$.

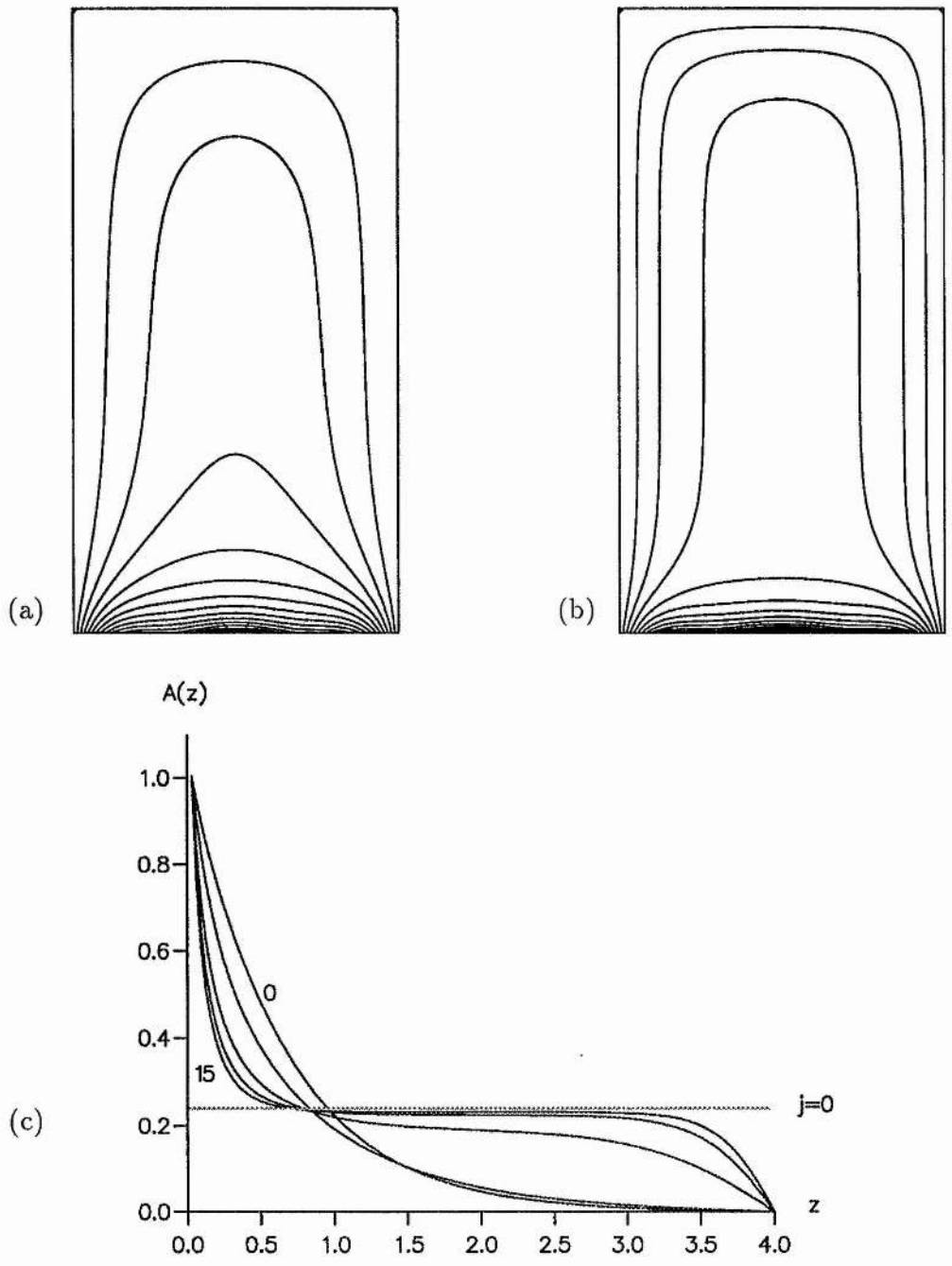

Figure 5.4: The magnetic field line structure for $\lambda f(A) = \lambda A(1 - c_2 A^2)$, $c_2 = 18$, for boundary function g. (a) $\lambda = 5$, (b) $\lambda = 15$. (c) Corresponding $A(z)$ at $y = 0$ for $\lambda = 0, 1, 5, 10, 15$.

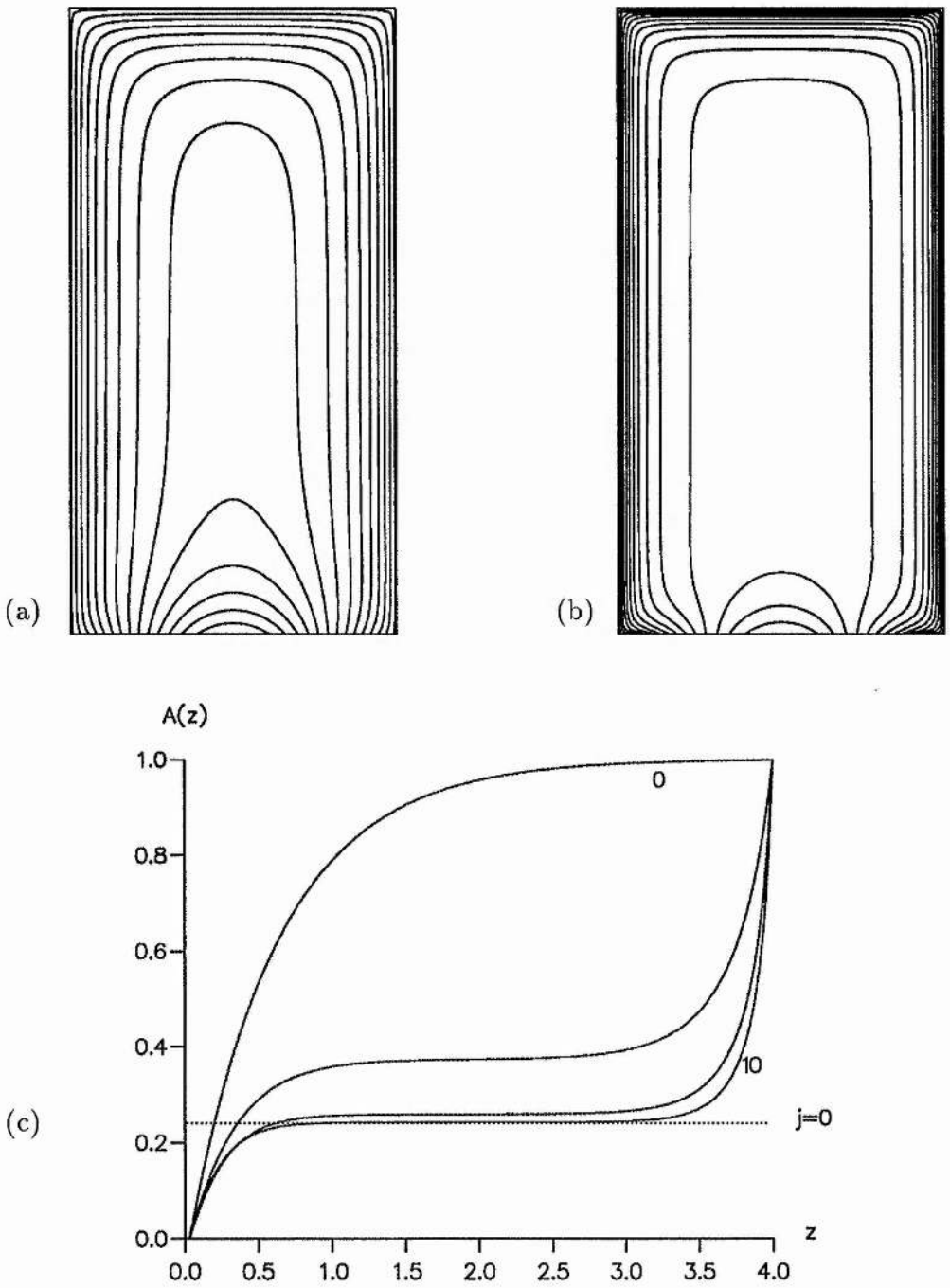

Figure 5.5: The magnetic field line structure for $\lambda f(A) = \lambda A(1 - c_2 A^2)$, $c_2 = 18$, for boundary function $\tilde{g}$. (a) $\lambda = 1$, (b) $\lambda = 10$. (c) Corresponding $A(z)$ at $y = 0$ for $\lambda = 0, 1, 5, 10$.

$j_x = 0$ corresponds to the maximum of B_x^2. Thus, the axial magnetic pressure $B_x^2/2\mu$ is responsible for pushing the field lines apart. The behaviour of the current density j as a function of height at $y = 0$ is portrayed in Figure 5.3b. It clearly shows how the current switches sign, and how for high λs it stays at an even level for the middle area.

Boundary function g (5.15) - except from a small lateral pinch to the field lines due to its plateau-shape - causes the same configurations of magnetic field lines as boundary function $\tilde{g}$ (5.14); as can be seen in figures 5.4 and 5.4c.

Boundary function $\bar{g}$ (5.16) is different in the sense that the minimum value for A is now at $y = 0, z = 0$ while A_{max}^{ph} is located in the corners and around the box. But since for this boundary function the line-of-sight magnetic field is negative, we have again a downwards and upwards directed Lorentz-force and the same behaviour as for boundary functions $\tilde{g}$ (5.14) or g (5.15), respectively. (See Figure 5.5)

The magnetic configurations we get for all boundary functions with practically no poloidal magnetic field existing in the middle of the box are a result of the choice of the constant c_m, which allows the axial current j_x to change sign and to create differently directed Lorentz-forces.

$A_{j=0}$ is equal to A_{max}^{ph}

Since now all the values of A given by the boundary function are smaller (or equal, respectively) than the A-value for which the current becomes zero, the current never changes sign and always stays positive, which means an only upwards directed Lorentz-force. So all field lines rise, the middle ones though less according to their lower current value (see Figure 5.6a). Eventually the highly stretched field lines come close together due to horizontal magnetic pressure and an X-type neutral point can form (Figure 5.6b), and consequently an O-type neutral point as well. Of course, it is assumed that field line reconnection has occurred through the small but finite resistivity.

For an X-type neutral point the flux function A as a function of z at $y = 0$ should have a minimum. In Figure 5.6c for $\lambda \geq 10$ a small dip can be seen before A

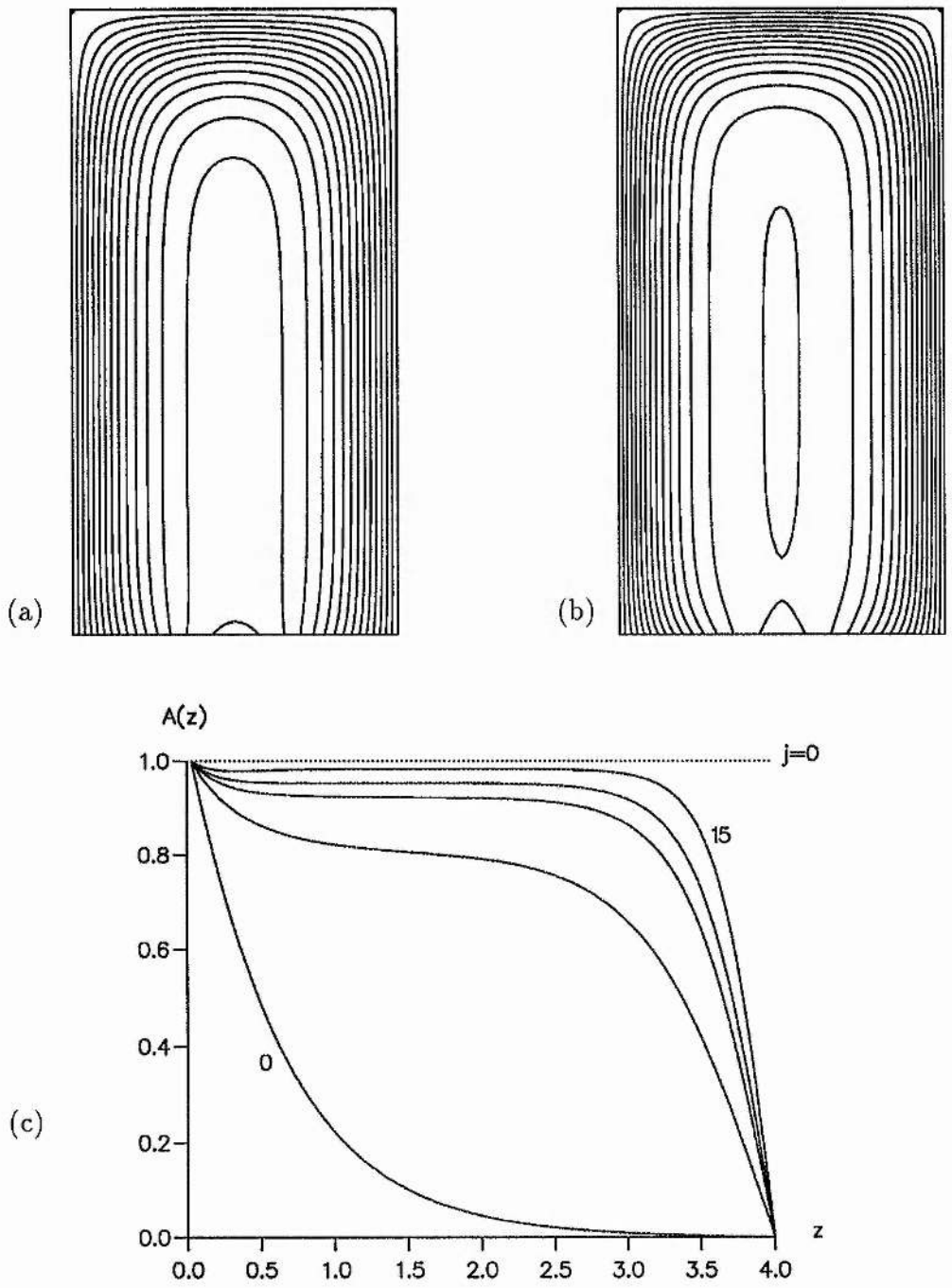

Figure 5.6: The magnetic field line structure for $\lambda f(A) = \lambda A(1 - c_2 A^2)$, $c_2 = 1$, for boundary function $\tilde{g}$. (a) $\lambda = 10$, (b) $\lambda = 15$. (c) Corresponding $A(z)$ at $y = 0$ for $\lambda = 0, 5, 8, 10, 15$.

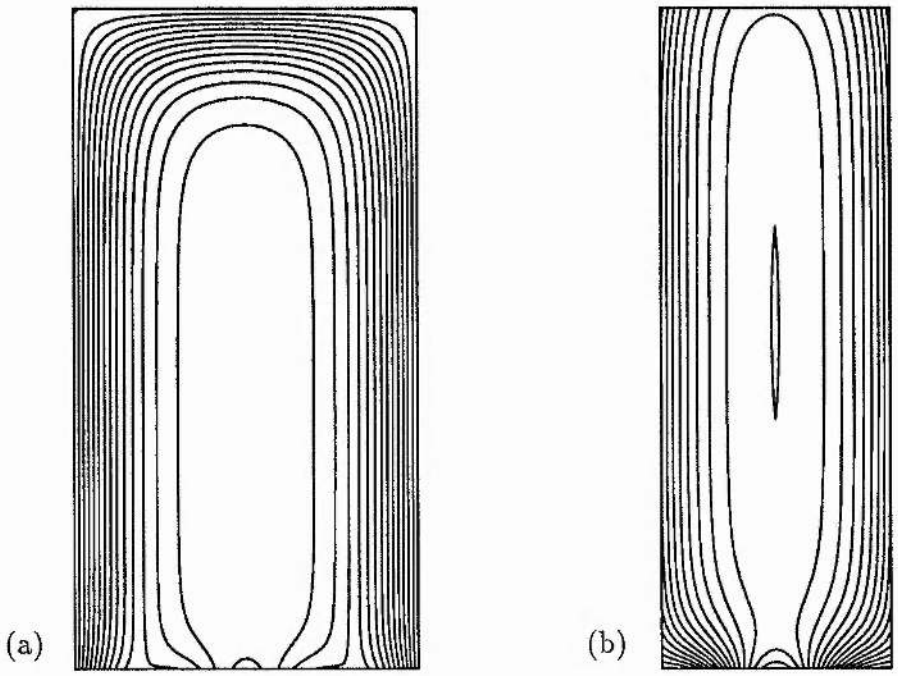

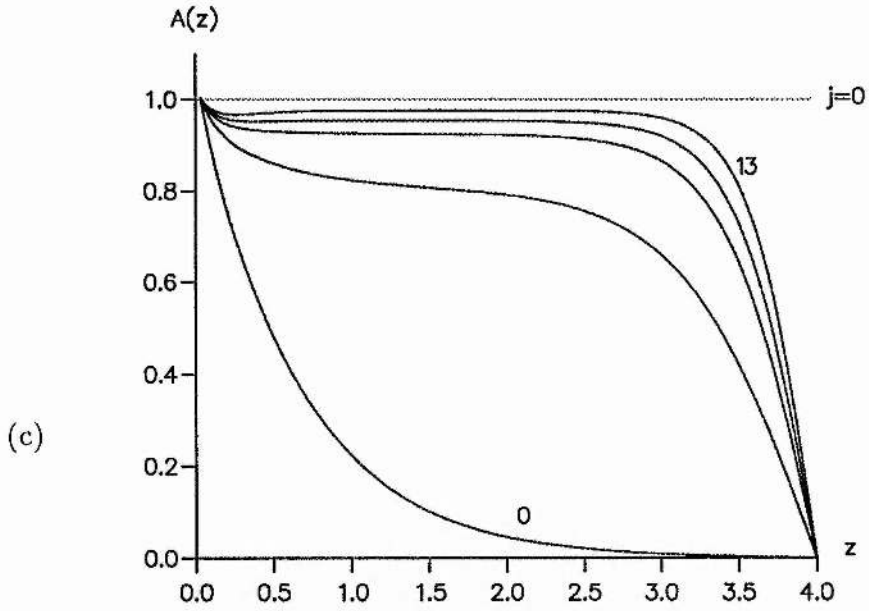

Figure 5.7: The magnetic field line structure for $\lambda f(A) = \lambda A(1 - c_2 A^2)$, $c_2 = 1$, for boundary function g. (a) $\lambda = 13$, (b) $\lambda = 13$ expanded scale $[-0.5 < y < 0.5$, $0 < z < 3]$. (c) Corresponding $A(z)$ at $y = 0$ for $\lambda = 0, 5, 8, 10, 13$.

approaches the $A_{j=0}$-value. However, since the $A_{j=0}$-value is the same as A^{ph}_{max}, the maximum value of the flux function is the one on the photosphere, although neutral points are present. Therefore the X-type neutral point will be conserved, but always stays very close to the photosphere.

The particular shape of boundary function g (5.15), which through its plateau shaped form is responsible for the lateral pinch to the field lines, favours the formation of an X-type neutral point; that can be seen in Figure 5.7 for $\lambda = 13$. The dip in $A(z)$ at $y = 0$ (Figure 5.7c) is therefore more profound as for boundary function $\tilde{g}$; otherwise these two boundary functions show the same behaviour.

Also for boundary function $\bar{g}$ (5.16) the flux function approaches the $A_{j=0}$-value, but does not cross it anymore (Figure 5.8c). The current stays positive. However, due to the negative line-of-sight magnetic field (5.17) a downwards resulting Lorentz-force is created and we obtain normal polarity arcades, slightly pushed together (Figure 5.8).

$A_{j=0}$ is larger than A^{ph}_{max}

Again the current always remains positive and the resulting upwards directed Lorentz-force lets the field lines rise. Since now the value of A for which the current becomes zero is much larger than the maximum A-value on the photosphere, the flux function can easily reach a maximum value and produce an O-type neutral point (Figure 5.9c). Also there is no dip in $A(0, z)$ anymore, so no X-type neutral point should be present as can be seen in Figure 5.9.

The same happens again for boundary function g (5.15). However, its 'pinch-causing' shape is responsible for the short formation of an X-type neutral point very close to photosphere. With a stronger current (increased λ) the boundary function has less influence and the X-type neutral point vanishes.

For boundary function $\bar{g}$ (5.16) we obtain closed field lines over an area of normal polarity arcades (Figure 5.10). Now the constant is decreased enough that the maximum A-value can become bigger than its maximum boundary value of $A^{ph}_{max} = 1$, so the values of $A > A^{ph}_{max} = 1$ form closed contour lines around A_{max},

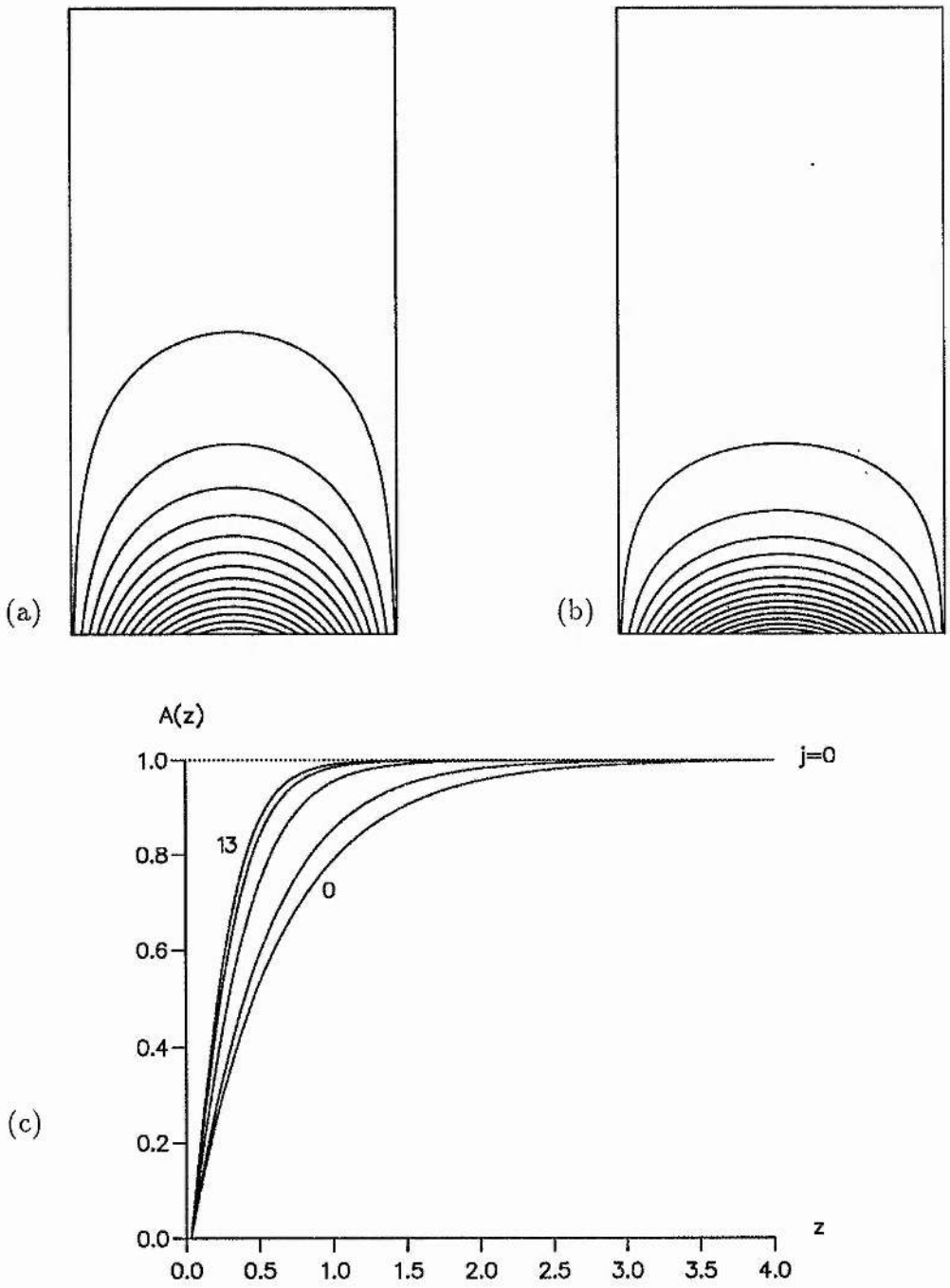

Figure 5.8: The magnetic field line structure for $\lambda f(A) = \lambda A(1 - c_2 A^2)$, $c_2 = 1$, for boundary function $\bar{g}$. (a) $\lambda = 1$, (b) $\lambda = 5$. (c) Corresponding $A(z)$ at $y = 0$ for $\lambda = 0, 1, 5, 10, 13$.

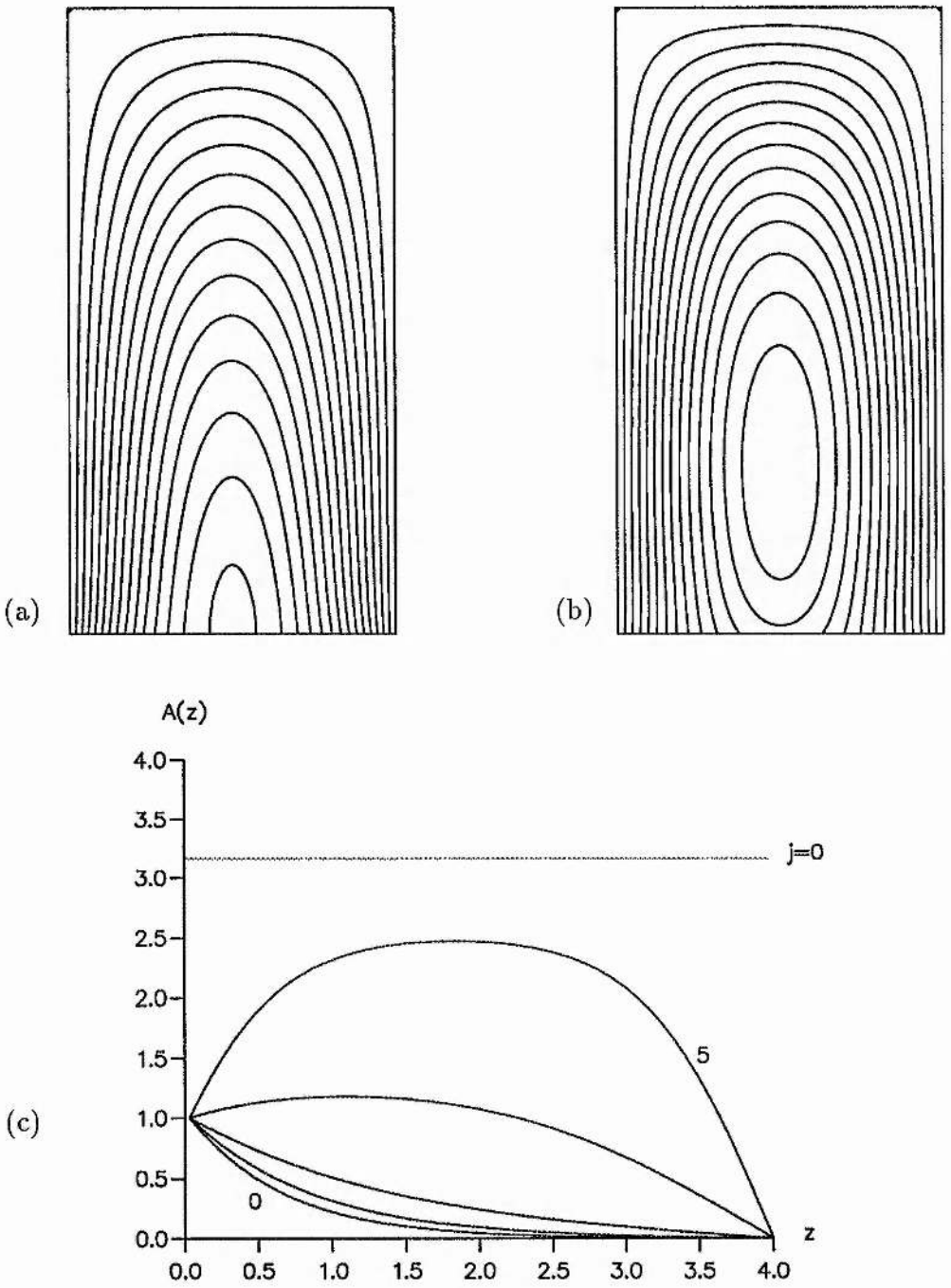

Figure 5.9: The magnetic field line structure for $\lambda f(A) = \lambda A(1 - c_2 A^2)$, $c_2 = 0.1$, for boundary function $\tilde{g}$. (a) $\lambda = 2.73$, (b) $\lambda = 3$. (c) Corresponding $A(z)$ at $y = 0$ for $\lambda = 0, 1, 2, 3, 5$.

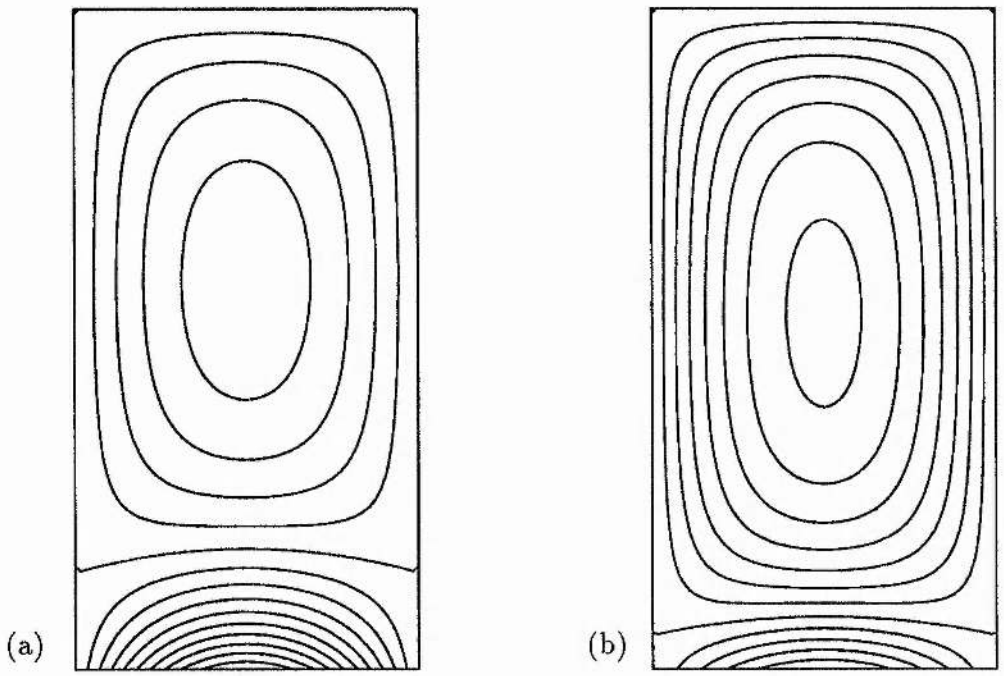

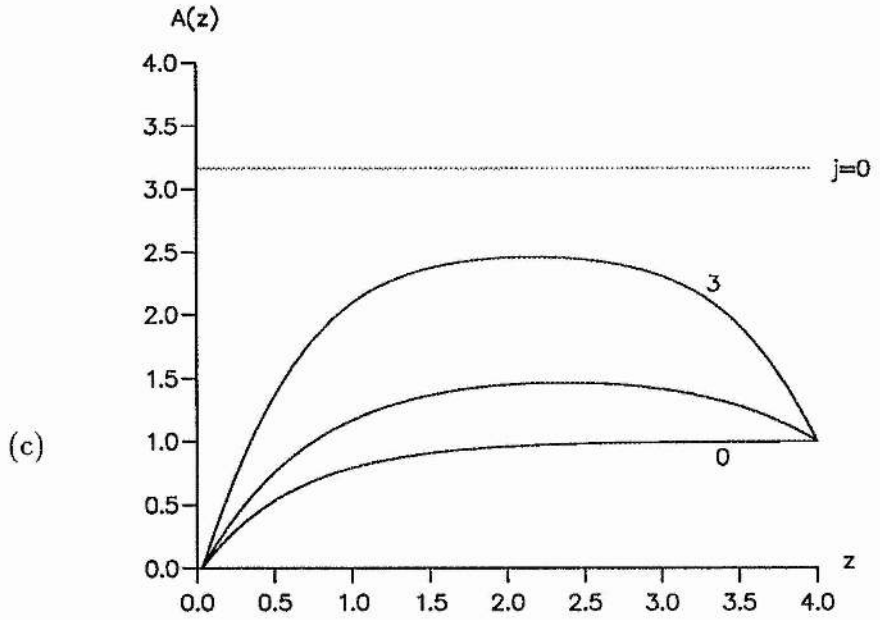

Figure 5.10: The magnetic field line structure for $\lambda f(A) = \lambda A(1 - c_2 A^2)$, $c_2 = 0.1$, for boundary function $\bar{g}$. (a) $\lambda = 1$, (b) $\lambda = 3$. (c) Corresponding $A(z)$ at $y = 0$ for $\lambda = 0, 1, 3$.

while the contours for $A < A^{ph}_{max} = 1$ remain in a squeezed normal arcade structure as in the case for $c_2 = 1$. The flux function has a tendency to reach its $A_{j=0}$-value, but because of its boundary constraints it has to reach back to its A^{ph}_{max}-value. As can be seen in Figure 5.10c even a very small λ-value would change $A(z)$ into a curve with its maximum greater than 1. Therefore, as soon as the current is switched on, the separation line and the closed loops start to form. They are completely detached from the solutions at the bottom of the numerical box.

Higher powers of n

For $n > 1$ the same behaviour for all three boundary functions appeared as it did for $n = 1$, though a stronger current (higher λ) is needed to get the same results.

The bigger the difference between $A_{j=0}$ and A^{ph}_{max} gets, the less likely a structure with an X-type neutral point is to form.

In general the behaviour of polynomials of the form (5.18) for boundary functions (5.14) or (5.15) depends on the value of the constant c_m:

- A high constant forces the axial current to change sign, and the resulting Lorentz-force creates a magnetic field configuration with field lines squeezed to the margins of the numerical box, while the middle area remains mainly without a poloidal magnetic field. Still the whole structure is of normal polarity.

- If the constant is decreased enough, the value of the flux function, which makes the axial current vanish, can reach and exceed the maximum value of A at the boundary. Then the current does not change sign anymore and remains always positive. Inverse polarity structures can now be found, with an X-type neutral point if the difference between these two A-values is small, and with only an O-type neutral point if this difference becomes large enough.

Only for a very small constant c_m is it possible to create a configuration for which the maximum value of the flux function is much smaller than the value at which the axial current becomes zero. Only these structures are able to create inverse polarity configurations.

5.5.2 Trigonometric functions

$$f(A) = \cos\left(\pi \frac{A - A_0}{2\,\delta A}\right) \tag{5.19}$$

with δA and A_0 being constants, simulates a current localised about particular field lines on the photosphere.

Applying Dirichlet Boundary Conditions on function (5.19) proved to be difficult. If we only consider the case $A_{j=0} > A^{ph}_{max}$, the cosine remains in the quadrants I and IV and is always positive. The first derivative of function (5.19) becomes positive for $A < A_0$, but its second derivative is always negative and no solution to the Dirichlet Boundary Conditions is obtained. For $A \geq A_0$ the first derivative of function (5.19) is negative and a unique solution for all λs is guaranteed. So a choice of A_0 being zero or negative would satisfy case 1 for the whole function. Attention should be paid to the fact that $A_{j=0}$ is still much larger than A^{ph}_{max}.

If the limit $A = A_{j=0}$ is much higher than A^{ph}_{max}, again no X-type neutral point is formed and inverse polarity structures with an O-type neutral point alone are obtained. If the limit $A = A_{j=0}$ is smaller than A^{ph}_{max}, again the current changes sign and normal polarity structures, similar to the ones for polynomials with $c_m = 18$, form.

By decreasing the parameter δA the current can be made more localised, but this also decreases the difference between $A_{j=0}$ and A^{ph}_{max}. For $\delta A = 1/2$ and $A_0 = 1/2$ for example $A_{j=0}$ is equal to A^{ph}_{max}. For $\delta A = 1/4$ the current profile is changed to $1 + \cos(\pi \frac{A - A_0}{2\,\delta A})$, otherwise $f(A)$ would be negative. Again $A_{j=0} = A^{ph}_{max}$ and the resulting graphs are similar to the ones obtained for polynomials with $A_{j=0} = A^{ph}_{max}$. Thus, the advantage of a closer localisation is cancelled by the disadvantage of a low $A_{j=0}$-boundary.

The height at which $A_{j=0}$ can be adjusted by choosing appropriate constants ($A_{j=0} = \delta A + A_0$). Once more – as for polynomials (5.18) – it depends on the choice of constants if inverse polarity structures can be obtained.

5.5.3 Exponential functions

$$f(A) = e^{-2A}. \tag{5.20}$$

This axial current profile has been investigated by Low (1977) for an infinite region, unlike the finite region considered here. Since λ is positive, function (5.20) satisfies case 1 for the Dirichlet Boundary Conditions and will have a unique solution for all λs.

For function (5.20) the axial current becomes zero only for infinite A. Therefore the current will always remain positive and will create inverse polarity configurations, independent of the choice of constants whatsoever.

We see (Figure 5.11) by increasing the current (larger λ) that low current profiles form normal polarity arcades, while for a small parameter range in λ inverse polarity arcades with an O-type and an X-type neutral point can form; for any larger λs we find an inverse polarity structure with an O-type neutral point alone.

Figure 5.12 shows how a small deviation of the current value affects the formation of an X-type neutral point, and shows also the corresponding $A(z)$ and how the dip in it vanishes when no X-type neutral point is formed anymore.

Again the same happens when using boundary function g (5.15). For boundary function $\bar{g}$ (5.16) the same magnetic field topology occurs as discussed above for polynomials with $A_{j=0} >> A^{ph}_{max}$.

5.6 Influence of the Numerical Walls

One could argue that the presence of the numerical box might render the obtained results physically unrealistic, since - while the presence of the vertical numerical walls simulates here the presence of adjacent active regions on the solar surface - there are also large, almost field-free regions in between active regions on the sun, allowing the magnetic field to expand freely sideways for some distance.

Taking this into account we widened the box, but restricted the flux, to simulate such a field-free surrounding (using the exponential function (5.20)). However,

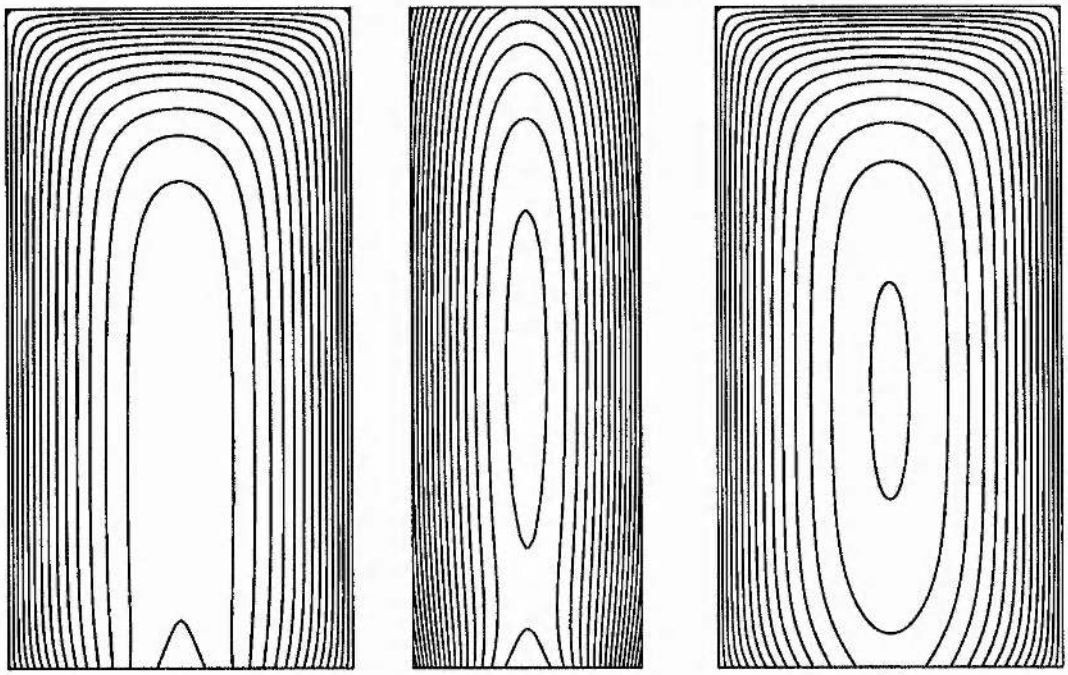

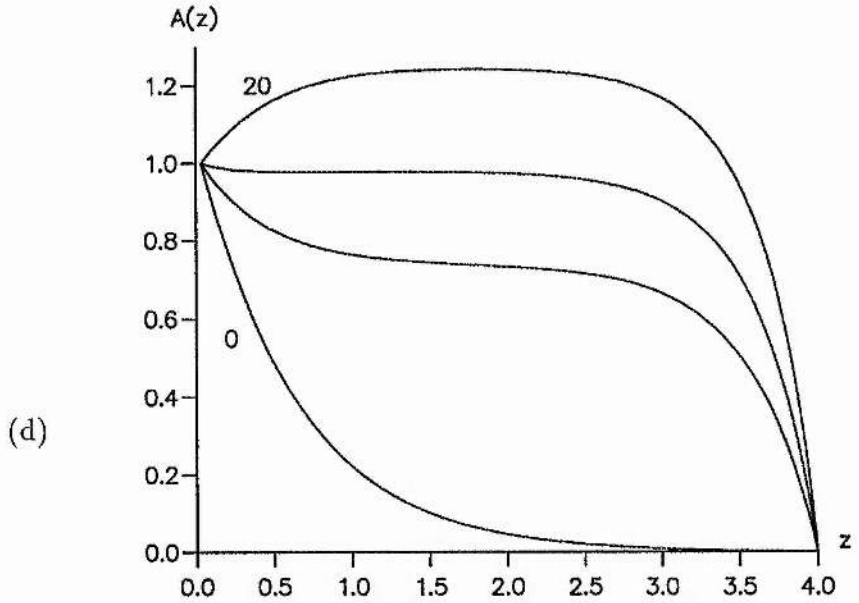

(d)

Figure 5.11: The magnetic field line structure for $\lambda f(A) = \lambda e^{-2A}$, for boundary function $\tilde{g}$. (a) $\lambda = 10$, (b) $\lambda = 10.5$ expanded scale $[-0.5 < y < 0.5,\ 0 < z < 3]$, (c) $\lambda = 15$. (d) Corresponding $A(z)$ at $y = 0$ for $\lambda = 0, 5, 10, 20$.

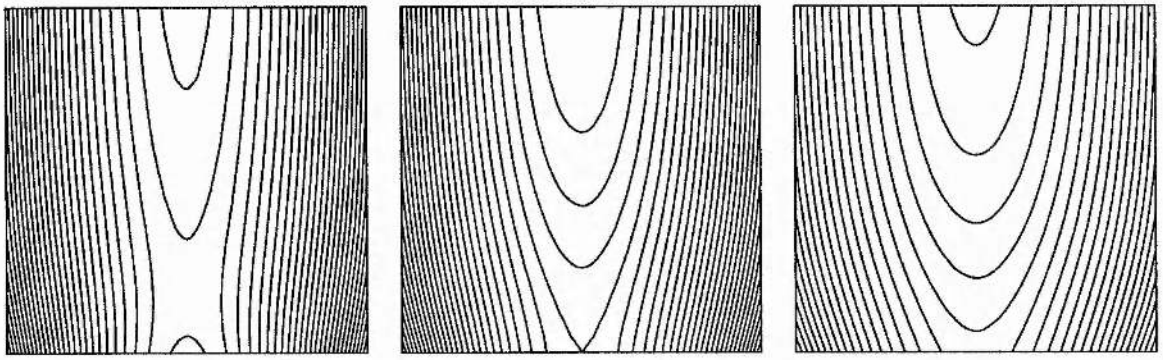

(a) (b) (c)

(d)

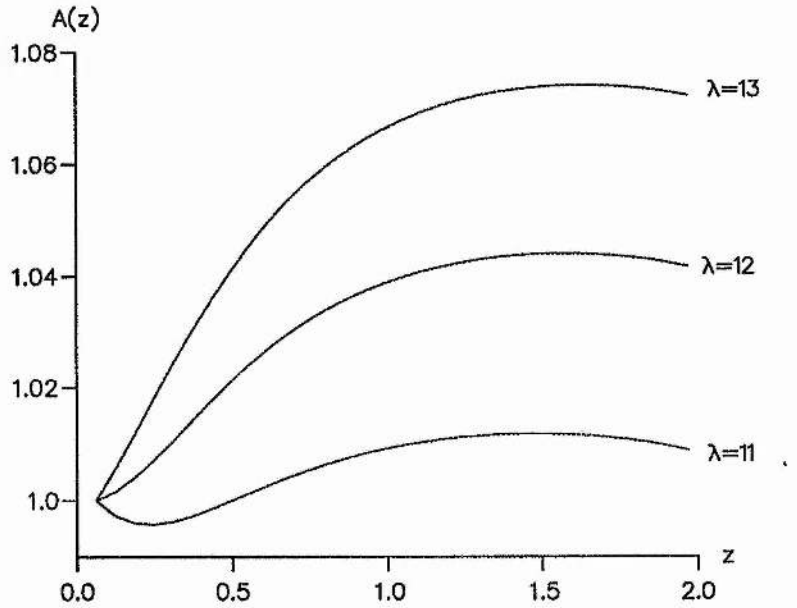

Figure 5.12: The magnetic field line structure for $\lambda f(A) = \lambda e^{-2A}$, for boundary function $\tilde{g}$. (a) $\lambda = 11$, (b) $\lambda = 12$, (c) $\lambda = 13$; all expanded scale $[-0.5 < y < 0.5, 0 < z < 1]$. (d) Corresponding $A(z)$ at $y = 0$. $\lambda = 11, 12, 13$.

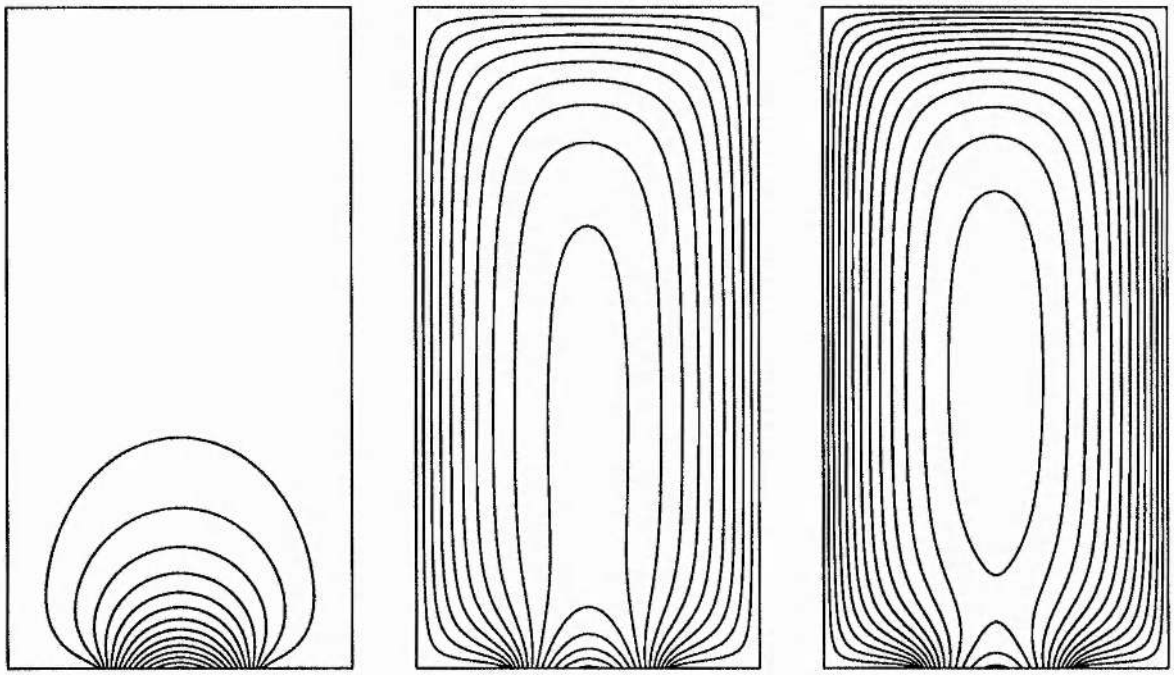

Figure 5.13: The magnetic field line structure for a bigger box $[-2 < y < 2,\ 0 < z < 8]$ with the flux in the region $-1 < y < 1$ only. $\lambda f(A) = \lambda e^{-2A}$ for boundary function $\tilde{g}$. (a) $\lambda = 0$; (b) $\lambda = 1$; (c) $\lambda = 2$.

the same behaviour of the magnetic field in general was found, as can be seen in Figures 5.13 and 5.14.

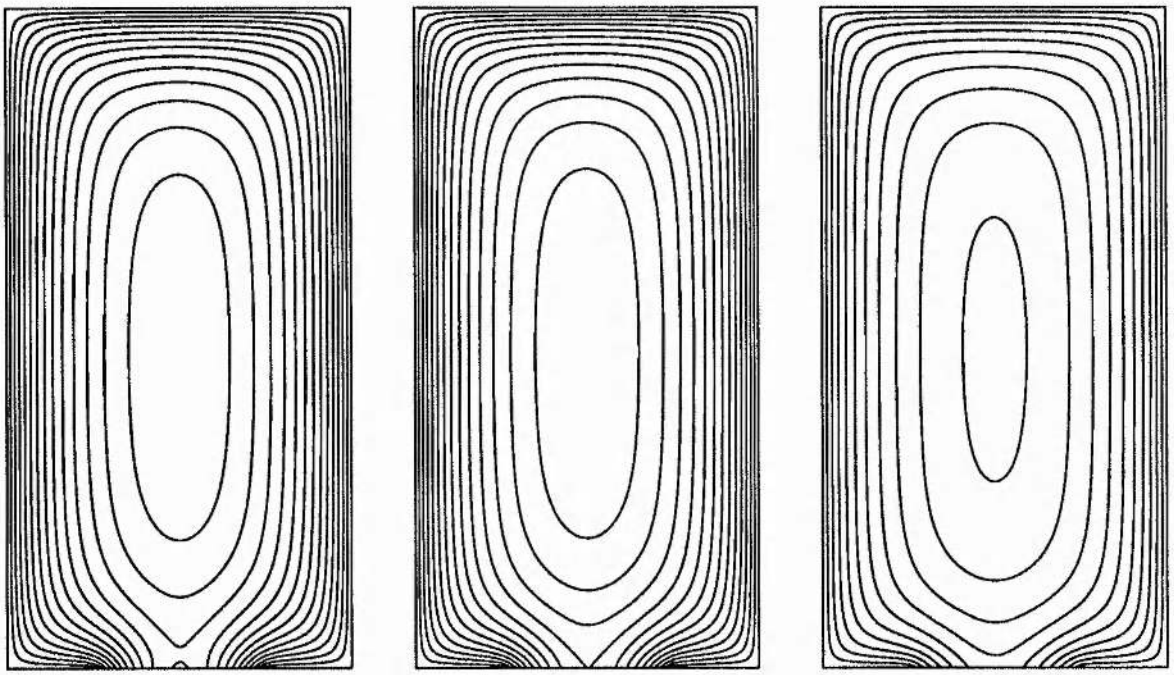

Figure 5.14: The magnetic field line structure for a big box $[-2 < y < 2,\ 0 < z < 8]$ with the flux in the region $-1 < y < 1$ only. $\lambda f(A) = \lambda e^{-2A}$ for boundary function $\tilde{g}$. (a) $\lambda = 5$; (b) $\lambda = 7$; (c) $\lambda = 10$.

Figure 5.13a shows the potential solution (i.e. $\lambda = 0$). As of course expected, the magnetic field is bulging sideways. Figures 5.13b and c shows the magnetic field lines for a some amount of current (i.e. $\lambda = 1$ and 2). In general the same general behaviour as discussed earlier in subsection 5.5.3 is found. An X-type neutral point can be found (Figure 5.13c), but again only in a certain current range. After the current exceeds a certain limit, only an O-type neutral point has formed (Figure 5.14).

The current value, when an X-type neutral point forms, is lower as for the smaller box; also the range, in which both neutral points are present, is broader for

the bigger box. However, the magnetic field can now expand more freely. We can also see that this magnetic configuration is very similar to the one in the tighter box for boundary function g (5.15); which is no wonder, since the magnetic field lines can now bend over at the sides, hence producing the lateral pinch we have already encountered for boundary function g (5.15) earlier on. This special configurations favours the existence of an X-type neutral point; nevertheless, beyond a certain current limit the X-type neutral point ceases to exist. Figure 5.15 shows the corresponding behaviour of the flux function A for the magnetic field shown in Figures 5.13 and 5.14.

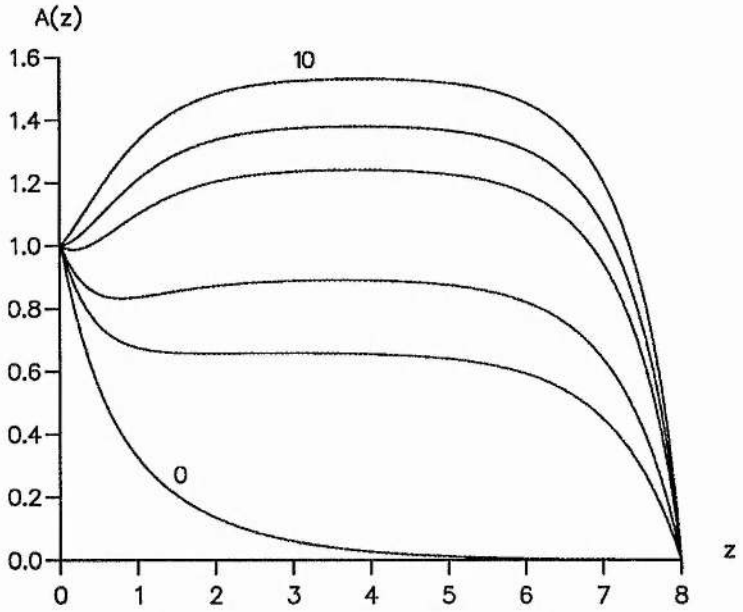

Figure 5.15: $A(z)$ at $y = 0$ for a big box $[-2 < y < 2,\ 0 < z < 8]$ with the flux in the region $-1 < y < 1$ only. $\lambda f(A) = \lambda e^{-2A}$ for boundary function $\tilde{g}$. $\lambda = 0, 1, 2, 5, 7, 10$.

In general the magnetic field shows the same behaviour as discussed beforehand for the tighter box. So we can be assured that the solutions are not influenced by the numerical box used.

5.7 Discussion

Three different types of axial current distributions have been investigated to see if they would create a magnetic field structure necessary for an inverse polarity prominence to form. The polynomials (5.18) and the trigonometric functions (5.19) have to be adjusted by an appropriate choice of constants; namely the maximum value of the flux function has to be much lower than the value which makes the axial current zero. The exponential function (5.20) is independent of such restrictions and proved to be the best choice for an axial current distribution to form a pre-prominence magnetic field for an inverse polarity prominence.

We look at these structures from a two-dimensional point of view, namely at a plane perpendicular to the prominence axis. Starting with a potential field ($\lambda = 0$), normal arcades are obtained. A small departure from the potential state ($\lambda = \tilde{\lambda} \neq 0$) causes these arcades to form inverse polarity structures, with an O-type and an X-type neutral point. A substantial departure ($\lambda > \tilde{\lambda}$) however, or as more field lines have reconnected and the twist has increased, the X-type neutral point is now below the photosphere and the field has an inverse polarity configuration with an O-type neutral point alone. This structure is not very sensitive to changes of the current through the value of λ (as long as $\lambda > \tilde{\lambda}$), while the other inverse structure with an X-type neutral point only occurs for the very small range of $\tilde{\lambda}$-values.

Summarising the results we get, if the current becomes strong enough (or λ exceeds a certain value), closed loops with seemingly no intersection with the photosphere. Initially they have contact with the photosphere and develop slowly in time to form closed loops. However, we only see a two-dimensional plane perpendicular to the prominence axis. In a three-dimensional view we would see the connection of these helical field lines to the photosphere. In the evolution beforehand some shearing and converging of the foot points occurs, together with flux cancellation at the neutral line (Van Ballegooijen and Martens, 1989), so that two normal field line loops come nearly end-to-end together and reconnect, giving a long twisted field line. In time more and more twisted field lines are created. So what appears to be a closed loop in the two-dimensional plane is actually a long helical field line. However, it was

not the aim of this chapter to look at this evolution due to foot point motions, but to understand the types of magnetic arcade structures various current distributions will create and whether it is possible to obtain inverse polarity structures that are in equilibrium.

Chapter 6

Current Sheet Models in Twisted Flux Tubes

6.1 Introduction

Recently it has been proposed that a prominence can form inside a large twisted flux tube (Priest, Hood and Anzer, 1989; Van Ballegooijen and Martens, 1989). The prominence forms a cool thin current sheet like structure while the external field remains essentially unmodified. However, the matching of the internal prominence solution and the external force-free solution within a twisted flux tube has been only recently investigated by Cartledge and Hood (1993). A detailed matching of the flux tube to the untwisted coronal field has yet only been demonstrated for a simplified case by Low (1993). An investigation of more complicated sheet currents (representing the prominence) and their matching to an external coronal field, as well as the resulting prominence properties, are the subject of this chapter.

Force-free field solutions, in Cartesian coordinates, invariant in a given direction, are presented to show the possibility of an inverse polarity prominence embedded in a large twisted flux tube. These new solutions are mathematically interesting and allow an investigation of different profiles of the current intensity of the magnetic field vector and of the mass density in the sheet.

6.2 The Background Field

The prominence lies in a twisted flux tube surrounded by a potential field. The potential field is assumed to be unsheared but, as discussed later, this can be removed without altering the basic results. Both the twisted flux tube and the untwisted field is considered in a self consistent model. Complex variable theory is used to describe the potential part of the field and the prominence will be represented by a branch cut in the complex plane. This technique will allow an investigation of different mass distributions within the prominence by specifying different current distributions.

The simplest model for a magnetic field in equilibrium in a low-β plasma is the force-free field of magnetohydrostatics, where the current is parallel to the magnetic field so that

$$\nabla \times \mathbf{B} = \alpha \mathbf{B}. \tag{6.1}$$

Using Maxwell's solenoidal equation, $\nabla \cdot \mathbf{B} = 0$, α satisfies

$$(\mathbf{B} \cdot \nabla)\, \alpha = 0. \tag{6.2}$$

z is taken as the direction along the prominence which overlies a long, relatively straight polarity inversion line; we may therefore neglect variations in this direction. The magnetic field can now be expressed by the *Grad-Shafranov* equation of Magnetohydrostatics

$$\nabla^2 A + \frac{1}{2}\frac{d}{dA} B_z^2(A) = 0, \tag{6.3}$$

where

$$\mathbf{B} = \left(\frac{\partial A(x,y)}{\partial y}, -\frac{\partial A(x,y)}{\partial x}, B_z(A) \right) \tag{6.4}$$

is given in terms of the scalar flux function $A(x,y)$. $B_z(A)$ is the z-component of the magnetic field and because of equations (6.1) and (6.2) is a function of A only. α can be written as

$$\alpha = \frac{dB_z(A)}{dA}. \tag{6.5}$$

In general, B_z is a nonlinear function of A and the Grad-Shafranov equation (6.3) becomes a non-linear, partial differential equation.

Let us consider the case of constant axial current (Low, 1993; Cartledge and Hood, 1993; Ridgway, Priest and Amari, 1991) for which

$$B_z(A) = \lambda A^{1/2}, \tag{6.6}$$

and λ is a constant. Equation (6.3) takes the linear form

$$\nabla^2 A + \frac{1}{2}\lambda^2 = 0 \tag{6.7}$$

with the general solution

$$A = \frac{1}{8}\lambda^2(r_0^2 - r^2) + A_{pot}, \tag{6.8}$$

where $r^2 = x^2 + y^2$, r_0 is a constant that is essentially the radius within which the constant axial current flows, i.e. the radius of the twisted flux tube. A_{pot} is the flux function for a potential field that satisfies

$$\nabla^2 A_{pot} = 0. \tag{6.9}$$

The general solution for equation (6.8) gives a magnetic field which does not decrease as $r \to \infty$. In order to obtain a globally well-behaved solution it is necessary to confine this solution to a finite domain and match it at the boundary to a potential solution, which is well behaved at infinity. The general solution (6.8) to equation (6.7) is also arbitrary up to a superposition of a potential function A_{pot}. We can therefore write (Low, 1993)

$$A = \begin{cases} \frac{1}{8}\lambda^2(r_0^2 - r^2) + A_{pot} & r \leq r_0 \\ \frac{1}{8}\lambda^2 r_0^2 \ln\left(\frac{r_0^2}{r^2}\right) + A_{pot} & r > r_0 \end{cases} \tag{6.10}$$

and

$$B_z = \begin{cases} \lambda A^{1/2} & r \leq r_0 \\ 0 & r > r_0 \end{cases} \tag{6.11}$$

where A_{pot} is the same potential function in both regions.

This solution describes a cylindrical, force-free magnetic field located in $r \leq r_0$, surrounded by a potential field for $r > r_0$. The edge of the flux tube is defined by $A = 0$ at $r = r_0$. The external potential field, in this case, is unsheared as $B_z = 0$. However, it is possible to include a constant axial field, B_z= constant, in the external region by defining the edge of the flux tube by a non zero value of A. Again the edge of the flux tube must be circular.

6.3 The Current Sheets

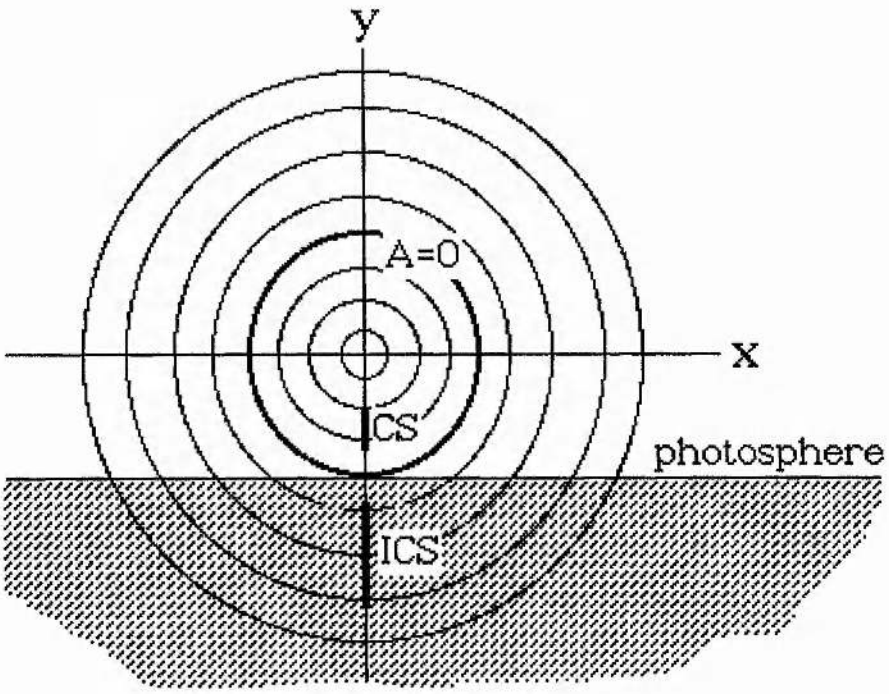

Figure 6.1: x, y-plane of the coordinate system used in this chapter. The potential magnetic field A_{pot} is generated by the current sheet (CS), extending in the z-direction and representing the prominence, combined with an image current sheet (ICS) below the photosphere, representing the line-tying effect. Variations in the z-direction are neglected. The magnetic field line $A = 0$ is indicated.

Quiescent prominences are found to lie above the magnetic polarity inversion line between two large-scale areas of opposing photospheric magnetic field polarities (Babcock and Babcock, 1955), often in the form of vertical sheet like structures. The simplest model for a prominence treats it as a cold discrete mass sheet of zero thickness, whose weight is balanced by an upward directed Lorentz-force. Thus, the mass density m_ρ of the current sheet can be expressed as (Anzer, 1989)

$$m_\rho = \frac{[B_y]B_x}{\mu g}, \tag{6.12}$$

where $[B_y] = B_y(0^+, y) - B_y(0^-, y)$ is the jump in B_y across the prominence from $x = 0^+$ to $x = 0^-$ and is related to the axial current flowing in the prominence. μ is the magnetic permeability and g is the gravitational acceleration.

The solution given by (6.10) is considered to be valid over the entire $x - y$ plane, where the potential field A_{pot} describes the discrete current sheet in the region $r < r_0$. The magnetic field given by the first terms on the right side of equations (6.10) and (6.11) is the force-free constant current background field. Projected onto the $x - y$ plane it is composed of concentric, circular field lines centered at $r = 0$. We seek to insert a massive, vertical electric current sheet in the region $r < r_0$. Gravity acts in the $-y$ direction; therefore it is assumed that the sheet consists of cold plasma that collects at the lowest points of the circular field lines of the background field. Following Low (1993), let the current sheet extend along the y-axis from $y = -b_1$ to $y = -b_2$, where $r_0 > b_2 > b_1 > 0$, to ensure that the current sheet lies in the region $r < r_0$ (see Figure 6.1). The desired potential A_{pot} then describes a potential magnetic field generated by this sheet with some current distributed on the sheet, flowing in the z-direction, combined with an image current sheet in $r > r_0$. This image current can be obtained by a geometric inversion of the former and extends therefore along the y-axis from $y = -r_0^2/b_2$ to $y = -r_0^2/b_1$. The image current is needed to maintain the circular shape of the field line at $r = r_0$. For a realistic coronal model the image current will be later excluded from the physical domain by placing the photosphere at $y = -r_0$. For the solar problem the important boundary condition is the distribution of the normal magnetic field component at the photosphere. Here we consider the solution obtained and state that if the photospheric normal field component is the one derived then we have a valid solution. In other words, the solution must give rise to a sensible normal field distribution.

To describe the potential part of the field $\mathbf{B} = (B_x, B_y, 0)$ complex variable theory is used ($\omega = x + iy$, $i = \sqrt{-1}$) and the prominence will be represented by a branch cut in the complex plane. This is achieved most easily by selecting functions that have fractional powers. Normally odd half powers are a good choice. In all Figures of this and the next chapter lengths are in units of r_0, which is the radius of the twisted flux tube.

6.3.1 Power 1/2

One particular realisation of the two-sheet potential field was found by Low (1993), in which fractional powers, in this case 1/2, give rise to cuts in the complex plane that simulate the current sheet. Thus,

$$\begin{aligned} B = B_y + iB_x &= -\left[(\omega + ib_1)^{1/2} - (\omega + ib_2)^{1/2}\right]^2 \\ &\quad + \frac{ir_0^2}{\omega^3}\left[\sqrt{b_1}\,(\omega + \frac{ir_0^2}{b_1})^{1/2} - \sqrt{b_2}\,(\omega + \frac{ir_0^2}{b_2})^{1/2}\right]^2 \\ &\quad - \frac{(b_1 - b_2)^2}{4\omega}. \end{aligned} \tag{6.13}$$

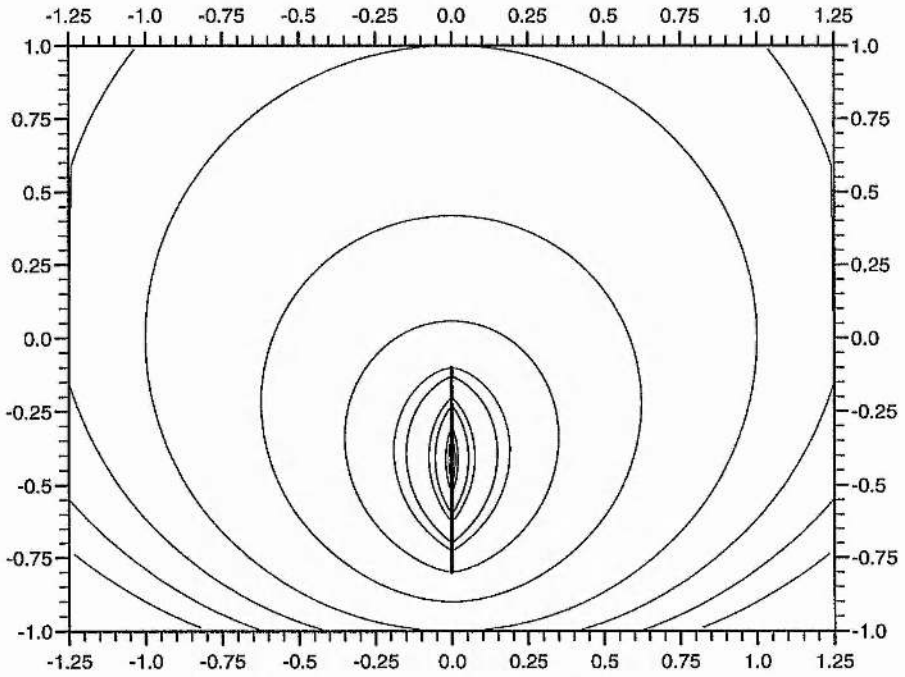

Figure 6.2: Power 1/2: Potential magnetic field for $b_1 = 0.1r_0$, $b_2 = 0.8r_0$, $r_0 = 1.0$.

The branch cuts associated with the four square roots of complex variables give rise to discontinuities in B_y, associated with the two finite length current sheets. Except at these current sheets the field associated with (6.13) is everywhere potential. These discontinuities are in the form of an abrupt reversal of the sign of B_y across the y-axis.

The above described field (6.13) is well-behaved as $r \to \infty$ and at $r = 0$. The first term on the right side of equation (6.13) describes the current sheet and has magnetic field components that tend to zero when $r \to \infty$. The second term on the right side of equation (6.13) describes the image current sheet and carries a singularity at $r = 0$, which is removed by the third term on the right side of equation (6.13). The image current sheet ensures that the field lines are circular at the edge of the flux tube and hence satisfies the requirement of continuity of magnetic pressure across this interface.

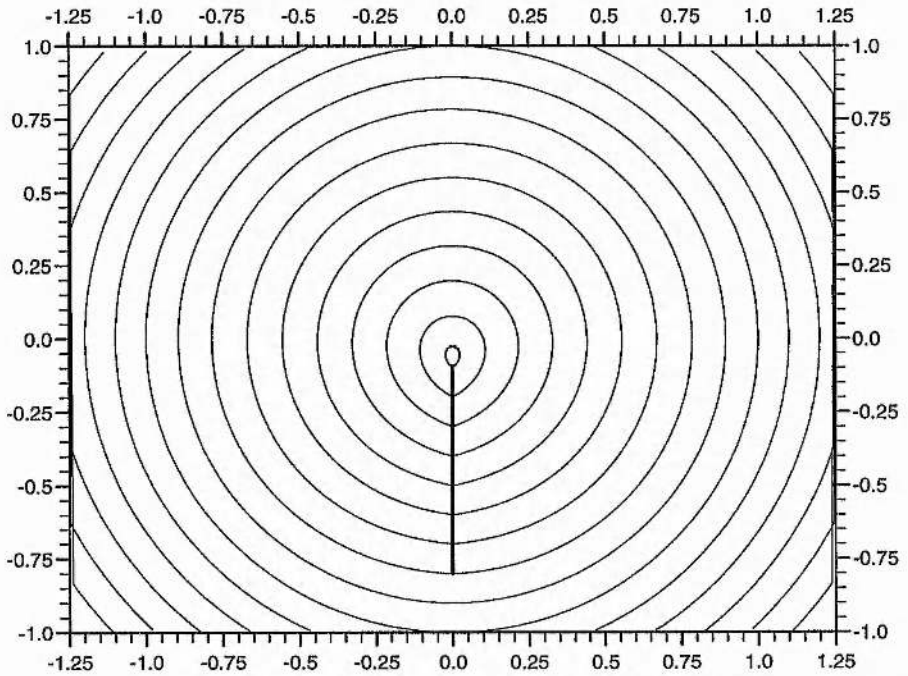

Figure 6.3: Power 1/2: Potential magnetic field and its linear superposition with the symmetric constant current force-free magnetic field for $b_1 = 0.1r_0$, $b_2 = 0.8r_0$, $r_0 = 1.0$, $\lambda = 5.1$.

The field lines in the neighbourhood of the upper sheet are shown in Figure 6.2. It shows that the Lorentz force is not everywhere upwards. Hence, a linear superposition of the above potential field with the constant current force-free background field is necessary to render the Lorentz force upwards everywhere along the current sheet. Thus, there is a minimum value for the parameter λ required for a meaningful

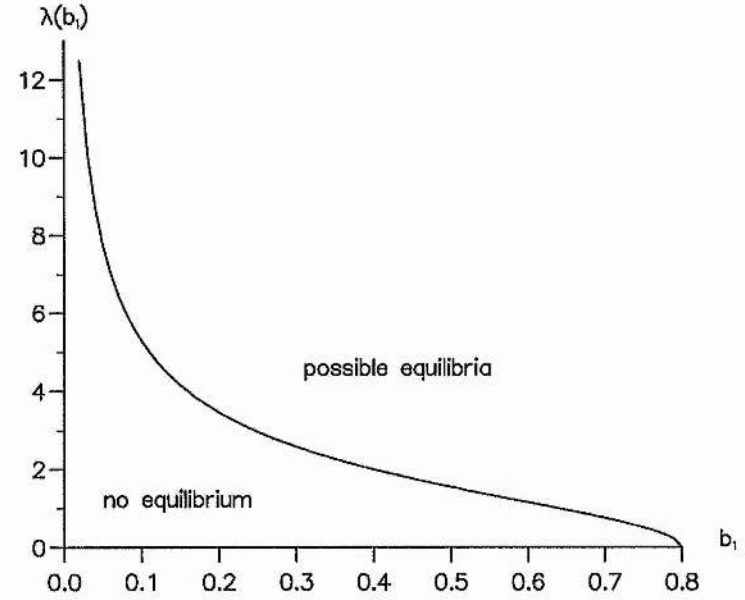

Figure 6.4: Power 1/2: The necessary λ-values, dependent on b_1, to make $B_x = 0$ at the top of the current sheet, for a fixed base $b_2 = 0.8r_0$.

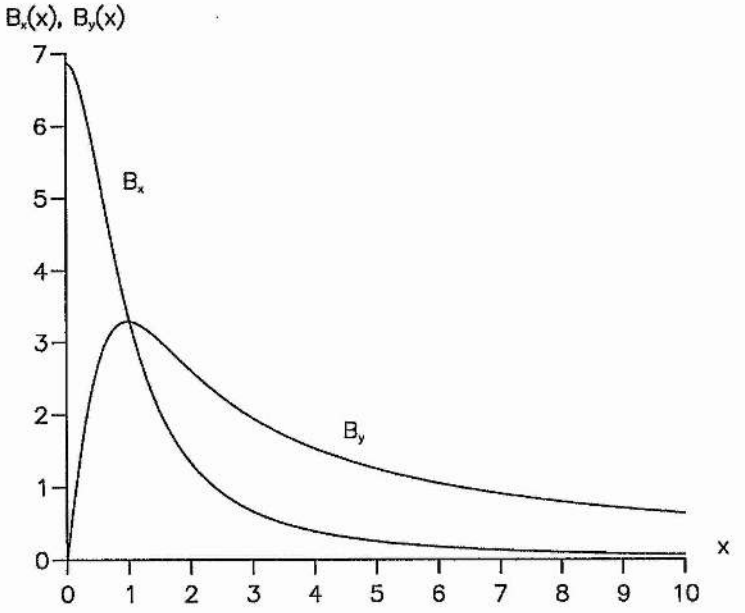

Figure 6.5: Power 1/2: $B_x(x)$ and $B_y(x)$ at the photosphere ($y = -r_0$) for $b_1 = 0.1r_0$, $b_2 = 0.8r_0$, $\lambda = 5.1$.

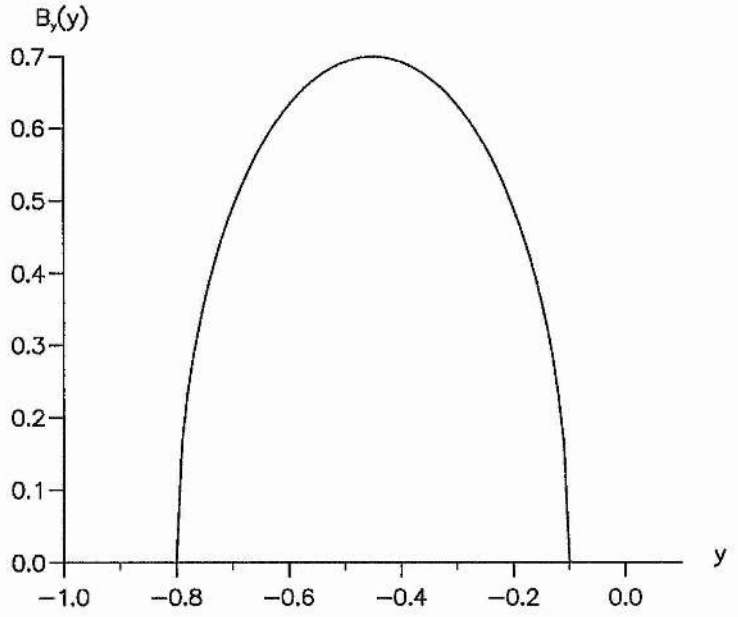

Figure 6.6: Power 1/2: $B_y(y)$ along the current sheet ($x = 0$) for $b_1 = 0.1r_0$, $b_2 = 0.8r_0$, $\lambda = 5.1$.

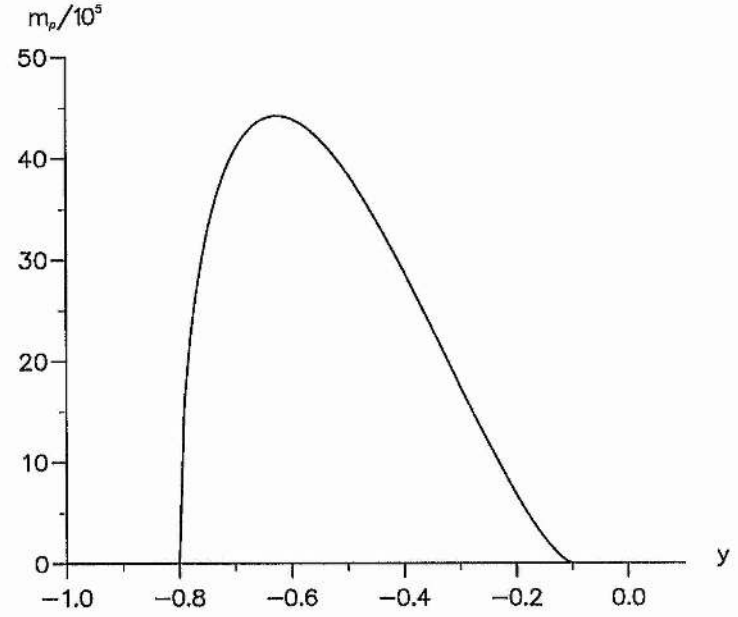

Figure 6.7: Power 1/2: Sheet mass density m_ρ along the current sheet ($x = 0$) for $b_1 = 0.1r_0$, $b_2 = 0.8r_0$, $\lambda = 5.1$.

prominence model. This configuration, as shown in Figure 6.3, is described by equation (6.10), taking A_{pot} to be the flux function of the potential field given by equation (6.13).

Figure 6.4 shows the minimum value of λ as a function of b_1 for a fixed base ($b_2 = 0.8r_0$). For λ-values lying above the curve an equilibrium can be obtained, since these values are large enough to ensure an upwardly directed Lorentz force everywhere on the upper current sheet. This occurs when B_x becomes positive at the top of the current sheet. Figure 6.5 shows the behaviour of the field components at large distances. As it can seen both components decrease with distance.

Figure 6.6 shows B_y and Figure 6.7 the sheet mass density m_ρ along the y-axis. Due to the power 1/2 used in equation (6.13), B_y and m_ρ show an abrupt change from zero at the end points of the current sheet. This is perhaps a little unrealistic and can be altered by adjusting the half powers in (6.13).

6.3.2 Power 3/2

In the twisted flux tube prominence model of Cartledge and Hood (1993) a nonsingular behaviour of the current was obtained by using higher powers in a radial expansion about the origin for the magnetic field. In addition, a power of 1/2 used in the above description of the magnetic field will give an infinite current density at the ends of the current sheets. Thus, we investigate potential magnetic fields A_{pot} described by higher powers.

An important requirement of the potential field is that it is circular at $r = r_0$, which allows us to match the flux tube model onto the external potential coronal field. Investigating (6.13) for power 1/2 we see, that the expressions in the two square brackets at $r = r_0$ are complex conjugates and so describes a circle as required.

For power 3/2 two different cases for the current sheets are possible.

Power 3/2, case A

As an example, consider

$$B = B_y + iB_x = \begin{array}{ll} +\frac{r_0^2}{\omega^2}\left[(\omega+ib_1)^{3/2}-(\omega+ib_2)^{3/2}\right]^2 & (I) \\ +\frac{i}{\omega^3}\left[b_1^{3/2}(\omega+\frac{ir_0^2}{b_1})^{3/2}-b_2^{3/2}(\omega+\frac{ir_0^2}{b_2})^{3/2}\right]^2. & (II) \end{array} \tag{6.14}$$

Firstly, investigate the behaviour of (6.14) as $r \to 0$. The second part of equation (6.14), labelled by (II), gives

$$\lim_{r\to 0} II = -\frac{9\,r_0^2\,(b_1-b_2)^2}{4\,\omega}. \qquad (III) \tag{6.15}$$

As was the case for power 1/2 this is a cylindrically symmetric term, and therefore the singularity in term II can easily be removed by subtracting term III from equation (6.14).

Unfortunately the first term on the right side of equation (6.14) also carries singularities, namely

$$\lim_{r\to 0} I = \begin{array}{ll} -\frac{ir_0^2}{\omega^2}(b_1^{3/2}-b_2^{3/2})^2 & (IV) \\ -\frac{3r_0^2}{\omega}(b_1^{3/2}-b_2^{3/2})(b_1^{1/2}-b_2^{1/2}) & (VI) \end{array}$$

Term VI is again cylindrically symmetric and can be removed by subtracting it from equation (6.14). We also subtract term IV from equation (6.14), but we have to be careful now because the $1/\omega^2$-dependence of this term disturbs our desired circular field line configuration at $r = r_0$. However, adding constant terms to potential solutions does not invalidate the general solution. Therefore we proceed by looking for a constant term which gives, together with term IV, a circle at $r = r_0$. The desired result is

$$-i\,(b_1^{3/2}-b_2^{3/2})^2 \qquad (V). \tag{6.16}$$

Secondly, consider the behaviour of (6.14) as $r \to \infty$. Term I vanishes, but term II tends to a constant, namely

$$\lim_{r\to\infty} II = i\,(b_1^{3/2}-b_2^{3/2})^2. \qquad (VII) \tag{6.17}$$

As can easily be seen, term VII cancels with term V, so the magnetic field is also well behaved at infinity.

Our desired magnetic field now consists of six terms, namely

$$\begin{aligned} B = B_y + iB_x = \; & +\tfrac{r_0^2}{\omega^2}\left[(\omega+ib_1)^{3/2}-(\omega+ib_2)^{3/2}\right]^2 && (I)\\ & +\tfrac{i}{\omega^3}\left[b_1^{3/2}(\omega+\tfrac{ir_0^2}{b_1})^{3/2}-b_2^{3/2}(\omega+\tfrac{ir_0^2}{b_2})^{3/2}\right]^2 && (II)\\ & +\tfrac{9r_0^2(b_1-b_2)^2}{4\omega} && (III)\\ & +\tfrac{ir_0^2}{\omega^2}(b_1^{3/2}-b_2^{3/2})^2 && (IV)\\ & -i\,(b_1^{3/2}-b_2^{3/2})^2 && (V)\\ & +\tfrac{3r_0^2}{\omega}(b_1^{3/2}-b_2^{3/2})(b_1^{1/2}-b_2^{1/2}), && (VI) \end{aligned} \tag{6.18}$$

where term I describes the current sheet from $-b_1$ to $-b_2$, term II the image current sheet from $-r_0^2/b_2$ to $-r_0^2/b_1$, term III removes the singularity in term II as $r \to 0$, terms IV and VI remove the singularities in term I as $r \to 0$, and term V is necessary to form a circular field line with term IV at $r = r_0$ and removes the homogeneous part of term II at infinity.

At the origin B is given by

$$B(x=0,y=0) = +\frac{9ir_0^2}{4}(b_1^{1/2}-b_2^{1/2})^2 - i\,(b_1^{3/2}-b_2^{3/2})^2. \tag{6.19}$$

The magnetic field lines for equation (6.18) are shown in Figure 6.8. They show a similar behaviour to the ones investigated by Low (1993) for power 1/2. (see Figure 6.2)

As can be seen again, the Lorentz force due to the current sheet is not everywhere upwards in the current sheet. The Lorentz force, being the repulsive force exerted by its image current of the opposite sign, is always upwards though. But the current in this sheet is everywhere of the same sign and different parts of it attract each other. At the top of the sheet, the mutual attraction between local current elements dominate over the repulsion force they all experience from the image current. The total Lorentz force is therefore downwards on the top part of the sheet. To avoid this self-pinching effect, the linear superposition of the above potential field with the constant current force-free background field was considered. The total magnetic field

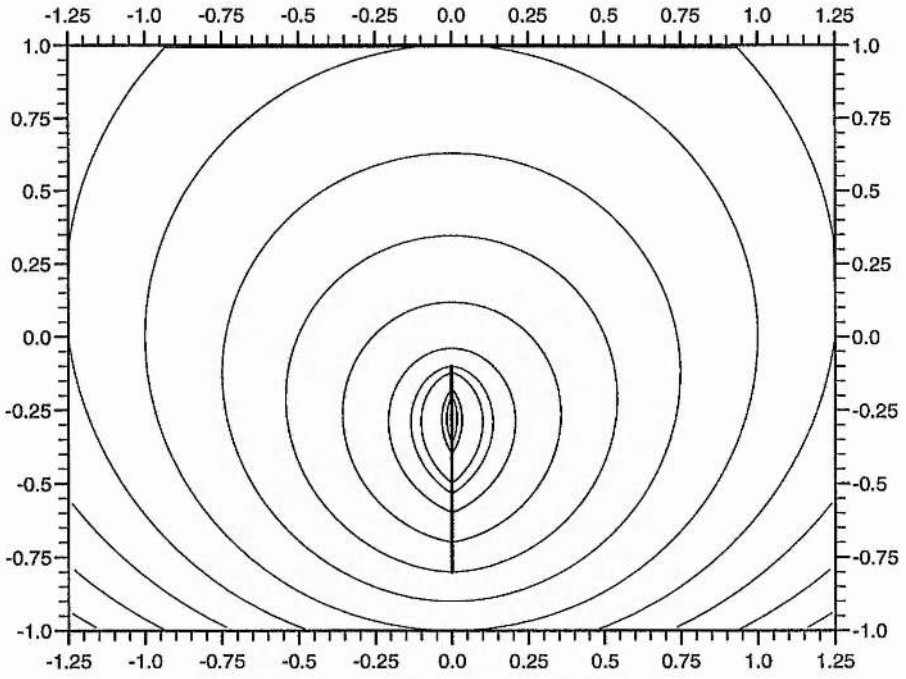

Figure 6.8: Power 3/2 case A: Potential magnetic field for $b_1 = 0.1r_0$, $b_2 = 0.8r_0$.

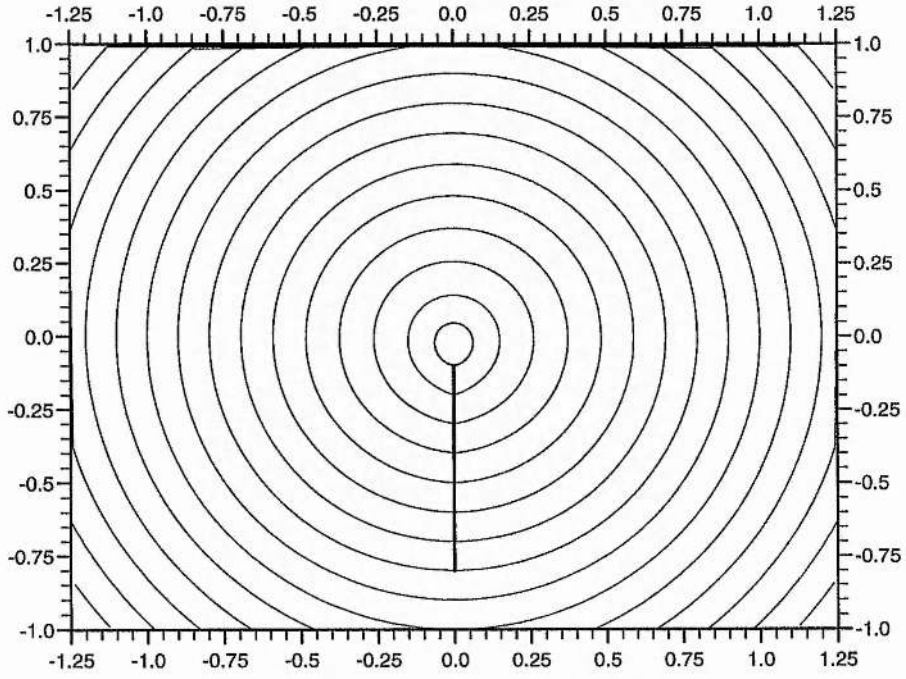

Figure 6.9: Power 3/2 case A: Potential magnetic field and its linear superposition with the symmetric constant current force-free magnetic field for $b_1 = 0.1r_0$, $b_2 = 0.8r_0$, $\lambda = 7$.

is potential in $r > r_0$, and non-potential in $r \leq r_0$ with currents in two forms, one the current sheet in the y-axis, and the other a current density aligned with the total magnetic field. Since the current sheet is not aligned with the total magnetic field, this gives rise to a vertical Lorentz force, as a result of the interactions between the current sheet with its image current sheet and the force-free currents. If the latter is of the proper sign, the total Lorentz force is upwards everywhere along the current sheet as required for a meaningful prominence model.

A vertically upwards Lorentz force is only possible when the force-free currents are present (independently derived by Lepeltier and Aly (1994), and Low and Hundhausen (1994)).

Note that the background constant current field has to have a certain magnitude before a prominence can form and this implies that the flux tube is twisted with the longitudinal field component an essential ingredient of the prominence.

Figure 6.9 shows such an example of a prominence model with an upward magnetic tension force everywhere on the sheet. The minimum λ has now to be greater than 7 whereas $\lambda > 5.1$ for power 1/2. The line $y = -r_0$ has been taken to be the photosphere.

Figure 6.10 shows the behaviour of B_y and Figure 6.11 shows the behaviour of m_ρ along the current sheet. As expected, the curves are much smoother now at the ends of the current sheet. $B_y(y)$ along the current sheet ($x = 0$) is independent of λ, since it is described by the real part of B, whereas λ at $x = 0$ contributes only to the imaginary part.

Power 3/2, case B

Another possibility for power 3/2 is

$$B = B_y + iB_x = \begin{array}{ll} -\left[(\omega + ib_1)^{3/2} - (\omega + ib_2)^{3/2}\right]^2 & (\widetilde{I}) \\ -\frac{ir_0^2}{\omega^5}\left[b_1^{3/2}(\omega + \frac{ir_0^2}{b_1})^{3/2} - b_2^{3/2}(\omega + \frac{ir_0^2}{b_2})^{3/2}\right]^2. & (\widetilde{II}) \end{array} \tag{6.20}$$

This also describes a circular field line at $r = r_0$.

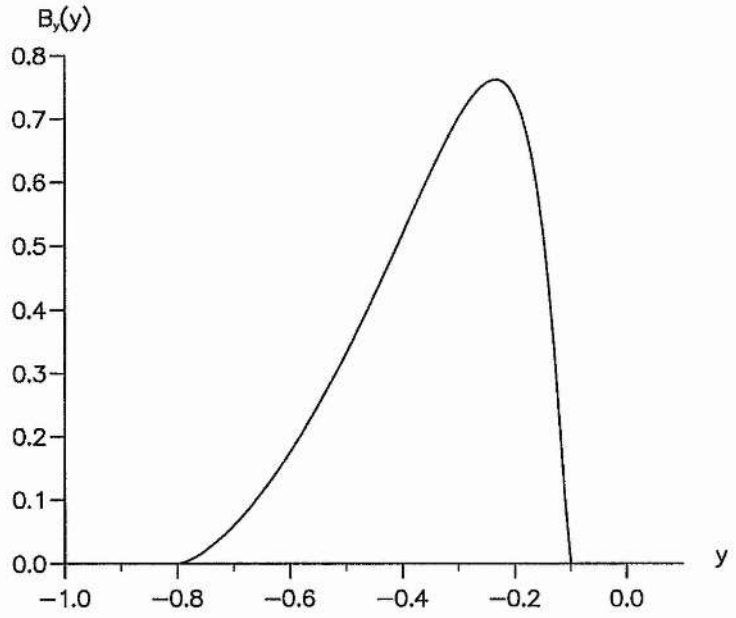

Figure 6.10: Power 3/2 case A: $B_y(y)$ along the current sheet ($x = 0$) for $b_1 = 0.1r_0$, $b_2 = 0.8r_0$, $\lambda = 7.0$.

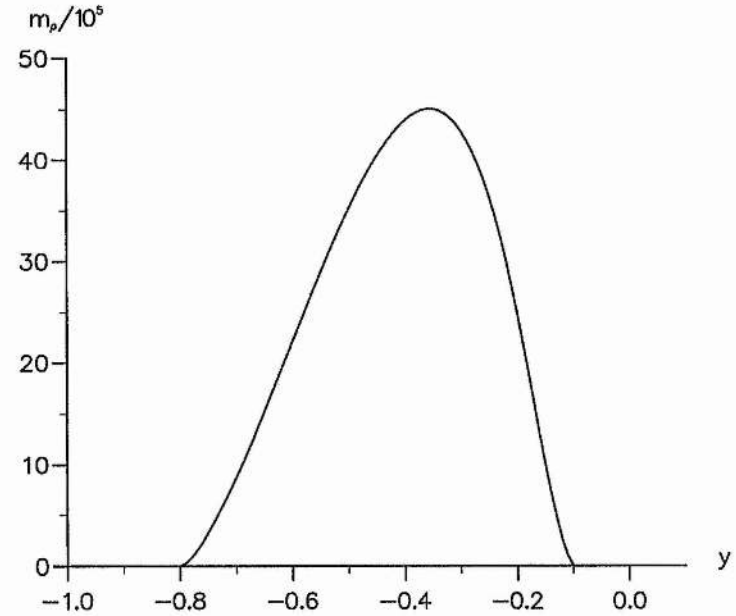

Figure 6.11: Power 3/2 case A: Sheet mass density m_ρ along the current sheet ($x = 0$) for $b_1 = 0.1r_0$, $b_2 = 0.8r_0$, $\lambda = 7.0$.

At infinity the first term on the right side of equation (6.20), $(\tilde{I})$, diverges.

$$\begin{aligned} \lim_{r\to\infty} \tilde{I} &= \frac{9}{4}(b_1-b_2)^2\,\omega && (\widetilde{IV}) \\ &+ \frac{9}{8}i(b_1-b_2)(b_1^2-b_2^2). && (\widetilde{VI}) \end{aligned} \tag{6.21}$$

At $r=0$ the second term on the right side of equation (6.20), $(\widetilde{II})$, carries singularities, namely

$$\begin{aligned} \lim_{r\to 0} \widetilde{II} &= +\frac{9}{4}\,\frac{r_0^4(b_1-b_2)^2}{\omega^3} && (\widetilde{III}) \\ &\quad -\frac{9}{8}\,\frac{ir_0^2(b_1-b_2)(b_1^2-b_2^2)}{\omega^2} && (\tilde{V}) \\ &\quad +\frac{3}{64}\,\frac{(b_1-b_2)^4}{\omega} && (\widetilde{VII}) \end{aligned} \tag{6.22}$$

These singularities can be removed by subtracting them from the magnetic field equation (6.20). Term $\widetilde{VII}$ is cylindrical symmetric. For the terms $\widetilde{III}$ and $\tilde{V}$ though we have to add other terms to make them circular at $r=r_0$. Luckily it turns out that these two extra terms $\widetilde{IV}$ and $\widetilde{VI}$ also remove the divergent terms at infinity (6.21).

This magnetic field configuration now becomes

$$\begin{aligned} B = B_y + iB_x = & -\left[(\omega+ib_1)^{3/2}-(\omega+ib_2)^{3/2}\right]^2 && (\tilde{I}) \\ & -\tfrac{ir_0^2}{\omega^5}\left[b_1^{3/2}(\omega+\tfrac{ir_0^2}{b_1})^{3/2}-b_2^{3/2}(\omega+\tfrac{ir_0^2}{b_2})^{3/2}\right]^2 && (\widetilde{II}) \\ & -\tfrac{9r_0^4}{4\omega^3}(b_1-b_2)^2 && (\widetilde{III}) \\ & -\tfrac{9}{4}(b_1-b_2)^2\,\omega && (\widetilde{IV}) \\ & +\tfrac{9}{8}\tfrac{ir_0^2}{\omega^2}(b_1-b_2)(b_1^2-b_2^2) && (\tilde{V}) \\ & -\tfrac{9}{8}i\,(b_1-b_2)(b_1^2-b_2^2) && (\widetilde{VI}) \\ & -\tfrac{3}{64\,\omega}(b_1-b_2)^4 && (\widetilde{VII}) \end{aligned} \tag{6.23}$$

where term $\tilde{I}$ describes the current sheet from $-b_1$ to $-b_2$, term $\widetilde{II}$ the image current sheet from $-r_0^2/b_2$ to $-r_0^2/b_1$, terms $\widetilde{III}$, $\tilde{V}$ and $\widetilde{VII}$ remove the singularities in term $\widetilde{II}$ as $r\to 0$, and terms $\widetilde{IV}$ and $\widetilde{VI}$ are necessary to form a circular field line with term $\widetilde{III}$ and term $\tilde{V}$, respectively, at $r=r_0$ and they also remove the divergent terms for term $\tilde{I}$ at infinity.

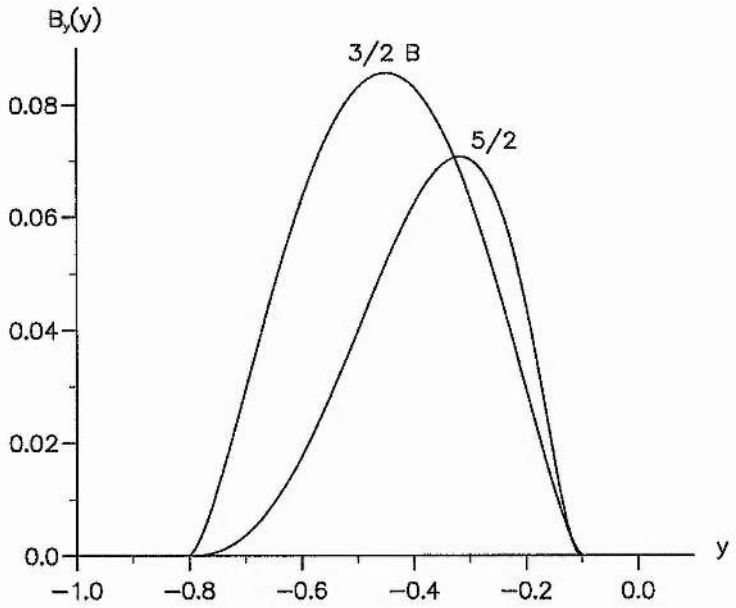

Figure 6.12: Power 3/2 case B and 5/2: $B_y(y)$ along the current sheet ($x = 0$). $b_1 = 0.1r_0$, $b_2 = 0.8r_0$, $\lambda = 1.5$.

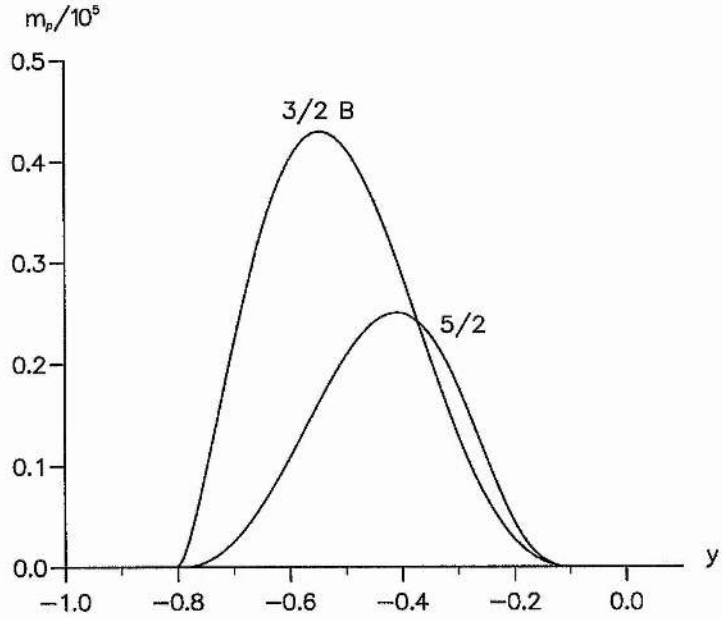

Figure 6.13: Power 3/2 case B and 5/2: Sheet mass density m_p along the current sheet ($x = 0$). $b_1 = 0.1r_0$, $b_2 = 0.8r_0$, $\lambda = 1.5$.

Again the field lines for (6.23) show a similar behaviour as for power 1/2 or power 3/2 case A. But now only $\lambda > 1.5$ is needed for the constant current background field (6.10) to ensure an upwardly directed Lorentz force along the whole current sheet.

Figure 6.12 shows the B_y-component and Figure 6.13 the sheet mass density m_ρ along the current sheet. They do not vary much in shape compared to the ones for power 3/2 case A (figures 6.10 and 6.11), but they are much smaller in size. A larger value of λ would increase m_ρ, but decrease the field line dip angle φ (see section 6.4.1).

6.3.3 Power 5/2

We write B as

$$
\begin{aligned}
B = B_y + iB_x = \; & + \tfrac{r_0^2}{\omega^2}\left[(\omega + ib_1)^{5/2} - (\omega + ib_2)^{5/2}\right]^2 && (\widehat{I}) \\
& - \tfrac{i}{\omega^5}\left[b_1^{5/2}(\omega + \tfrac{ir_0^2}{b_1})^{5/2} - b_2^{5/2}(\omega + \tfrac{ir_0^2}{b_2})^{5/2}\right]^2 && (\widehat{II}) \\
& + \tfrac{25 r_0^6}{4\omega^3}(b_1 - b_2)^2 && (\widehat{III}) \\
& + \tfrac{25}{4} r_0^2 (b_1 - b_2)^2 \omega && (\widehat{IV}) \\
& - \tfrac{75 i r_0^4}{8\omega^2}(b_1 - b_2)(b_1^2 - b_2^2) && (\widehat{V}) \\
& + \tfrac{75}{8} i r_0^2 (b_1 - b_2)(b_1^2 - b_2^2) && (\widehat{VI}) \\
& - \tfrac{225 r_0^2}{64\omega}(b_1^2 - b_2^2)^2 - \tfrac{75 r_0^2}{48\omega}(b_1 - b_2)(b_1^3 - b_2^3) && (\widehat{VII}) \\
& - \tfrac{i r_0^2}{\omega^2}(b_1^{5/2} - b_2^{5/2})^2 && (\widehat{VIII}) \\
& + i(b_1^{5/2} - b_2^{5/2})^2 && (\widehat{IX}) \\
& - \tfrac{5 r_0^2}{\omega}(b_1^{5/2} - b_2^{5/2})(b_1^{3/2} - b_2^{3/2}) && (\widehat{X})
\end{aligned}
\tag{6.24}
$$

Again term $\widehat{I}$ describes the current sheet from $-b_1$ to $-b_2$ and term $\widehat{II}$ the image current sheet from $-r_0^2/b_2$ to $-r_0^2/b_1$. Terms $\widehat{III}$, $\widehat{V}$ and $\widehat{VII}$ remove the singularities in term $\widehat{II}$ as $r \to 0$, and terms $\widehat{IV}$ and $\widehat{VI}$ are necessary to form a circular field line with term $\widehat{III}$ and term $\widehat{V}$, respectively, at $r = r_0$ and they also remove the divergent terms for term $\widehat{I}$ at infinity.

Terms $\widehat{VIII}$ and $\widehat{X}$ remove the singularities in term $\widehat{I}$ as $r \to 0$, while term $\widehat{IX}$ is necessary to form a circular field line with term $\widehat{VIII}$ at $r = r_0$ and removes the homogeneous part for term $\widehat{II}$ at infinity.

Again we find a similar field line configuration as for lower powers. As for power 3/2 case B, we only need a $\lambda > 1.5$ to render the Lorentz force properly.

Figures 6.12 and 6.13 also show the B_y-component and the sheet mass density m_ρ along the current sheet for power 5/2. The curves are much smoother now on both ends of the current sheet. While the B_y-component is independent of λ, m_ρ can be increased by using a higher λ.

It is clear that higher powers can be selected but the number of terms needed to keep the radius r_0 circular and the field well behaved will increase.

6.3.4 Mixed Powers

The distribution of current and mass along the sheet depends on the choice of powers. Other possibilities exist which are discussed in this section.

Different Powers for the Current and the Image Current Sheet

Let us consider the first part of B, describing the current sheet, is of power 1/2 and the second part of B, describing the image current sheet, of power 3/2, as for example

$$\begin{aligned} B &= k_1 \left[(\omega + ib_1)^{1/2} - (\omega + ib_2)^{1/2}\right]^2 \\ &\quad + k_2 \left[\sqrt{b_1^3}\,(\omega + \frac{ir_0^2}{b_1})^{3/2} - \sqrt{b_2^3}\,(\omega + \frac{ir_0^2}{b_2})^{3/2}\right]^2 . \end{aligned} \tag{6.25}$$

Since the second part of (6.25) is now of higher power than the first one, we rewrite B as

$$\begin{aligned} B &= k_1 \left[(\omega + ib_1)^{1/2} - (\omega + ib_2)^{1/2}\right]^2 + k_2\,(ir_0^2)^2 \left[\left(1 + \frac{b_1\omega}{ir_0^2}\right)\right. \\ &\quad \left.\sqrt{b_1}\left(\omega + \frac{ir_0^2}{b_1}\right)^{1/2} - \left(1 + \frac{b_2\omega}{ir_0^2}\right)\sqrt{b_2}\left(\omega + \frac{ir_0^2}{b_2}\right)^{1/2}\right]^2 . \end{aligned} \tag{6.26}$$

The first aim is to get a circular field line at $r = r_0$. Setting $\omega = r_0 e^{i\vartheta}$, B transforms to

$$B = k_1 i \left[\sqrt{b_1}\left(1 - \frac{ir_0 e^{i\vartheta}}{b_1}\right)^{1/2} - \sqrt{b_2}\left(1 - \frac{ir_0 e^{i\vartheta}}{b_2}\right)^{1/2}\right]^2$$

$$- k_2 r_0^5 e^{i\vartheta} \left[\left(1 - \frac{ib_1 e^{i\vartheta}}{r_0}\right) \sqrt{b_1} \left(1 + \frac{ir_0 e^{-i\vartheta}}{b_1}\right)^{1/2} - \left(1 - \frac{ib_2 e^{i\vartheta}}{r_0}\right) \sqrt{b_2} \left(1 + \frac{ir_0 e^{-i\vartheta}}{b_2}\right)^{1/2} \right]^2 . \tag{6.27}$$

The terms under the square roots of the first part of (6.27) are the conjugate complex terms of the terms under the square roots of the second part of (6.27). To make everything in the square brackets conjugate complex, we have to multiply into the first part the conjugate complex of $(1 - ib_1 e^{i\vartheta}/r_0) := c_1$ and $(1 - ib_2 e^{i\vartheta}/r_0) := c_2$, respectively. But

$$c_1^* = 1 + \frac{ib_1 e^{-i\vartheta}}{r_0} = 1 + \frac{ib_1}{r_0 e^{i\vartheta}} = 1 + \frac{ib_1}{\omega}$$

or

$$c_1^* \omega = (\omega + ib_1) \qquad \text{and} \qquad c_2^* \omega = (\omega + ib_2). \tag{6.28}$$

Multiplying the first part on the right side of (6.27) by (6.28) brings it to power 3/2. Different powers for the current and the image current sheet are therefore not possible.

Different Powers in the Current Sheets

Let us now consider the case where different powers, here 1/2 and 3/2, are used to describe the current sheet, and image current sheet, respectively. (This we refer to as mp1/3, standing for mixed powers 1/2 and 3/2.)

We write B as

$$\begin{aligned} B = B_y + iB_x = \; & - \tfrac{r_0^2}{\omega^2} \left[i\,(\omega + ib_1)^{1/2} - (\omega + ib_2)^{3/2} \right]^2 && \text{(i)} \\ & - \tfrac{i}{\omega^3} \left[\omega\, b_1^{1/2} (\omega + \tfrac{ir_0^2}{b_1})^{1/2} - b_2^{3/2} (\omega + \tfrac{ir_0^2}{b_2})^{3/2} \right]^2 && \text{(ii)} \\ & + \tfrac{r_0^6}{\omega^3} && \text{(iii)} \\ & + r_0^2 \omega && \text{(iv)} \\ & + \tfrac{2ir_0^4}{\omega^2} (1 - \tfrac{3}{2} b_2) && \text{(v)} \end{aligned} \tag{6.29}$$

$$
\begin{aligned}
= \; & -2ir_0^2\,(1-\tfrac{3}{2}b_2) && \text{(vi)}\\
& -\tfrac{r_0^2}{\omega}(3b_2(b_2-1)-(b_1-1)) && \text{(vii)}\\
& -\tfrac{ir_0^2}{\omega^2}(b_1^{1/2}-b_2^{3/2})^2 && \text{(viii)}\\
& +i(b_1^{1/2}-b_2^{3/2})^2 && \text{(ix)}\\
& -\tfrac{r_0^2}{\omega}(b_1^{1/2}-b_2^{3/2})(b_1^{-1/2}-3b_2^{1/2}) && \text{(x)}
\end{aligned}
$$

The added terms (iii) to (x) in equation (6.29) are needed to remove singularities at zero and divergencies at infinity. The added i in term (i) and the added ω in term (ii) are necessary to keep the field line at $r = r_0$ circular.

Since for the potential magnetic field alone (6.29) the Lorentz force can not be directed upwards all along the current sheet, we have again to consider its linear superposition with the cylindrically symmetric constant-current force free field (6.10). For the case here the necessary λ has to be at least 28.

Another possibility is to switch the powers in the description of the current sheets, hence first power 3/2, then power 1/2. (This is referred to as mp3/1.) The description of the field is similar to (6.29). Again the added i in term ($\widetilde{\text{i}}$) and the added ω in term ($\widetilde{\text{ii}}$) are necessary to keep the field line at $r = r_0$ circular.

$$
\begin{aligned}
B = B_y + iB_x = \; & +\tfrac{r_0^2}{\omega^2}\left[(\omega+ib_1)^{3/2}-i\,(\omega+ib_2)^{1/2}\right]^2 && (\widetilde{\text{i}})\\
& +\tfrac{i}{\omega^3}\left[b_1^{3/2}(\omega+\tfrac{ir_0^2}{b_1})^{3/2}-\omega\,b_2^{1/2}(\omega+\tfrac{ir_0^2}{b_2})^{1/2}\right]^2 && (\widetilde{\text{ii}})\\
& -\tfrac{r_0^6}{\omega^3} && (\widetilde{\text{iii}})\\
& -r_0^2\,\omega && (\widetilde{\text{iv}})\\
& -\tfrac{2ir_0^4}{\omega^2}\,(1-\tfrac{3}{2}b_1) && (\widetilde{\text{v}})\\
& +2ir_0^2\,(1-\tfrac{3}{2}b_1) && (\widetilde{\text{vi}})\\
& +\tfrac{r_0^2}{\omega}(3b_1(b_1-1)-(b_2-1)) && (\widetilde{\text{vii}})\\
& +\tfrac{ir_0^2}{\omega^2}(b_1^{3/2}-b_2^{1/2})^2 && (\widetilde{\text{viii}})\\
& -i(b_1^{3/2}-b_2^{1/2})^2 && (\widetilde{\text{ix}})\\
& +\tfrac{r_0^2}{\omega}(b_1^{3/2}-b_2^{1/2})(3b_1^{1/2}-b_2^{-1/2}) && (\widetilde{\text{x}})
\end{aligned}
\qquad (6.30)
$$

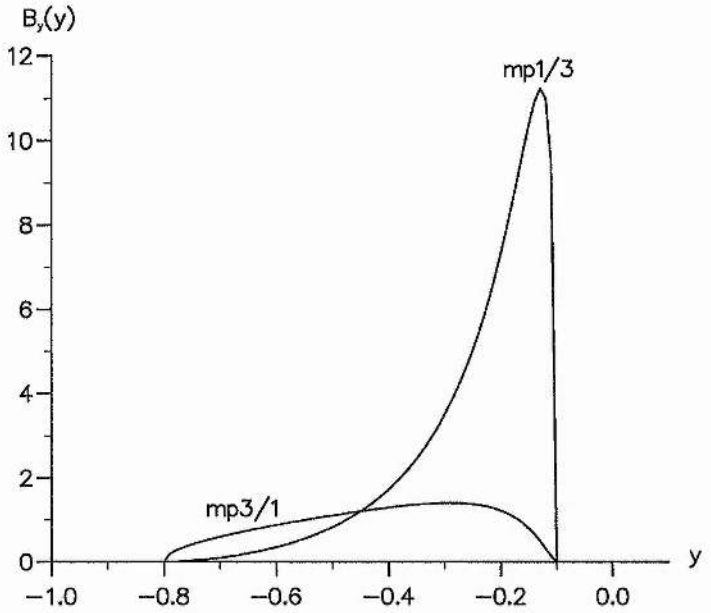

Figure 6.14: Both mixed powers: $B_y(y)$ along the current sheet ($x = 0$) for $b_1 = 0.1r_0$, $b_2 = 0.8r_0$, $\lambda = 28.0$.

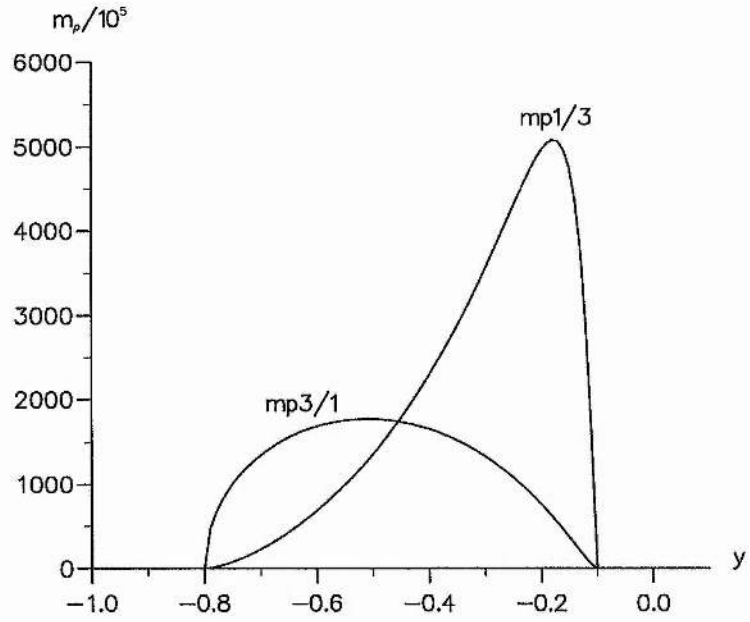

Figure 6.15: Both mixed powers: Sheet mass density m_ρ along the current sheet ($x = 0$) for $b_1 = 0.1r_0$, $b_2 = 0.8r_0$, $\lambda = 28.0$.

The minimum necessary λ of the constant current force-free field (6.10) has now to be only 10. For comparison with the mixed power mp1/3 we will use $\lambda = 28$ too.

Figure 6.14 shows the B_y-component and Figure 6.15 the sheet mass density m_ρ, both along the current sheet for both mixed powers mp1/3 and mp3/1 for $\lambda = 28$. Note the different shapes. For $\lambda = 10$ the maximum of m_ρ for mp3/1 would only be at approximately $235/10^5$. A larger value of λ increases the height of the sheet mass density curve, but does not change the shape. However, it does decrease the dip angle φ (see section 6.4.1).

6.4 Prominence Properties

Now let us investigate the predictions of the models of the previous section for various prominence properties.

6.4.1 Field line dip angle φ

The magnetic field enters the prominence at an angle φ to the horizontal. φ is defined by

$$\tan\varphi = \frac{B_y}{B_x}, \tag{6.31}$$

and is typically the order of 10°. Figures 6.16 and 6.17 shows the field line dip angle φ for all models. φ is in the range 5°-20° and is in agreement with observations (Leroy, 1987). Figure 6.17 also shows for the mixed power mp3/1 how a stronger background field (larger λ) than necessary flattens the field line dip. Therefore the tops of the curves for powers 3/2 case B and 5/2 for a $\lambda = 7$ would be around two degrees only.

6.4.2 Shear angle α

Observations (Tandberg-Hanssen and Anzer, 1970; Leroy, 1978; Nikolsky et al., 1984) have shown that the magnetic field passes through a prominence at an angle

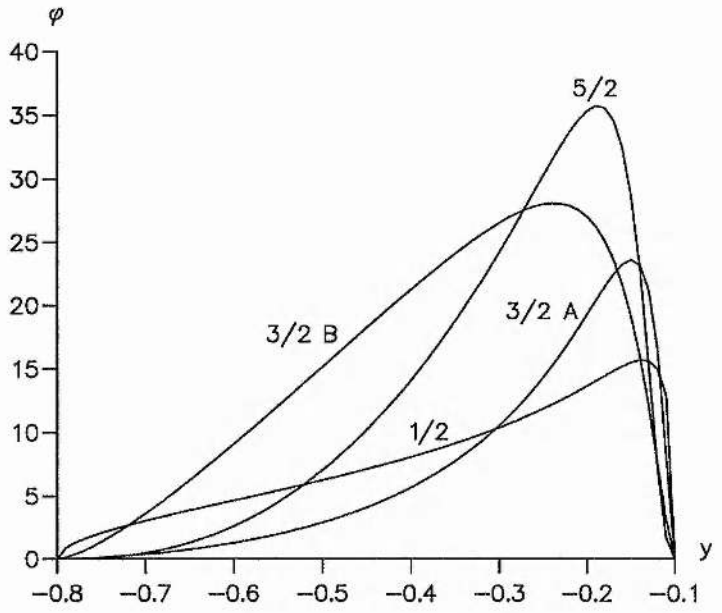

Figure 6.16: $\varphi = \arctan(B_y/B_x)$ along the current sheet ($x = 0$). Powers 1/2 and 3/2 case A for $\lambda = 7$; and powers 3/2 case B and 5/2 for $\lambda = 1.5$. $b_1 = 0.1r_0$, $b_2 = 0.8r_0$.

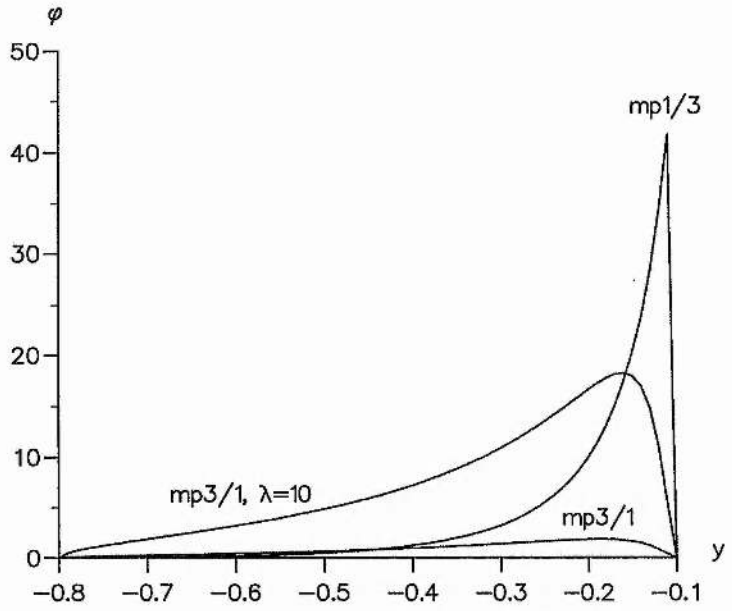

Figure 6.17: $\varphi = \arctan(B_y/B_x)$ along the current sheet ($x = 0$). Mixed powers mp1/3 and mp3/1 for $\lambda = 28$; and mp3/1 for $\lambda = 10$. $b_1 = 0.1r_0$, $b_2 = 0.8r_0$.

α to the prominence axis. α lies in the range 10°-30° and is given by

$$\tan\alpha = \frac{B_x}{B_z}. \tag{6.32}$$

Figure 6.18 shows, that for all current distributions the magnetic field is sheared and is within the range given by observations. The shear angle is only very weakly dependent on the range of λ-values used. This is because λ must exceed the minimum value needed for the correct sign of the Lorentz force, i.e. $B_x > 0$. Thus, in (6.10) the nonpotential part of A is larger than the A_{pot}-part. Hence, $\tan\alpha \simeq -y/\sqrt{2(1-y^2)}$ with the weak dependence on λ only influencing the region near the top of the current sheet. Therefore using different λs will not change the main behaviour of the graphs in Figure 6.18. It also shows that the shear decreases when approaching the top of the prominence as B_x is smaller there. Again the values are close to the observed values (Leroy, 1987).

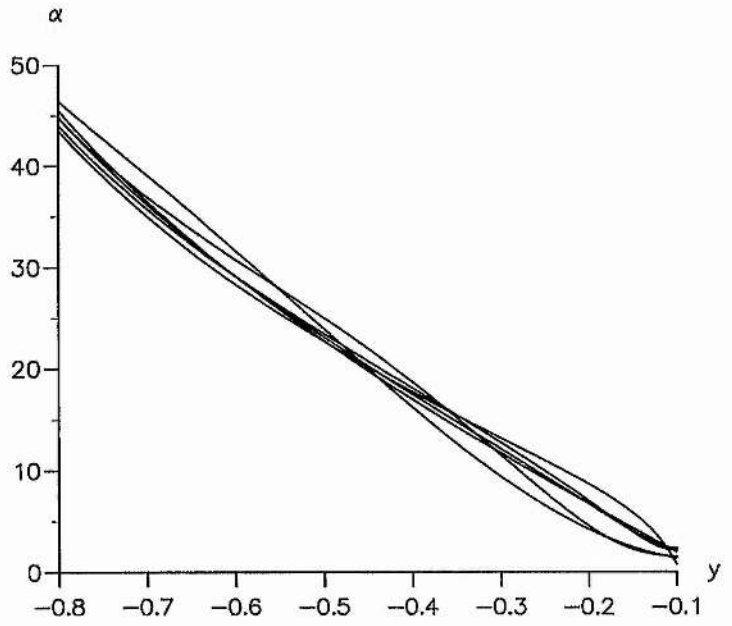

Figure 6.18: $\alpha = \arctan(B_x/B_z)$ along the current sheet ($x = 0$) for all powers (1/2, 3/2 case A and B, 5/2 ($\lambda = 7$) and both mixed powers ($\lambda = 28$)) with $b_1 = 0.1r_0$, $b_2 = 0.8r_0$.

6.4.3 Mass and densities

The sheet mass density m_ρ, whose different graphs we have already seen for the various powers, was given by equation (6.12). The total mass M of the prominence per unit length is then given by

$$M = r_0 \int_{-b_2}^{-b_1} m_\rho \, dy, \tag{6.33}$$

with r_0 being the height against which all heights are made dimensionless (approximately the height of a prominence).

The density can be obtained by dividing the sheet mass density m_ρ by a typical prominence width d (d = 5-10 Mm). Table 6.1 shows the number densities for the various models. For comparison a higher λ than necessary was also considered in some cases.

Table 6.1: The integral over the sheet mass density m_ρ, and the particle density n for the various current distributions.

λ	power	$\int_{-b_1}^{-b_2} m_\rho dy$	n [m^{-3}]	λ	power	$\int_{-b_1}^{-b_2} m_\rho dy$	n [m^{-3}]
5.1	1/2	$1.9 \cdot 10^{-3}$	10^{17}	1.5	5/2	$8 \cdot 10^{-6}$	10^{15}, 10^{14}
7	1/2	$3.5 \cdot 10^{-3}$	10^{18}, 10^{17}	7	5/2	$1.8 \cdot 10^{-4}$	10^{16}
7	3/2 A	$1.8 \cdot 10^{-3}$	10^{17}	28	mp 13	$1.5 \cdot 10^{-1}$	10^{19}
1.5	3/2 B	$1.5 \cdot 10^{-5}$	10^{15}, 10^{14}	10	mp 31	$1.2 \cdot 10^{-2}$	10^{18}
7	3/2 B	$3.2 \cdot 10^{-4}$	10^{17}, 10^{16}	28	mp 31	$8.9 \cdot 10^{-2}$	10^{19}

In general the obtained densities n are in the range of 10^{16} to 10^{17} m^{-3}, in agreement with observations. (Priest, 1988) The densities for the mixed powers are too high, due to the large λ necessary for a totally upwardly directed Lorentz force.

6.4.4 Magnetic field strength as a function of height

Quiescent prominences have been found to possess a slow increase of the magnetic field strength with altitude (Rust, 1967; Leroy, 1977; Leroy, 1989; Kim,

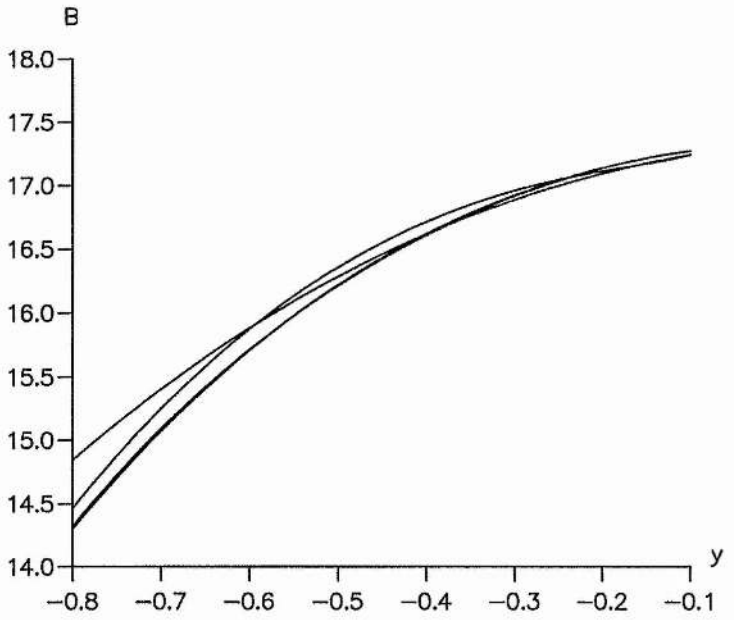

Figure 6.19: Magnetic field strength (in G) along the current sheet ($x = 0$, $b_1 = 0.1r_0$, $b_2 = 0.8r_0$) for powers 1/2, 3/2 case A and B and 5/2 for $\lambda = 7.0$.

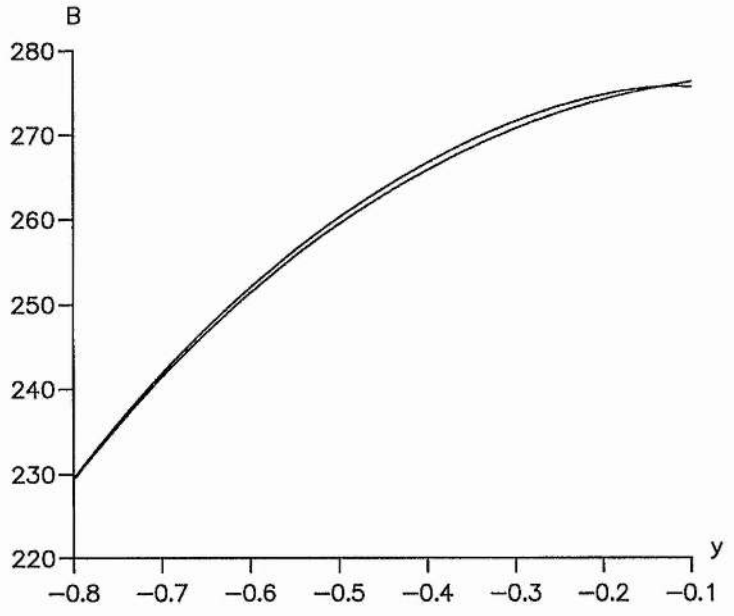

Figure 6.20: Magnetic field strength (in G) along the current sheet ($x = 0$, $b_1 = 0.1r_0$, $b_2 = 0.8r_0$) for both mixed powers mp1/3 and mp3/1 for $\lambda = 28.0$.

1990). All our models show a general increase in magnetic field strength with height (figure 6.19) in agreement with observations. Larger λ values, as used in Figure 6.20 for mixed powers, are responsible for the larger magnetic field strength at the prominence base. Also the range of the increase of the magnetic field strength increases if λ is larger. Using $\lambda = 1.5$ for powers 3/2 case B or 5/2 the magnetic field strength at the prominence base drops to approximately 0.7 and at the top of the prominence to approximately 0.8 G. Using $\lambda = 10$ for mixed power mp3/1 gives a magnetic field strength of 30 G at the base and of 35 G at the top of the prominence. However, there is always an increase of the magnetic field strength with height.

6.5 Comparison of the different Models

As we have seen all models show an increase in magnetic field strength with height and a shear, only weakly dependent on the strength of their background field through the choice of λ. We are limited in our choice of λ since there is a minimum value for which the Lorentz force is just positive all along the current sheet. This λ_{min} is different for the various models and depends on the values of b_1 and b_2. With $b_1 = -0.1r_0$ and $b_2 = -0.8r_0$, $\lambda_{min} = 5.1$ for power 1/2, and $\lambda_{min} = 7$ for power 3/2 case A. For both powers 3/2 case B and 5/2 $\lambda_{min} = 1.5$ only. For the mixed power mp1/3 λ_{min} is quite high, namely 28, whereas for mp3/1 $\lambda_{min} = 10$. We can choose a larger λ than λ_{min}, but have to be aware that this will decrease our field line dip angle. On the other hand it will increase the density.

In Figure 6.21 we see the B_y-component (which is independent of λ) and in Figure 6.22 the sheet mass density m_ρ (which is dependent on λ) for powers 1/2, 3/2 case A and B, and 5/2. λ-values, which will give realistic densities (see table 6.1), have been chosen.

The prominence model of Low (1993), using power 1/2 in its description, has abrupt endings of its mass distribution at the ends of the current sheet. In addition, it will have an infinite current density at these ends. This has been removed here by using higher powers in the description of the current distribution.

In Figure 6.22 the value $\lambda = 7$ has been used for powers 3/2 case B and 5/2.

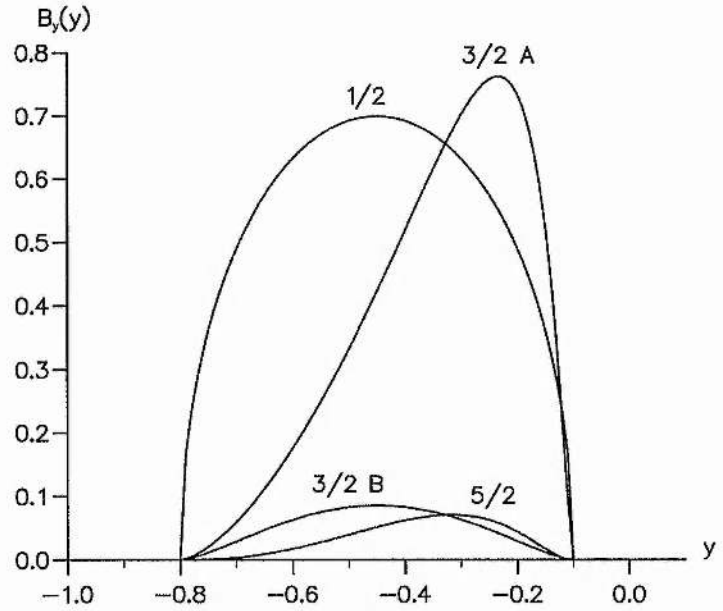

Figure 6.21: $B_y(y)$ for power 1/2 ($\lambda = 5.1$), and powers 3/2 case A and B, and 5/2 ($\lambda = 7$). $b_1 = 0.1r_0$, $b_2 = 0.8r_0$.

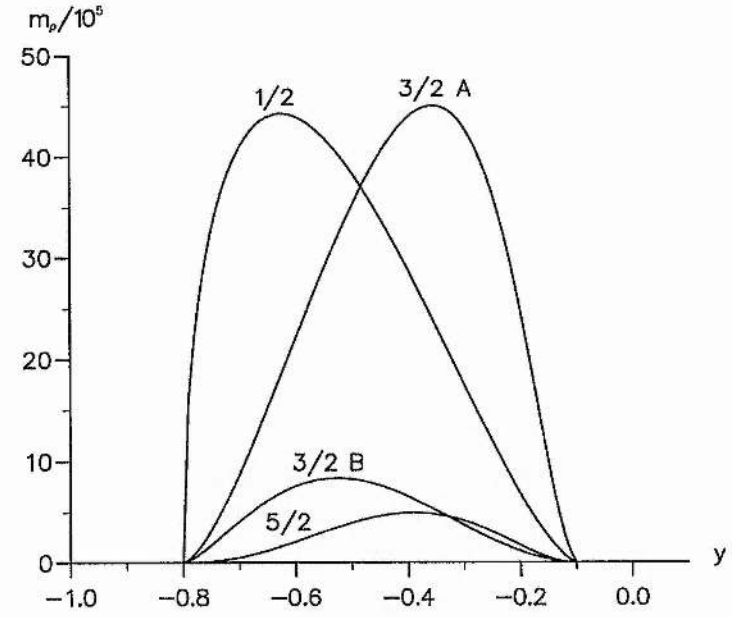

Figure 6.22: Sheet mass density m_ρ for power 1/2 ($\lambda = 5.1$), and powers 3/2 case A and B, and 5/2 ($\lambda = 7$). $b_1 = 0.1r_0$, $b_2 = 0.8r_0$.

This can be compared with the value $\lambda = 1.5$ used in Figure 6.13. As can be seen there, these graphs are much lower, producing too low a value for the density. Using $\lambda = 7$ in these descriptions will give us the required number density in the range 10^{16} to 10^{17}. The field line dip angle φ will be around 2°. If we decide to choose power 3/2 case A, we also get a realistic density, but with a much steeper field line dip angle.

The mixed powers mp1/3 and mp3/1 need quite a strong force-free background field to render the Lorentz force upwards along the whole current sheet. These large λ values have a direct effect on the sheet mass densities m_ρ; hence these current distributions produce densities which are too high when compared to observational values.

The current distributions using powers 3/2 and 5/2 are closest to observed values. For power 3/2 we can choose between a large or small field line dip angle (case A or B), due to the different necessary minimum constant-current force-free background fields.

6.6 Discussion

Observations in Hα suggest that a prominence is embedded in a large twisted flux tube within a highly sheared bipolar magnetic field (Tandberg-Hanssen, 1974). Over the prominence larger scale unsheared magnetic fields are often observed in X-ray emission.

As shown by Anzer in 1993, at present no physical models for inverse polarity prominences exist. A promising approach was the twisted flux tube model of Cartledge and Hood (1993), which describes an inverse polarity prominence in a very elegant way; but a detailed matching of the flux tube to the untwisted coronal field was not demonstrated in that paper. The first successful basic model for a quiescent prominence of I-type polarity was only recently published by Low (1993).

Following this model of Low (1993) more complicated current sheets have been examined in this chapter. Our analytical current sheet models describe an inverse polarity prominence embedded in a large twisted flux tube. The actual constant-current force-free solution, containing the current sheet, representing the prominence,

is matched onto an external, unsheared, potential field, which vanishes at infinity.

By varying the current sheet intensities it is possible to model different prominence mass distributions with height and see how the model compares with observed prominence properties. This has been discussed in detail in the previous section. In all cases the background force-free field needs to be of a sufficient strength in order that the Lorentz force is in the correct direction, hence avoiding the self-pinching effect of the current sheet. Assuming λ is large enough to satisfy this restriction, it turns out that the shear angle is largely independent of λ but does agree with observations. The dip angle and the prominence mass do depend on the background field strength through λ. As λ increases the dip angle decreases and the prominence mass increases. For most cases these properties agree with observations. Finally, the magnetic field strength increases with height in the prominence for all our models.

6.7 On General Current Sheets

As seen in the last sections a prominence can be represented by a current sheet. In this particular case the current sheet, together with its image current sheet below the photosphere, was given by the potential part A_{pot} in the general solution (6.10) to equation (6.7). The magnetic field is force-free within $r \leq r_0$ and potential outside ($r > r_0$). The edge of the flux tube is a circular field line at $r = r_0$ and $A = 0$. To describe this potential part of the field $\mathbf{B} = (B_x, B_y, 0)$ complex variable theory was used ($\omega = x + iy$, $i = \sqrt{-1}$) and the prominence was represented by a branch cut in the complex plane. This section gives a short overlook on general current sheets in this particular realisation.

Generally we can write

$$\begin{aligned} B = B_y + iB_x &= f(\omega)\left(\omega + ib_1\right)^{n/2}\left(\omega + ib_2\right)^{n/2} \\ &+ g(\omega)\left(\omega + \frac{ir_0^2}{b_1}\right)^{n/2}\left(\omega + \frac{ir_0^2}{b_2}\right)^{n/2}, \end{aligned} \tag{6.34}$$

whereas the current sheet CS (extending along the y-axis from $y = -b_1$ to $y = -b_2$, $r_0 > b_2 > b_1 > 0$) is described by the first term on the right side of above equation (6.34) and the image current sheet ICS (extending along the y-axis from $y = -r_0^2/b_2$ to $y = -r_0^2/b_1$) by the second term. $f(\omega)$ and $g(\omega)$ are initially arbitrary functions of ω. For particular forms for $f(\omega)$ and $g(\omega)$ it is possible to have a circular field line at the edge of the flux tube at $r = r_0$.

We rewrite 6.34 as (n being a positive odd integer)

$$\begin{aligned} B &= f(\omega)\left[\left(\omega + ib_1\right)^{n/2} - \left(\omega + ib_2\right)^{n/2}\right]^2 \qquad (CS) \\ &+ g(\omega)\left[b_1^{n/2}\left(\omega + \frac{ir_0^2}{b_1}\right)^{n/2} - b_2^{n/2}\left(\omega + \frac{ir_0^2}{b_2}\right)^{n/2}\right]^2 \qquad (ICS) \end{aligned} \tag{6.35}$$

Setting $\omega = r_0 e^{i\vartheta}$, B can be transformed to

$$\begin{aligned} B &= i^n f(r_0 e^{i\vartheta})\left[b_1^{n/2}\left(1 - \frac{r_0 e^{i\vartheta}}{b_1}\right)^{n/2} - b_2^{n/2}\left(1 - \frac{r_0 e^{i\vartheta}}{b_2}\right)^{n/2}\right]^2 \\ &+ r_0^n e^{in\vartheta} g(r_0 e^{i\vartheta})\left[b_1^{n/2}\left(1 + \frac{r_0 e^{-i\vartheta}}{b_1}\right)^{n/2} - b_2^{n/2}\left(1 + \frac{r_0 e^{-i\vartheta}}{b_2}\right)^{n/2}\right]^2. \end{aligned} \tag{6.36}$$

We see that that the terms in the square brackets of both the current sheet and the image current sheet in equation (6.36) are complex conjugates. To make the field line circular at $r = r_0$, $Be^{i\vartheta}$ has to have a real contribution only. Therefore the relation between $f(\omega)$ and $g(\omega)$ has to be

$$g(\omega) = \frac{1}{i^n} \frac{r_0^2}{\omega^{n+2}} f^*(\omega), \tag{6.37}$$

where f^* is the complex conjugate of f.

Divergent terms are present as $r \to \infty$ as well as singularities at $r = 0$. The number of additional terms needed to remove these unwelcomed features depend on the power n and the way we choose $f(\omega)$, and related to it therefore $g(\omega)$.

The simplest way to achieve this is following form for $f(\omega)$ (with CS standing for the current sheet term, and ICS for the image current sheet term, and C_k and K_l being constants):

$$\begin{aligned} f(\omega) = \frac{C_k}{\omega^k} \quad &\Rightarrow \quad k \text{ singularity-terms for } CS \to 0 \quad (:= f_m^0) \\ &\Rightarrow \quad (k-1) \text{ non-vanishing terms for } ICS \to \infty \quad (:= g_m^\infty) \end{aligned}$$

$$\begin{aligned} g(\omega) = \frac{K_l}{\omega^l} \quad &\Rightarrow \quad (l-2) \text{ singularity-terms for } ICS \to 0 \quad (:= g_m^0) \\ &\Rightarrow \quad (l-3) \text{ non-vanishing terms for } CS \to \infty \quad (:= f_m^\infty) \end{aligned}$$

$k, l \in N_0$ and are related to each other by $k + l = n + 2$. The singularity-terms (f_m^0, g_m^0) are of the form

$$f_m^0 = \frac{C_m}{\omega^m}, \quad m = 1, 2, ..., k \qquad \text{and} \qquad g_m^0 = \frac{K_m}{\omega^m}, \quad m = 1, 2, ..., l-2.$$

For $m > 1$ every singularity-term needs another term to keep the field line circular at $r = r_0$. It is the beauty of Mathematics that these corresponding terms are exactly the divergent terms from the opposite current sheet as $r \to \infty$. So f_m^0 depends on g_m^∞ and g_m^0 on f_m^∞. Therefore the non-vanishing terms at infinity (g_m^∞, f_m^∞) are given by

$$g_m^\infty = (-1)^{m+1} \, f_m^0 \, \frac{\omega^{2m-2}}{r_0^{2m-2}} \quad m = 2, 3, ..., k$$

and

$$f_m^{\infty} = (-1)^{m+1}\, g_m^0\, \frac{\omega^{2m-2}}{r_0^{2m-2}} \quad m = 2, 3, ..., l-2.$$

These additional terms, removing singularities and divergent terms at infinity, have then to be subtracted from the original description of the current sheets (6.35) in order to make the field well-behaved for $r = 0$ and as $r \to \infty$.

In this description current sheet and image current sheet balance each other perfectly with all the additional terms needed. It is clear that fields with higher powers can be selected, but the number of terms needed to keep the edge of the flux tube circular and the field well behaved will increase accordingly.

Chapter 7

Prominence Sheets supported in Twisted Flux Tubes

7.1 Introduction

Numerical calculations of a 2-dimensional flux tube with an embedded current sheet, representing a prominence, are presented. The field inside the magnetic flux rope is considered to be force-free, as required for a functioning prominence model (see chapter 3). The field outside the magnetic flux tube, representing the coronal magnetic field, is taken to be potential. The matching of the force-free flux tube to the outside potential unsheared magnetic field has been accomplished in the way described analytically in chapter 6.

However, the numerical code proved to be difficult to adjust to the problem investigated, as discussed later. The current within the flux tube has a tendency to increase continuously, expanding the flux rope right to the margins of the numerical box. Various methods of restricting the current have been attempted.

7.2 Mathematical Description of the Model

We use a Cartesian coordinate system (x, y, z) with y being the horizontal and z the vertical component. The second horizontal component x is the direction

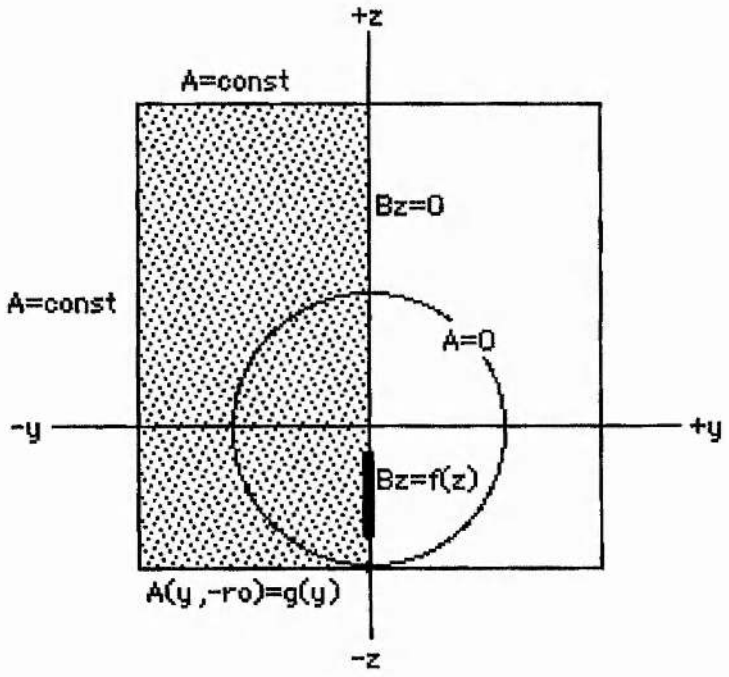

Figure 7.1: The numerical box used. Only the dotted half is solved and then mirrored along the vertical axis, where $B_z = 0$, except at the current sheet, where $B_z \neq 0$. At the sides and the top of the box the flux function A is constant, whereas at the bottom of the box, representing the photosphere, $A = g(y)$.

along the prominence. All physical quantities are assumed to be invariant in the longitudinal direction x, hence we will only consider a single plane perpendicular to the prominence axis $\{x=0, -\infty < y < \infty, 0 < z < \infty\}$. The prominence is represented by an infinitesimally thin sheet of mass and current, along the vertical axis, extending between $-b_2$ and $-b_1$, and lies within the magnetic flux tube of radius r_0. Within the tube, surrounding the prominence sheet, the magnetic field is assumed to be force-free. Outside the flux tube it is assumed to be potential. The matching of the flux tube to the external magnetic field was accomplished as described in chapter 6.

We express the magnetic field (see section 2.3) in terms of a scalar flux function $A(y,z)$ as

$$\mathbf{B} = \left[B_x(y,z), \frac{\partial A(y,z)}{\partial z}, -\frac{\partial A(y,z)}{\partial y} \right],$$

with

$$\nabla^2 A = \begin{cases} -f(A), & \text{inside the flux tube} \\ 0, & \text{outside the flux tube} \end{cases}$$

7.3 Boundary Functions of the Numerical Code

Again the numerical code using nonlinear, multigrid, finite difference method (chapter 4) has been used to obtain solutions of the Grad-Shafranov equation (2.35) together with the included current sheet.

Only half the numerical box, dotted in figure 7.1, was solved, and the solution was then mirrored along the z-axis, containing the current sheet ($B_z = f(z) = -(z+b_2)(z+b_1)$). The boundary function at the photosphere $A(y,0) = g(y)$ has been taken as (see Figure 7.2)

$$g(y) = \begin{cases} 5\,(r_0^2 - r^2)/8, & r \le r_0 \\ 5\,r_0^2\,\ln(r_0^2/r^2)/8, & r > r_0 \end{cases} \tag{7.1}$$

with $r^2 = y^2 + z^2$ and r_0 being the radius of the magnetic flux tube.

All the other boundaries are taken as field lines so that $A(y,z) =$ constant, using the corner value on the photosphere. (They have also been treated as open boundaries, with field lines threading through the sides of the box. As expected, both treatments have had the same effect on the overall structure.)

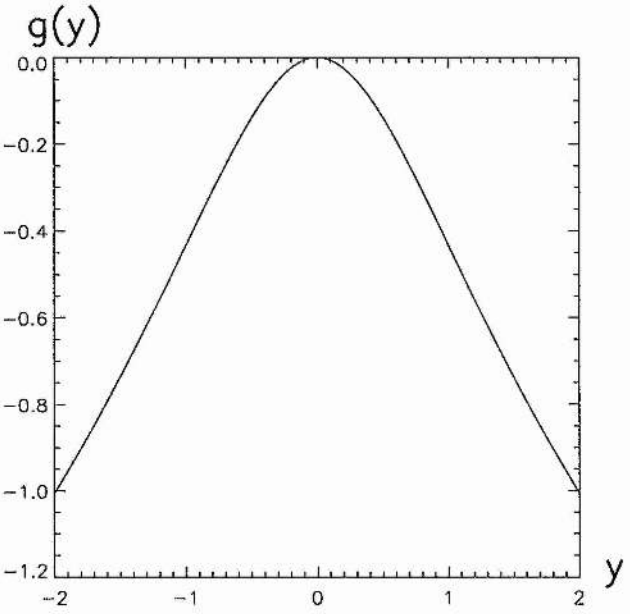

Figure 7.2: The boundary function $g(y)$ on the photosphere. $z = -r_0$.

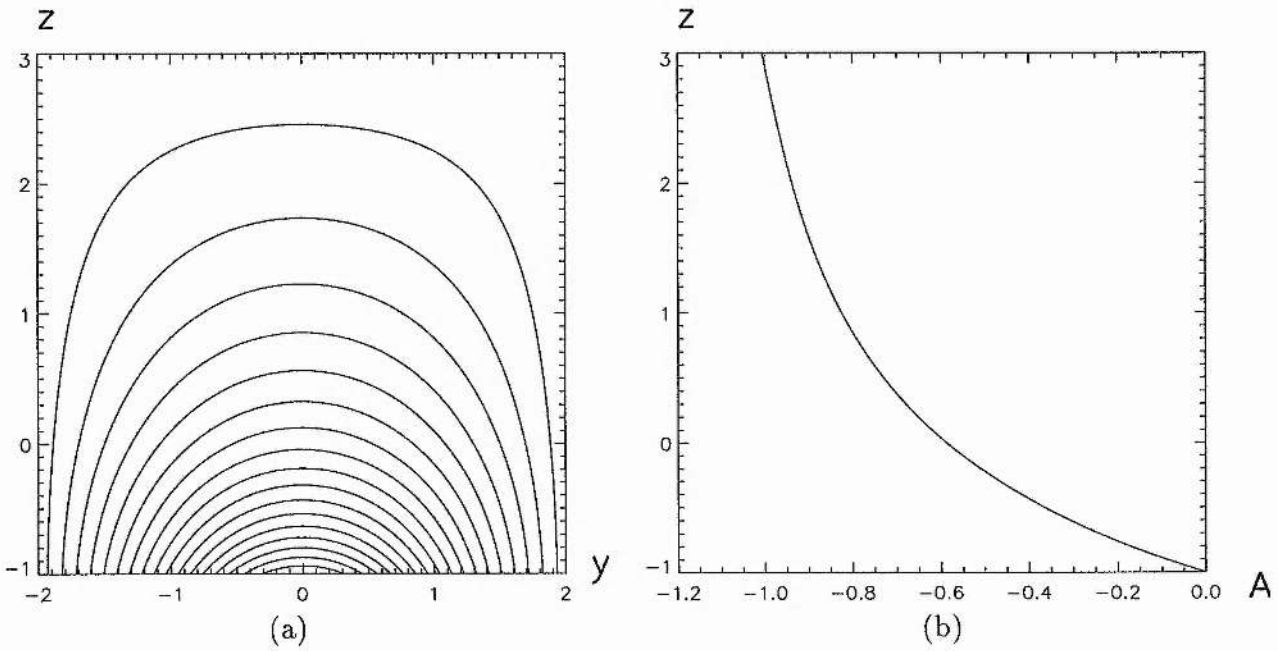

Figure 7.3: (a) Magnetic field lines for the potential solution ($f(A) = 0$). (b) The corresponding $A(0, z)$ along the vertical axis. $\lambda = 0$.

The chosen values for the numerical box are $-2 < y < +2$ on the horizontal, and $-1 < z < +3$ on the vertical. The center of the flux tube is located at (0,0) with a radius of $r_0 = 1$. The current sheet then extends from $-b_2 = 0.8$ to $-b_1 = 0.1$.

The potential solution ($\lambda = 0$) is shown in Figure 7.3, as well as its corresponding $A(0, z)$.

7.4 Background Fields and Prominence Sheets

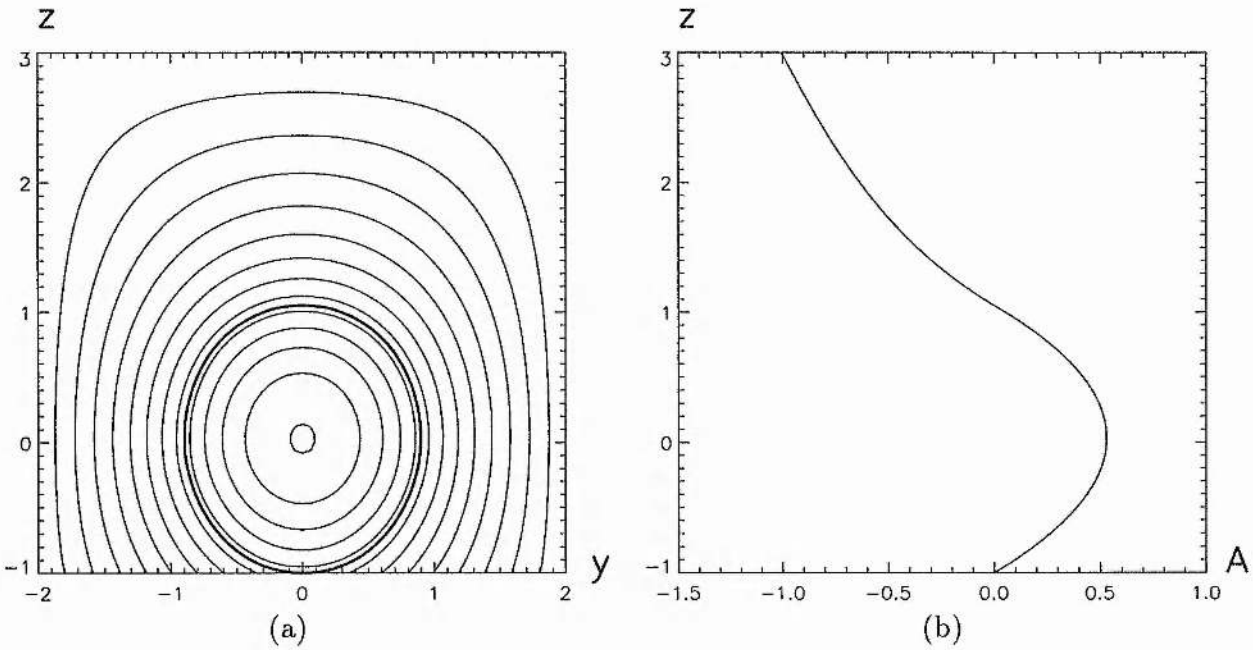

Figure 7.4: (a) Magnetic field lines for $f(A) = \lambda^2/2$ for $r \leq r_0$ and $f(A) = 0$ for $r > r_0$, and (b) the corresponding $A(0, z)$ with height. The margin of the flux tube ($A = 0$) is the dark solid line. $\lambda = 2.15$.

First we investigate the background field without the inclusion of the prominence sheet ($B_z = 0$). The resulting field for $f(A) = \lambda^2/2$ for $r \leq r_0$ and $f(A) = 0$ for $r > r_0$ as well as the behaviour of the flux function A with height is shown in Figure 7.4. A surface plot of the current is given in Figure 7.5, which clearly shows the constant current within the flux tube and the absence of it outside.

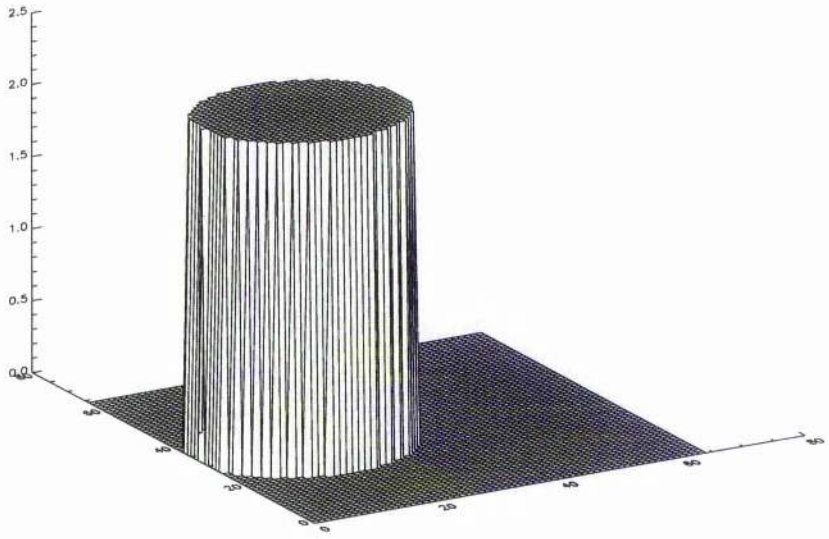

Figure 7.5: Surface plot of the current for $f(A) = \lambda^2/2$ for $r \leq r_0$ and $f(A) = 0$ for $r > r_0$, $\lambda = 2.15$

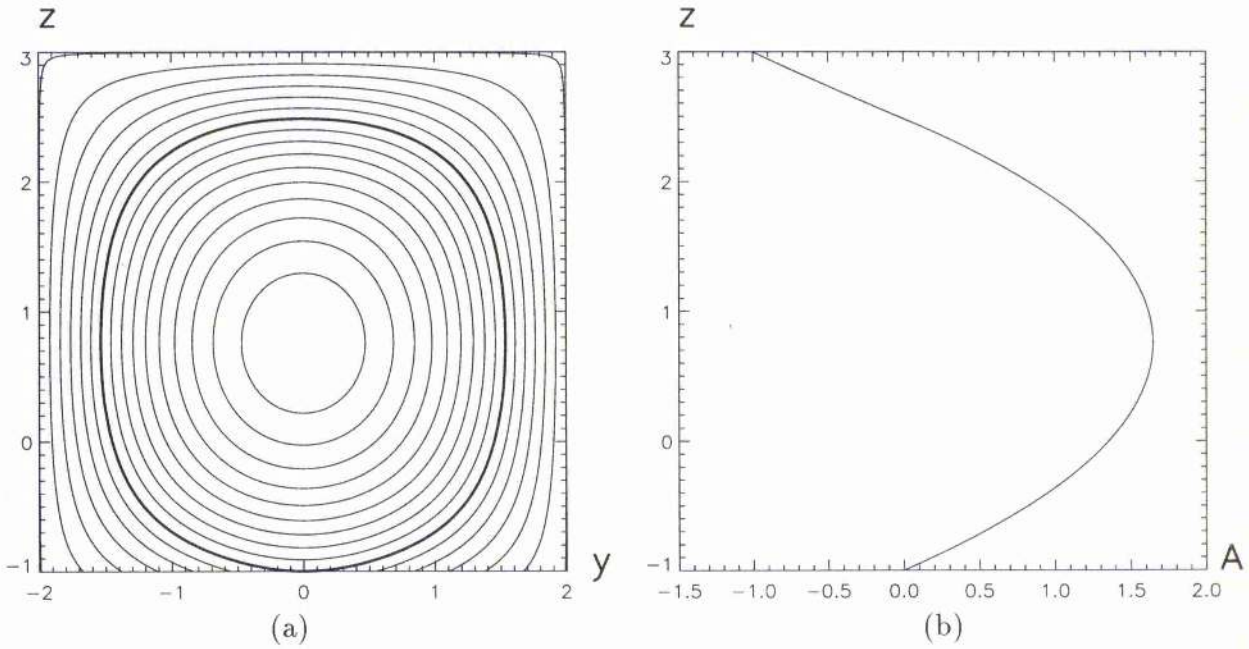

Figure 7.6: (a) Magnetic field lines for $f(A) = \lambda^2/2$ for $r \leq r_0$ and $f(A) = 0$ for $r > r_0$, and (b) the corresponding $A(0, z)$ with height. The margin of the flux tube ($A = 0$) is the dark solid line. $\lambda = 2.16$.

Unfortunately this configuration is very sensitive to the amount of current. At $\lambda = 2.14$, although some current is picked up by the code, the magnetic field configuration still shows normal arcades, similar to the potential solution shown in Figure 7.3. But a small increase of the current to $\lambda = 2.16$ is enough to blow up the flux tube (Figure 7.6), trying to fill up the whole numerical box, because the amount of current in this particular description cannot be restricted to the desired area of a flux tube with radius $r_0 = 1$. The larger the current, the more the maximum value of A moves into the center of the numerical box, forming field line loops around it.

Nonetheless, for $\lambda = 2.15$ we seem to have a proper background magnetic field. When using a rectangular box, namely twice as high as otherwise used ($-1 < z < 7$), we obtain for $\lambda = 2.156$ the same configuration ($r_0 = 1$) as in Figure 7.4. However, the whole field is again very sensitive to the current input, producing normal arcades for $\lambda = 2.155$; but for $\lambda = 2.157$ the flux tube has again nearly filled the whole box.

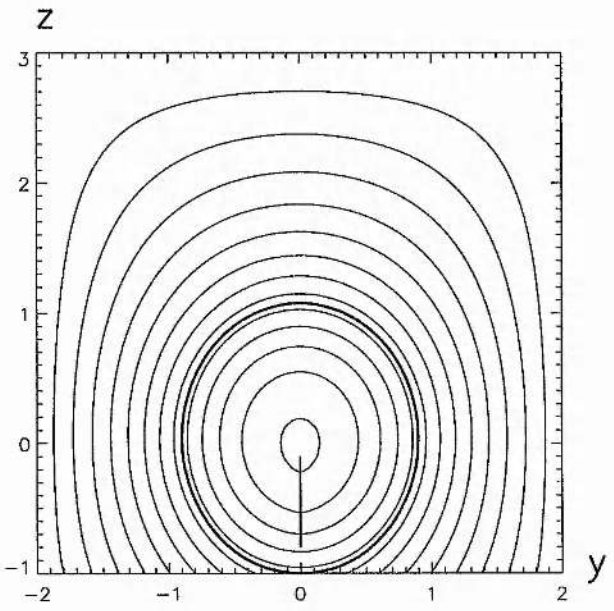

Figure 7.7: Magnetic field lines including a current sheet from $-b_2$ to $-b_1$ for $f(A) = \lambda^2/2$ for $r \leq r_0$ and $f(A) = 0$ for $r > r_0$. The margin of the flux tube ($A = 0$) is intensified. $\lambda = 2.14$.

Including the current sheet ($B_z = -(z + b_2)(z + b_1)$ between $-b_2$ and $-b_1$,

otherwise $B_z = 0$) yields for $\lambda = 2.14$ to the configuration shown in Figure 7.7. The Lorentz force is directed upwards all along the current sheet. However, the convergence of the numerical code is poor in this case, in addition to the above mentioned sensitivity of the configuration to the amount of current used. When using the rectangular box again, the code fails to converge completely and no solution can be found.

Therefore we have to assume that the obtained magnetic structure, shown in Figure 7.7, or Figure 7.4 respectively, is not a real physical solution. The problem is the current, which tends to increase in an unrestricted manner, hence blowing up the boundaries of the flux tube. We proceed to look for possibilities for restricting the current in the magnetic flux tube.

7.5 Current Restrictions

As we have seen the current within the force-free flux rope tends to expand unrestrictedly, hence the radius of the flux tube increases as far as possible, i.e. to the margins of the numerical box. Therefore we need to restrict the current within the code, so that the edge of the flux tube is kept at $r_0 = 1$. Various methods have been tried.

7.5.1 Superposition of potential solutions with the force-free solution

One possibility to prevent the constant current force-free region to blow up might be the superposition of the force-free solution with the potential solution. We rewrite our Poisson equation as

$$\nabla^2 A = \nabla^2 (A_{pot} + A_{ff}) = -\lambda^2/2. \tag{7.2}$$

Hence inside the flux tube we have a constant current,

$$\nabla^2 A_{ff} = -\lambda^2/2, \tag{7.3}$$

with one solution

$$A_{ff} = \begin{cases} \frac{\lambda^2}{8}(r_0^2 - r^2), & r \leq r_0 \\ \frac{\lambda^2}{8} r_0^2 \ln\left(\frac{r_0^2}{r^2}\right), & r > r_0 \end{cases} \tag{7.4}$$

Outside the flux tube we have

$$\nabla^2 A_{pot} = 0, \qquad r > r_0 \tag{7.5}$$

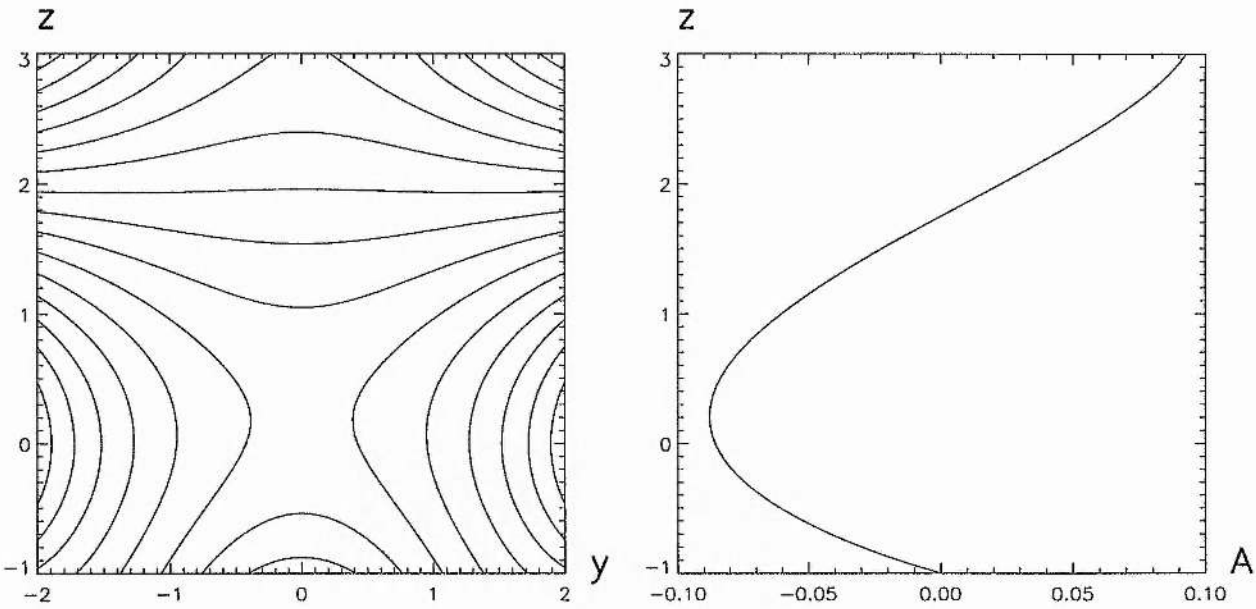

(a) (b)

Figure 7.8: (a) Magnetic field lines for the potential solution only. (b) According $A(0, z)$ with height. $\lambda = 2.0$.

We then solve numerically the potential solution (7.5). Our A_{pot} on the boundaries then has accordingly to be

$$\begin{aligned} A_{pot}^{bottom} &= g(y) - \frac{\lambda^2}{8} \ln\left(\frac{r_0^2}{y^2 + z^2}\right)\Big|_{z=-1r_0} \\ A_{pot}^{sides} &= g(y = \pm 1) - \frac{\lambda^2}{8} \ln\left(\frac{r_0^2}{y^2 + z^2}\right)\Big|_{y=\pm 2r_0} \\ A_{pot}^{top} &= g(y) - \frac{\lambda^2}{8} \ln\left(\frac{r_0^2}{y^2 + z^2}\right)\Big|_{z=3r_0} \end{aligned} \tag{7.6}$$

Figure 7.8 shows the output of the potential solution ($\lambda = 0$) together with the new boundary functions 7.6. Due to their peculiar form the boundary functions push into the box, with the same amount as the force-free solution (7.4) pushes outwards and therefore was blowing up the flux tube. Any potential solution can be added to the force-free solution (7.4); so we proceed by adding above potential solution (7.6).

$$A = A_{pot} + A_{ff} = A_{pot} + \begin{cases} \frac{\lambda^2}{8}(r_0^2 - r^2), & r \leq r_0 \\ \frac{\lambda^2}{8} r_0^2 \ln\left(\frac{r_0^2}{r^2}\right), & r > r_0 \end{cases} \tag{7.7}$$

This superposition of the force-free and the potential solution should keep the flux tube in balance, prohibiting it from unlimited increase. As we can see in Figure 7.9, it does so indeed. The current stays down, as well as the margin of flux tube at $A = 0$ stays in the lower part of the numerical box, where it is supposed to be.

So far so good. Yet, for a physical matching of the flux tube to the outside potential field we require in this particular description the field line $A = 0$, describing the edge of the flux tube, to be exactly circular. Unfortunately this is not the case.

One could also argue, since only the Laplace equation (7.5) has been solved numerically, and the force-free solution to equation (7.3) has then been added analytically, it is not a proper solution to the full equation (7.2).

So unfortunately also the solutions obtained in this way, while more realistic in appearance, cannot be taken as physically viable.

7.5.2 Special current profiles

Another way in restricting the current within the flux tube might be the use of special functions $f(A)$ instead of constant currents.

The hyperbolic tangent function

We look at the behaviour of the step-like function

$$f(A) = \frac{\lambda^2}{2}\big(1 + \tanh(10A)\big). \tag{7.8}$$

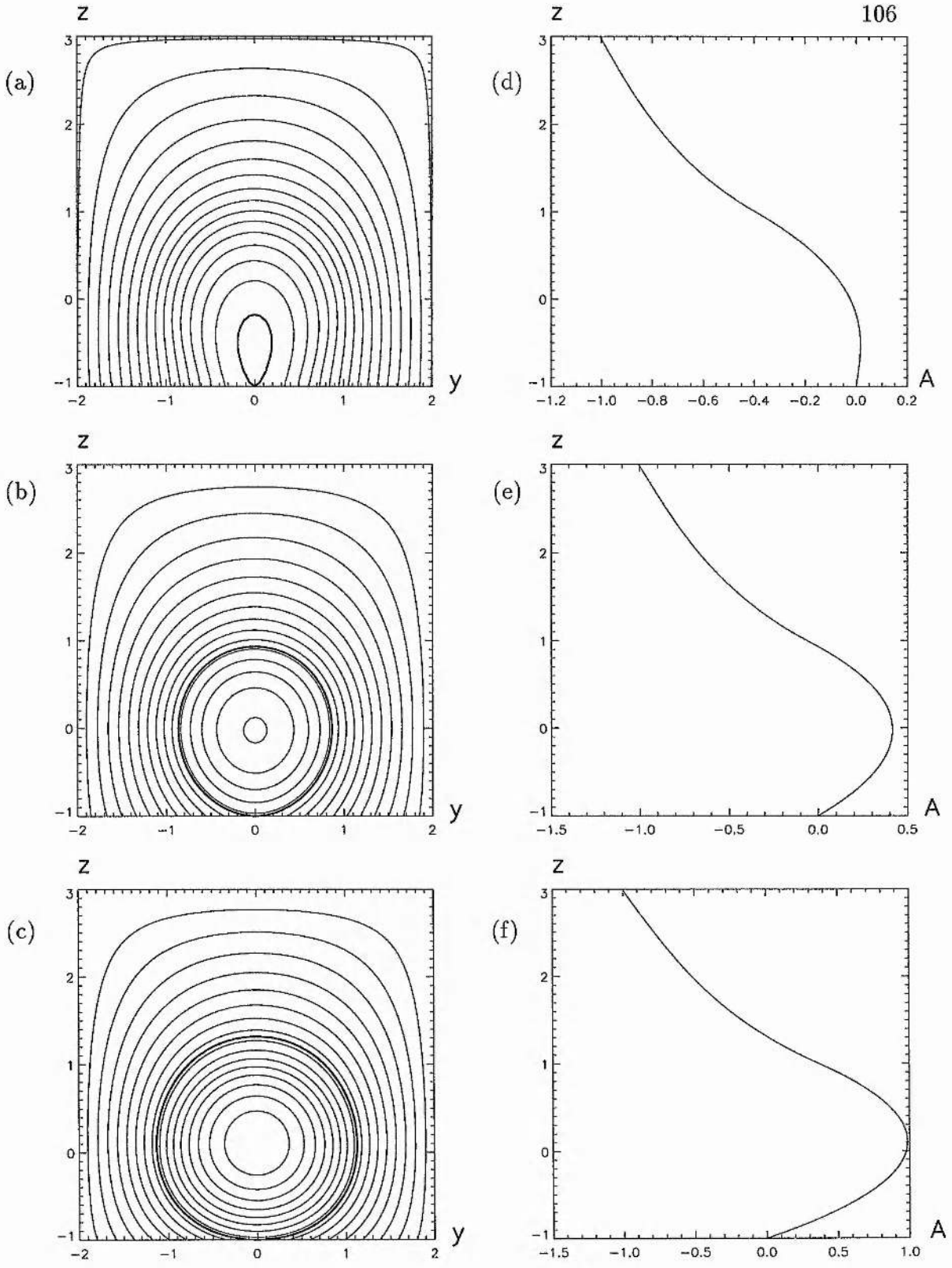

Figure 7.9: (a), (b) and (c): Magnetic field lines, superposition of potential and force-free solution. The margin of the flux tube ($A = 0$) is the dark solid line. (d), (e) and (f): Corresponding $A(0, z)$. (a) & (d): $\lambda = 1.5$; (b) & (e): $\lambda = 2.0$; (c) & (f): $\lambda = 2.5$.

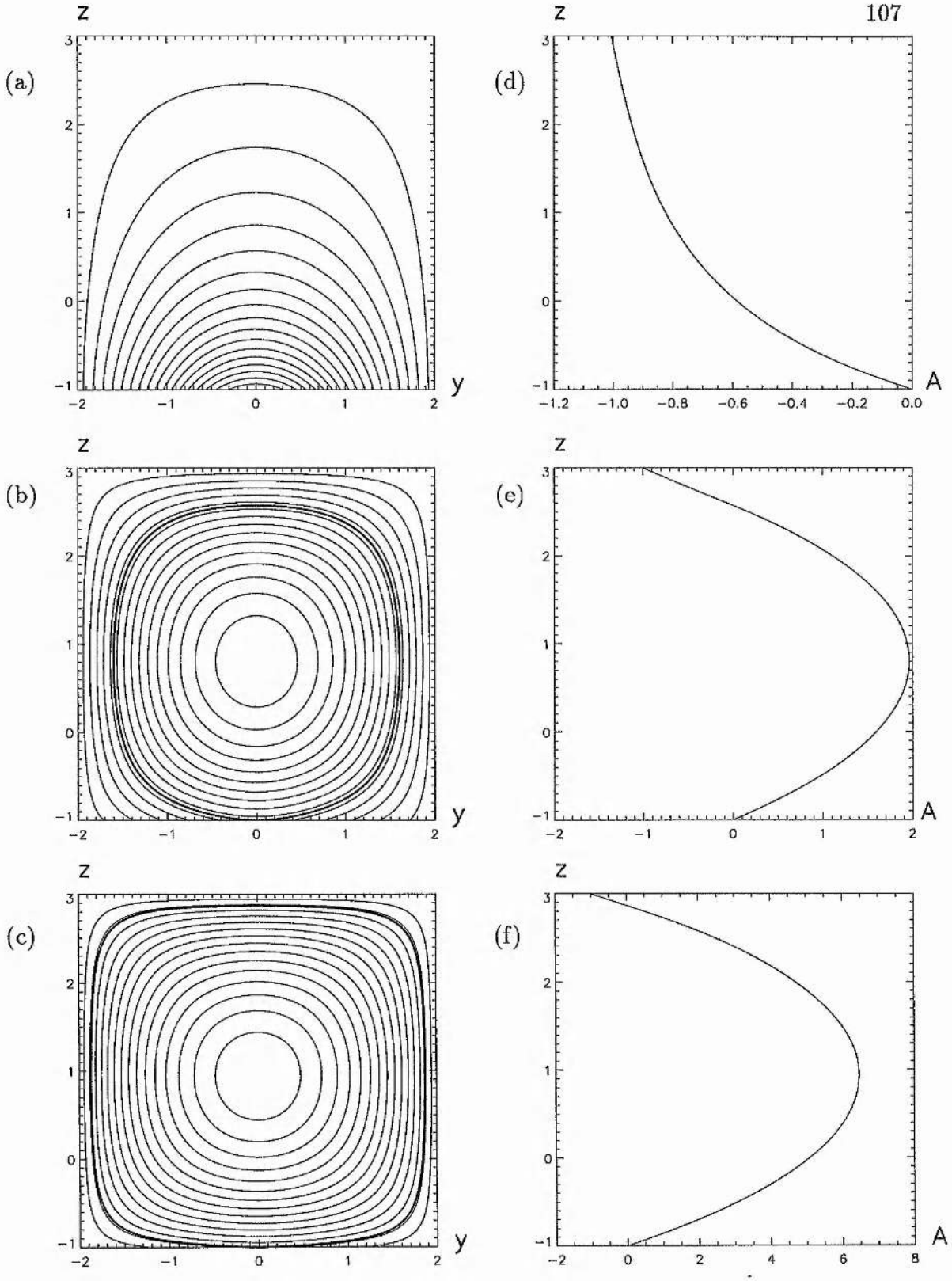

Figure 7.10: (a), (b) and (c): Magnetic field lines for $f(A) = \lambda^2(1 + \tanh(10A))/2$. The margin of the flux tube ($A = 0$) is the dark solid line. (d), (e) and (f): Corresponding $A(0, z)$. (a) & (d): $\lambda = 1.5$; (b) & (e): $\lambda = 1.6$; (c) & (f): $\lambda = 2.5$.

Figure 7.10 shows in (a) the still potential-like field for $\lambda = 1.5$. In (b) for $\lambda = 1.6$ the flux tube is already expanded over its supposed location, and in (c) for $\lambda = 2.5$ has nearly reached the margins of the numerical box. (d), (e) and (f) show the corresponding flux function A as a function of height at $y = 0$. The endpoints are fixed at zero and -1, according to the used boundary function at the photosphere. Nonetheless, the maximum value of A does again increase unlimited, hence we are left with the same problem as discussed earlier.

Therefore also a special function like (7.8) does not prevend the flux tube from blowing up and its solutions cannot be taken physically viable.

The exponential function

We use another type of function to possibly restrict the current and prevent it from increasing unlimited, namely

$$f(A) = \lambda e^{-((A-A_i)/\sigma)^2}. \tag{7.9}$$

This function keeps the total current constant, producing a Gaussian distribution. The constant A_i is responsible for the location of the peak of the function, while the constant σ defines the width of the Gaussian curve. We choose first $A_i = 0$ and $\sigma = 0.5$.

This function (7.9) does keep the maximum current value constant, as can be seen in the graphs of $A(0, z)$ in Figure 7.11. The current is restricted at last. Nevertheless, the margin of the flux tube, or the $A = 0$ field line, still moves towards the box margins with bigger λ-values, since the location of the $A = 0$ field line is not kept in place through that description.

We now choose a perhaps more sensible current value through the parameter λ, namely $\lambda = 1.75$, while also reducing the width of the function through a $\sigma = 0.25$.

Figure 7.12 shows the magnetic field lines as well as the corresponding flux function with height, whereas Figure 7.13 shows the current surface plot. So far the background field seems okay. Including the current sheet ($B_z = -(z + b_2)(z + b_1)$ between $-b_2$ and $-b_1$) yields for a $\lambda = 1.75$ to the configuration shown in Figure 7.14.

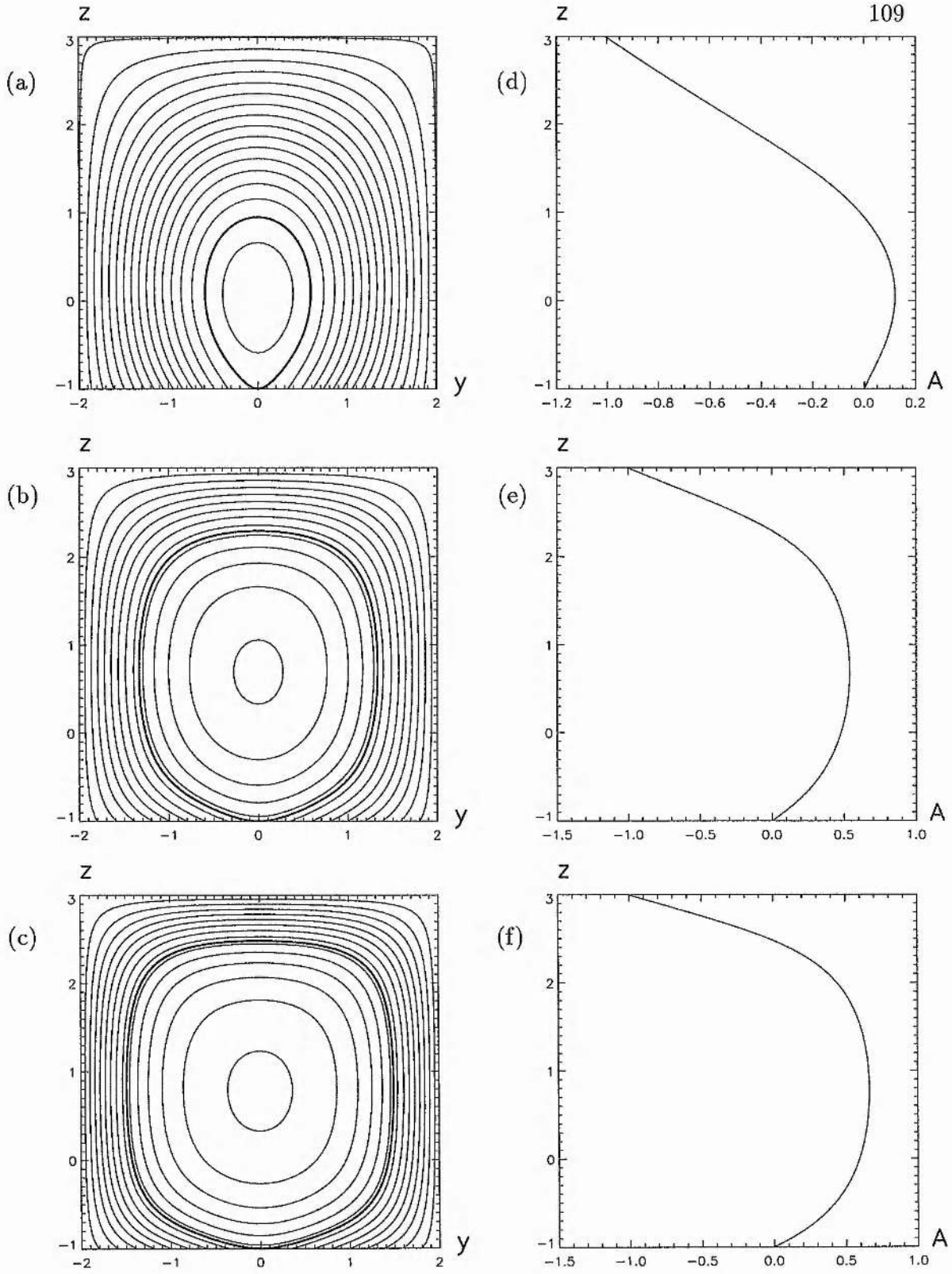

Figure 7.11: (a), (b) and (c): Magnetic field lines for $f(A) = \lambda e^{-((A-A_i)/\sigma)^2}$. The margin of the flux tube ($A = 0$) is the dark solid line. (d), (e) and (f): Corresponding $A(0, z)$. $A_i = 0.0$, $\sigma = 0.5$. (a) & (d): $\lambda = 1.0$; (b) & (e): $\lambda = 2.0$; (c) & (f): $\lambda = 3.0$.

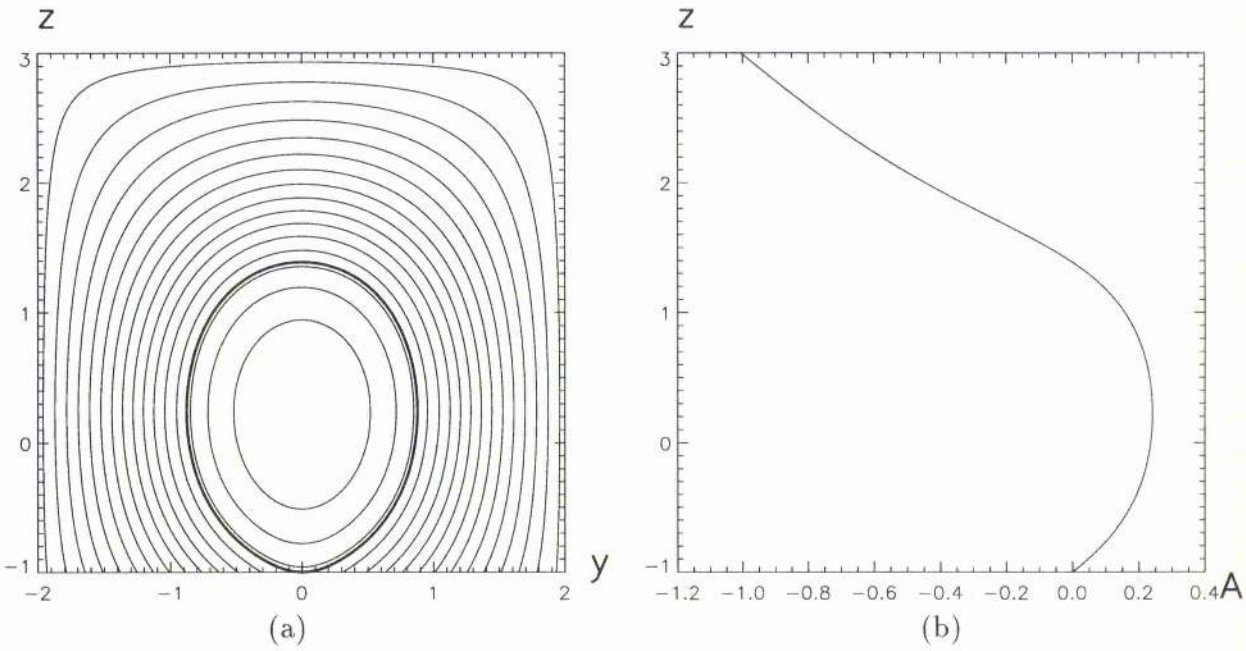

Figure 7.12: (a) Magnetic field lines for $f(A) = \lambda e^{-((A-A_i)/\sigma)^2}$ and (b) the corresponding $A(0, z)$ with height. The margin of the flux tube ($A = 0$) is the dark solid line. $\lambda = 1.75$, $A_i = 0.0$, $\sigma = 0.25$.

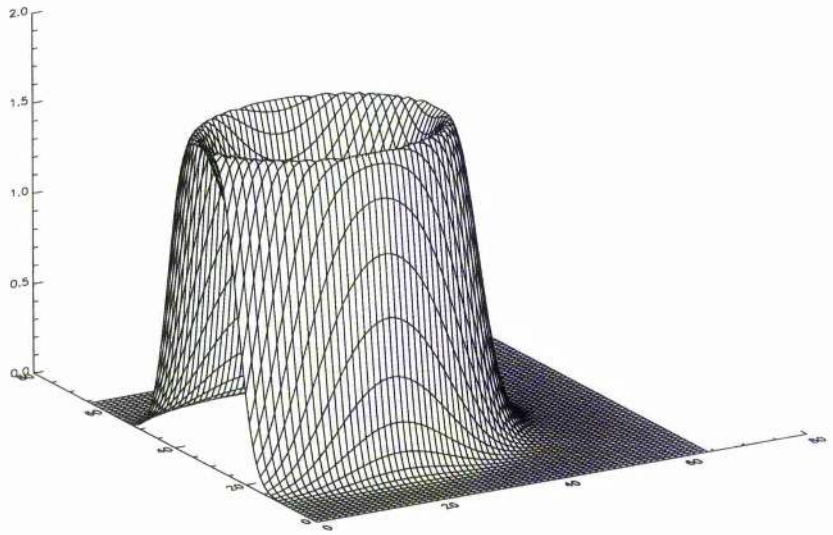

Figure 7.13: Surface plot of the current for $f(A) = \lambda e^{-((A-A_i)/\sigma)^2}$, $\lambda = 1.75$

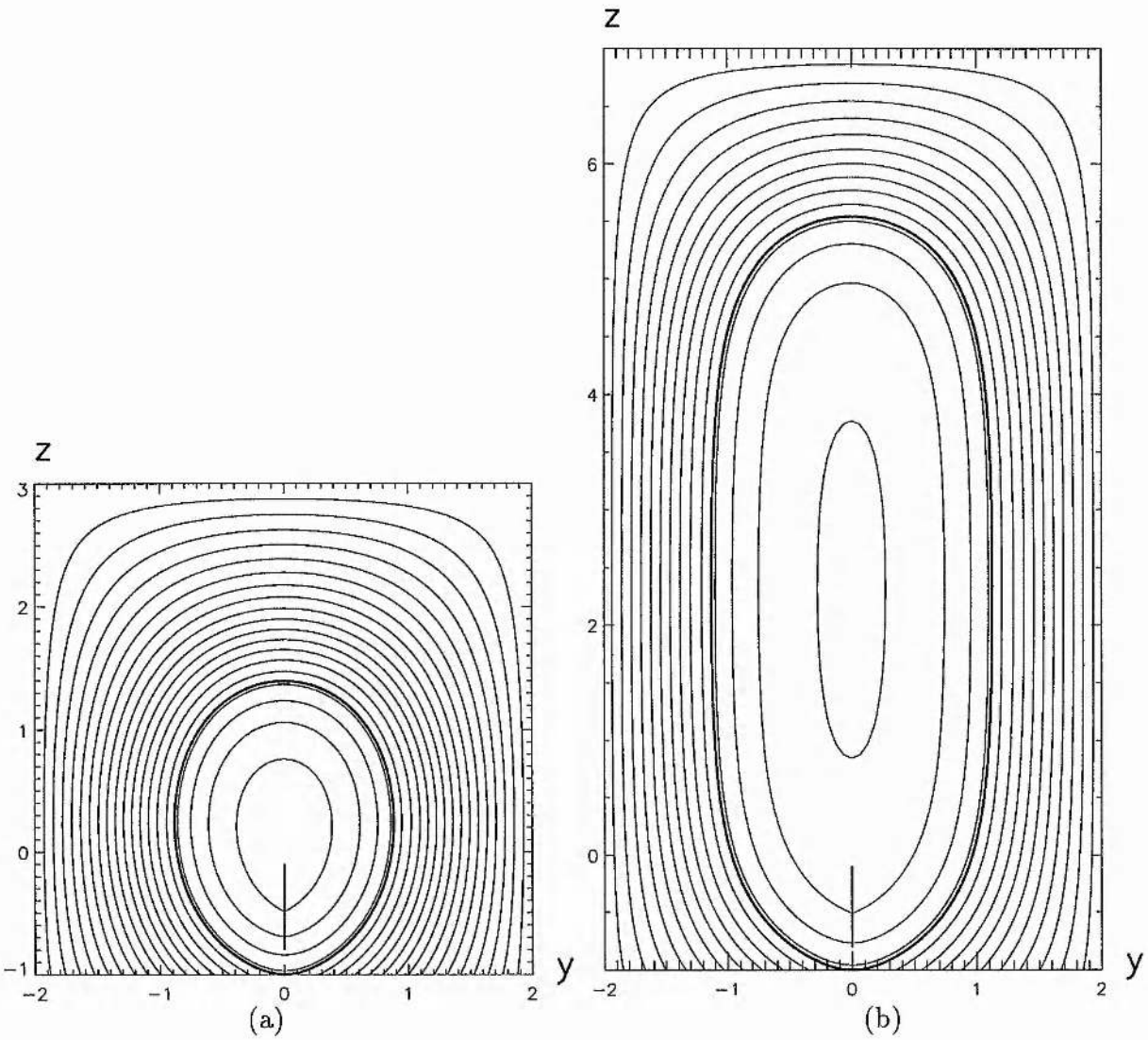

Figure 7.14: Magnetic field lines including a current sheet from $-b_2 = 0.8$ to $-b_1 = 0.1$ for $f(A) = \lambda e^{-((A-A_i)/\sigma)^2}$. The margin of the flux tube ($A = 0$) is the dark solid line. (a) Square box. (b) Rectangular box (twice the height than width). $\lambda = 1.75$, $A_i = 0.0$, $\sigma = 0.25$.

However, again the convergence of the numerical code is poor. When using the rectangular box, the convergence stays poor, but in addition the O-type neutral point moves towards the center of the box instead of remaining in the lower part, as can be seen in Figure 7.14 b. This is due to the already mentioned sensitivity of the configuration to the amount of current used. Also these solutions are therefore again not really physical.

7.6 Force-Free Fields only

Since the computer program has difficulties in dealing with the required change from a force-free field to a potential field within one solution, we look shortly at a force-free configuration only. We use a configuration derived in chapter 5, namely the magnetic field structure shown in Figure 5.9b. We then include a current sheet, $B_z = -(z - b_2)(z - b_1) \cdot C$, between $b_1 = 0.3$ and $b_2 = 0.8$. The result is shown in Figure 7.15a for $C = 2.1$, which has a Lorentz force upwards all along the sheet, as required for a meaningful solution. Figure 7.16 shows the corresponding surface plot of the current. As we can see, the current distributed on the current sheet is quite small though.

Figure 7.15b shows the magnetic structure using a stronger current sheet, namely $C = 10.0$. Figure 7.17 again gives the corresponding current surface plot. The current in the sheet is much more significant now. However, we can see that the Lorentz force is downwards on the top part of the sheet. The background force-free field is not strong enough anymore to avoid the self-pinching effect of the current sheet.

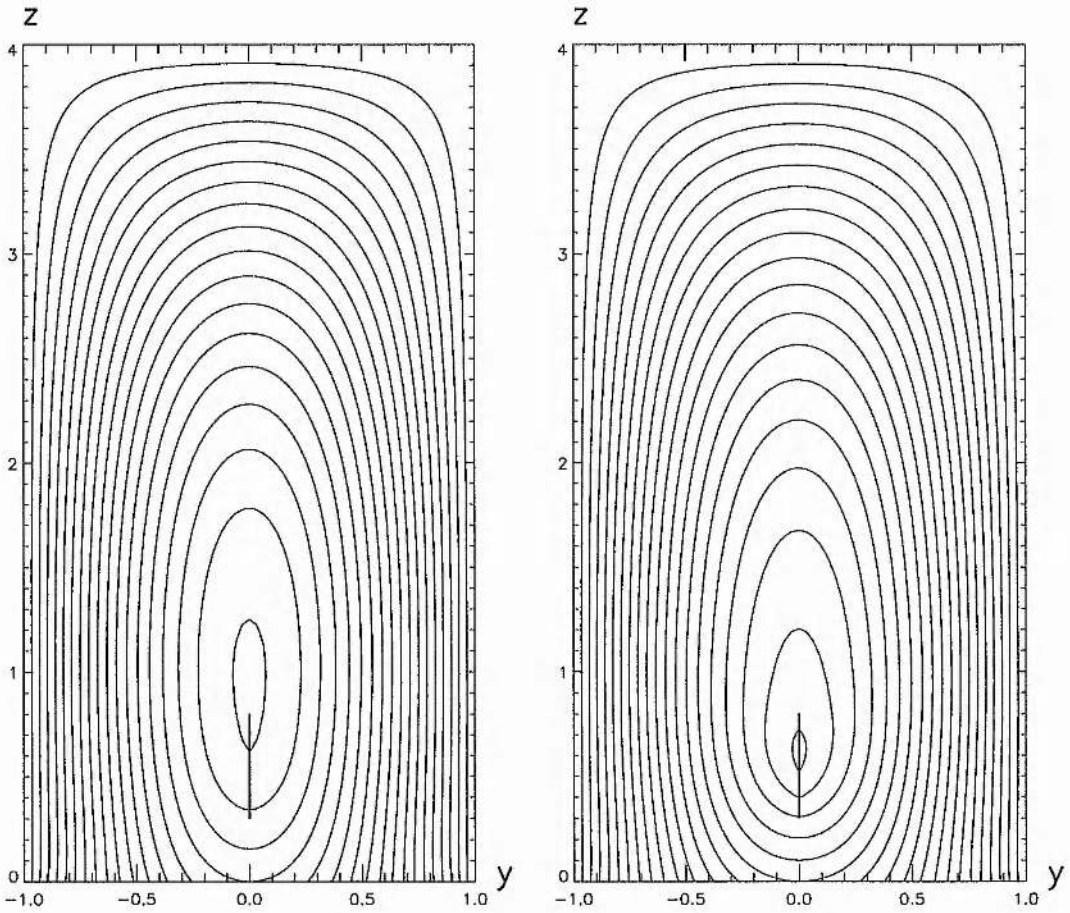

Figure 7.15: Magnetic field lines for $\lambda f(A) = \lambda A(1 - c_2 A^2)$, $c_2 = 0.1$, boundary function $\tilde{g}$, $\lambda = 3$, with the inclusion of a current sheet between $b_1 = 0.3$ and $b_2 = 0.8$. (a) $C = 2.1$, (b) $C = 10.0$.

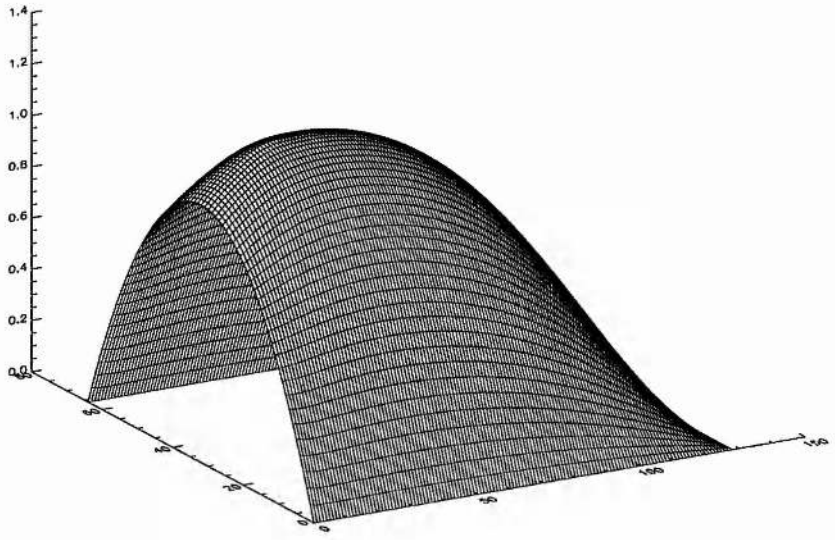

Figure 7.16: Surface plot of the current for $\lambda f(A) = \lambda A(1 - c_2 A^2)$, $c_2 = 0.1$, boundary function $\tilde{g}$, $\lambda = 3$, with the inclusion of a current sheet between $b_1 = 0.3$ and $b_2 = 0.8$. $C = 2.1$

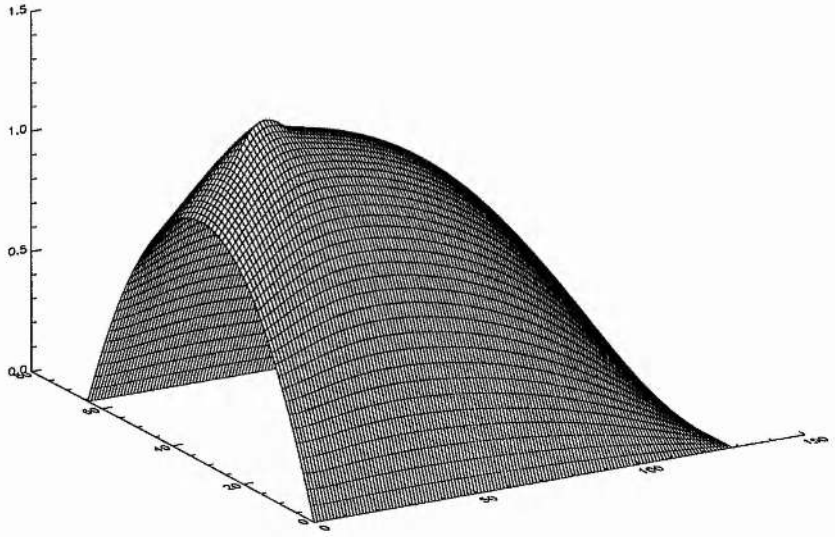

Figure 7.17: Surface plot of the current for $\lambda f(A) = \lambda A(1 - c_2 A^2)$, $c_2 = 0.1$, boundary function $\tilde{g}$, $\lambda = 3$, with the inclusion of a current sheet between $b_1 = 0.3$ and $b_2 = 0.8$. $C = 10.0$

7.7 Discussion

So far all the solutions obtained when matching a force-free field onto a potential field do not seem to be physically valid. The numerical code was not able to deal with both the potential and the force-free field together within one numerical box. It cannot restrict the amount of current, which tends to grow unlimited and blows up the flux tube, pushing the potential field aside. Analytically - although in complex variable theory and therefore with special current sheets (chapter 6) - it has been proven that prominence sheets in equilibrium can exist in such given surroundings. But due to the computing difficulties encountered these numerical results in this chapter have to be viewed very critically.

The main problem is that as the field within the force-free region expands, more current in this region can flow. This on the other hand produces an even stronger expansion, hence even more current is flowing in then - leading to a vicious circle.

The advantage of force-free fields only is that the current is evenly distributed throughout the box, hence the program can easily find physical solutions. The force-free solutions we looked at in section 7.6 used some of the solutions obtained in chapter 5, and now the code converged without any difficulty. We obtain physical results, as long as the background field is strong enough to prevend the self-pinching effect of the current sheet.

Chapter 8

Summary and Future Prospects

Cool, dense, long-lived sheets of plasma, known as quiescent prominences, have been observed since the Middle Ages. With the evolution of photographic and spectrographic techniques, as well as through satellites and space crafts, better and better observations are possible to obtain, helping the theoretician to explain and model these interesting structures on the sun. Most of the quiescent prominences have been found to be of inverse polarity. Yet modelling such features has been proven to be difficult.

With that in mind in chapter 5 we investigated first the overall magnetic structure alone, without a prominence sheet, to see how it is influenced by different current distributions and if they can create inverse polarity structures, that being a necessary precondition for forming prominences of I-type polarity. A variety of different current profiles have been considered in the Grad-Shafranov equation (2.35) that describes the magnetohydrostatic equilibrium. Some current functions had to be adjusted by appropriate constants to yield to the desired results. However, for all current distributions the range of the current required to form an X-type neutral point above the photosphere has turned out to be very small, whereas for O-type neutral points only the current range is much wider. Hence, the results of the numerical solutions to the equilibrium equation suggest that most of the fully developed, long-lived prominences are likely to possess an O-type, but not an X-type neutral point.

Observations of erupting prominences often reveal a helical structure, sug-

gesting that prominences are embedded in a large twisted flux tube within a highly sheared bipolar magnetic field. Yet surrounding these flux ropes large-scale unsheared magnetic fields are often observed. Only very recently has a basic model, containing both a twisted flux tube as well as an overlying unsheared potential field as a description of the magnetic surroundings of a prominence, been put forward by Low (1993), since a detailed matching of the flux tube to the potential coronal field had not been accomplished as yet. Following this thread in chapter 6 we investigated analytically, using complex variable theory, more complicated and physically valid current sheets, which can represent a prominence. The constant-current force-free solutions of the twisted flux tube, containing a prominence current sheet, have been matched onto the external, unsheared, potential magnetic field. These models have then been compared with observed prominence values and were found to be in agreement with the observations. In particular, they all show an increase of the magnetic field strength with height, an observation which proved difficult to explain. Hence, in chapter 6 we present a successful analytical model for prominences of inverse polarity.

A disadvantage of complex variable theory is that the current sheets used are of special form and cannot be altered without quite drastically influencing the whole configuration. Hence in chapter 7 we leave the field of complex functions and investigate simpler current sheets; a task which cannot be accomplished analytically anymore. Therefore we again use the numerical code, based on a multigrid, finite, difference method, but now keeping the realistic configuration of a force-free twisted flux tube, containing the prominence current sheet, together with a surrounding untwisted potential field. However, the code showed to have problems with switching from the force-free solution to the potential one within one numerical box. The force-free solution proved to have a tendency to take over and push the potential part aside. Various methods of restricting the current and keeping the flux tube in the given position have been tried, but were not entirely satisfactory. The solutions obtained have to be viewed critically, and so far cannot be taken as actually physically viable. Nevertheless, they do suggest (as well as the analytic results in previous chapter 6) the existence of such models, once these problems of more "technical" nature have been overcome.

An interesting step for future work would be incorporating a finite, vertical prominence sheet with a non-zero thickness in the model of the global magnetic field, allowing one to determine the distribution of the prominence density, pressure and temperature. One obvious deficiency in all current sheet models is the inert assumption that the prominence is represented well by an infinitesimally thin sheet of mass and current. The temperature within such a sheet is zero. In reality, however, prominences do have an appreciable thickness.

Since such a internal solution, matched onto the external force-free solution of a twisted flux tube, already exists (Cartledge and Hood, 1993), but cannot be matched onto an outside unsheared potential field with our method used in chapter 6 or 7 because of the non-circular edge of their flux tube, another possible future extension would be to find detailed ways of matching flux tubes with non-circular field lines onto the global, potential field.

As computer efficiency improves and increasingly more robust MHD codes are developed, a logical and promising future extension to the model in chapter 7 would be to find a truly successful way to restrict the current within the flux tube.

Nevertheless, it should be remembered that the analytical solutions to the MHD equations play an important role, even if only solvable in highly idealised conditions. They demonstrate the basic physical principle behind a model and one is free of fear of numerical errors or unwanted effects due to the imposed boundary conditions.

Prominences come in many forms and shapes, and the fact, that there are two basic different types for their global magnetic field, suggests that it is quite likely that various processes play a part in prominence evolution. Until observations indicate otherwise, it is the task of the theoretician to investigate as many different possibilities; only then can we in time increasingly improve our knowledge and understanding of these most fascinating objects on our sun, or stars in general.

Bibliography

Amari, T. and Aly, J. J. (1990). *Astron. Astrophys.* **231**: 213.

Amari, T. and Aly, J. J. (1992). *Astron. Astrophys.* **265**: 791.

Amari, T., Démoulin, P., Browning, P., Hood, A. W. and Priest, E. R. (1991). *Astron. Astrophys.* **241**: 604.

Antiochos, S. K., Dahlburg, R. B. and Klimchuk, J. A. (1994). *Astrophys. J. Lett.*

Anzer, U. (1989). *in* E. R. Priest (ed.), *Dynamics and Structure of Quiesent Solar Prominences*, Kluwer, Dordrecht, p. 143.

Anzer, U. (1990). *Solar Phys.* **130**: 403.

Anzer, U. (1993). *Comments Astrophys.* **16**(5): 305.

Athay, R. G., Querfeld, C. W., Smartt, R. N., Landi Degl'innocenti, E. and Bommier, V. (1983). *Solar Phys.* **89**: 3.

Babcock, H. W. and Babcock, H. D. (1955). *Astrophys. J.* **121**: 349.

Birn, J. and Schindler, K. (1981). Chapter 6, *in* E. R. Priest (ed.), *Solar Flare Magnetohydrodynamics*, Gordon and Breach Science, New York, London, Paris, p. 343.

Brandt, A. (1977). *Math. Comput.* **31**: 333.

Briggs, W. L. (1987). *A Multigrid Tutorial*, SIAM, Philadelphia.

Cartledge, N. and Hood, A. W. (1993). *Solar Phys.* **148**: 253.

Démoulin, P. and Forbes, T. G. (1992). *Astrophys. J.* **387**: 394.

Démoulin, P., Raadu, M. A. and Malherbe, J. M. (1992). *Astron. Astrophys.* **257**: 278.

Engvold, O. (1976). *Solar Phys.* **49**: 283.

Fiedler, R. A. S. (1992). *Proceedings of the first SOHO Workshop* **ESA SP-348**: 273.

Grad, H. and Rubin, H. (1958). *Proceedings of the Second United Nations International Conference in the Peaceful Uses of Atomic Energy*, United Nations, Geneva, pp. 190–7, vol. 31.

Jockers, K. (1978). *Solar Phys.* **56**: 37.

Kim, I. (1990). *in* E. Tandberg-Hanssen (ed.), *IAU Colloq. 117 on Dynamics of Solar Prominences*, Springer Verlag, Hvar.

Kippenhahn, R. and Schlüter, A. (1957). *Zs. Astrophys.* **43**: 36.

Kuperus, M. and Raadu, M. A. (1974). *Astron. Astrophys.* **31**: 189.

Kuperus, M. and Van Tend, W. (1981). *Solar Phys.* **71**: 125.

Lepeltier, T. and Aly, J. J. (1995). *Astron. Astrophys. (submitted).*

Leroy, J. L. (1977). *Astron. Astrophys.* **60**: 79.

Leroy, J. L. (1978). *Astron. Astrophys.* **64**: 247.

Leroy, J. L. (1985). *in* M. J. Hagyard (ed.), *NASA Conference Publication 2374*, p. 121.

Leroy, J. L. (1987). *in* J. L. Ballester and E. R. Priest (eds), *Proceedings of the Workshop on Dynamics and Structure of Solar Prominences*, Palma de Mallorca, p. 33.

Leroy, J. L. (1989). *in* E. R. Priest (ed.), *Dynamics and Structure of Quiesent Solar Prominences*, Kluwer, Dordrecht, p. 77.

Leroy, J. L., Bommier, V. and Sahal-Brehot, S. (1983). *Solar Phys.* **83**: 135.

Low, B. C. (1977). *Astrophys. J.* **212**: 234.

Low, B. C. (1993). *Astrophys. J.* **409**: 798.

Low, B. C. and Hundhausen, J. R. (1995). *Astrophys. J.* **443**: 818.

Lüst, R. and Schlüter, A. (1957). *Z. Naturforschung* **12a**: 850.

Malherbe, J. M. and Priest, E. R. (1983). *Astron. Astrophys.* **123**: 80.

Martin, S. F. (1973). *Solar Phys.* **31**: 3.

Martres, M., Mein, P., Schmieder, B. and Soru-Escaut, I. (1981). *Solar Phys.* **69**: 301.

Mein, P. (1977). *Solar Phys.* **54**: 45.

Nikolsky, G. M., Kim, I. S., Koutchmy, S. and Stellmacher, G. (1984). *Astron. Astrophys.* **140**: 112.

Priest, E. R. (1982). *Solar Magnetohydrodynamics*, Kluwer, Dordrecht.

Priest, E. R. (1989). *in* E. R. Priest (ed.), *Dynamics and Structure of Quiesent Solar Prominences*, Kluwer, Dordrecht, p. 1.

Priest, E. R., Hood, A. W. and Anzer, U. (1989). *Astrophys. J.* **344**: 1010.

Ridgway, C., Amari, T. and Priest, E. R. (1991). *Astrophys. J.* **378**: 773.

Ridgway, C., Priest, E. R. and Amari, T. (1991). *Astrophys. J.* **367**: 321.

Rust, D. M. (1967). *Astrophys. J.* **150**: 313.

Shafranov, V. D. (1958). *Sov. Phys. JETP* **6**: 545.

Stüben, K. and Trottenberg, U. (1982). *in* W. Hackbusch and U. Trottenberg (eds), *Multigrid Methods, Proceedings, Köln-Porz, 1981, Lecture Notes in Mathematics, Vol. 960*, Springer-Verlag, Berlin, p. 1.

Tandberg-Hanssen, E. (1974). *Solar Prominences*, Reidel, Dordrecht.

Tandberg-Hanssen, E. and Anzer, U. (1970). *Solar Phys.* **15**: 158.

The Poetic Edda (1994). Translated with an Introduction and Explanatory Notes by Lee M. Hollander. University of Texas Press, Austin, Texas.

Van Ballegooijen, A. and Martens, P. (1989). *Astrophys. J.* **343**: 971.

Van Tend, W. and Kuperus, M. (1978). *Solar Phys.* **59**: 115.

Wesseling, P. (1992). *An Introduction into Multigrid Methods*, John Wiley & Sons, Chichester.